International Scientific-Technical and Production Journal

The Paton WELDING JOURNAL

June 2008 # 6

English translation of the monthly «Avtomaticheskaya Svarka» (Automatic Welding) journal published in Russian since 1948

Founders: *E.O. Paton Electric Welding Institute of the NAS of Ukraine*
International Association «Welding»

Publisher: *International Association «Welding»*

Address:
E.O. Paton Electric Welding Institute,
International Association «Welding»,
11, Bozhenko str., 03680, Kyiv, Ukraine
Tel.: (38044) 287 67 57
Fax: (38044) 528 04 86
E-mail: journal@paton.kiev.ua
http://www.nas.gov.ua/pwj

State Registration Certificate
KV 4790 of 09.01.2001

Subscriptions:
$324, 12 issues per year,
postage and packaging included.
Back issues available.

CONTENTS

INLFUENCE OF NONMETALLIC INCLUSIONS IN LOW-ALLOYED STEELS ON THEIR WELDABILITY IN FLASH-BUTT WELDING

S.I. KUCHUK-YATSENKO, V.F. ZAGADARCHUK, V.I. SHVETS and G.N. GORDAN
E.O. Paton Electric Welding Institute, NASU, Kiev, Ukraine

Influence of nonmetallic inclusions (NMI) contained in low-alloyed steels on joint formation in flash-butt welding was studied. NMI including chemical elements not specified by standards in this steel class were considered. It is shown that presence of such NMI in steel impairs its weldability, particularly, if they contain elements forming refractory oxides. Methods of improvement of flash-butt welding technologies in welding steels with an increased NMI content are outlined.

Keywords: *flash-butt welding, welding mode, low-alloyed steel, alloying element, nonmetallic inclusion, oxide, weldability, joint, microstructure, fracture, fractography*

Flash-butt welding is widely used for joining rolled stock from low-carbon and low-alloyed steels (shaped sections, pipes, sheets) in the shop and site conditions. Modes of welding such items are specified in different departmental instructions and codes. The modes are usually selected taking into account the content of the main alloying elements in steel, as well as certain impurities, the content of which is controlled, in particular, sulphur and phosphorus. Joints made by flash-butt welding are characterized by stable and high mechanical property values close to the respective values of the base metal. However, from many years of experience of flash-butt welding application some cases are known, when it was impossible to achieve stable values of mechanical properties in welding of some batches of rolled stock, despite the absence of any deviations from the welding modes or steel composition from the specified values. This is most often due to the presence of non-metallic inclusions (NMI) in the welds.

In modern metallurgical production various methods of liquid metal treatment are applied, using slags, ferroadditives containing various modifiers and deoxidizers. Their interaction with the liquid metal results in NMI remaining in it, which contain various elements not included into the alloying element composition. Their content in the metal is not specified [1].

The purpose of this work was investigation of NMI influence in low-alloyed steels on formation of joints, produced by flash-butt welding, and their mechanical properties.

Investigations were conducted on seamless pipes of oil and gas pipeline sizes of steel 20, made in various enterprises of Ukraine and Russia and differing by their manufacturing technology. Two batches of pipes of 168 mm diameter with 6.5 mm wall thickness (batch #1) and of 178 mm diameter with 10 mm wall thickness (batch #2) were selected for welding. Pipe welding was performed in flash-butt welding machine K584 designed by PWI, which is batch-produced by Kakhovka Plant of Electric Welding Equipment [2]. Such machines are used in different industries, in particular in the enterprises of oil and gas industry for welding pipes of 114–325 mm diameter.

At the first stage of investigations welding of pipes of both the batches was conducted in the mode specified by the departamental codes [3]. The main parameters of the mode are given in Table 1 (mode A). Testing of pipe welded joints was conducted in keeping with the above code and API 1104 International Standard.

NMI identification and distribution in samples of base metal and welded joints was conducted on polished microsections, and the content of chemical elements in NMI was determined in the Cameca microanalyzer Camebax SX-50. Etching in nital was used to identify the structural components of the base metal and welded joints in the studied samples, and the microstructure was studied in Neophot-32 microscope at different magnifications. Fractographic studies of the fracture surface were performed in JSM-840 scanning microscope with Link-Systems microanalyzer.

Content of the specified alloying elements in both the batches is approximately the same (Table 2), but they differ as to the composition of uncontrollable inclusions (Table 3). Steel of batch #1 contains fine

Table 1. Parameters of pipe welding modes

Pipe batch #	Welding mode	Welding time, s	Final flashing speed, mm/s	Flashing allowance, mm	Maximum consumed power, kV·A	Specific upsetting pressure, kg/mm^2	Upset value, mm	Minimum upset speed, mm/s
1, 2	A (specified by VSN 006–89)	75–80	1.0–1.2	16.5–19.2	76	4.0–5.6	6	25
2	B (improved)	45–50	4.0–4.5	15.0–16.0	304	5.0	7	100

Table 2. Composition of steel pipes, wt.%

Pipe batch #	C	Si	Mn	S	P	Cr	Ni	Cu	Al*	V*	Mo*	Ti*	Nb*	As
1	0.212	0.218	0.60	0.017	0.014	0.03	0.03	<0.02	0.021	<0.02	<0.03	<0.002	0.002	–
2	0.163	0.327	0.52	0.003	0.007	0.11	0.13	0.19	0.010	0.05	0.03	0.002	<0.002	0.01

*Elements not specified by GOST.

Table 3. Elementary composition of NMI in pipe steels, wt.%

Pipe batch #	Al	Si	Mg	S	Mn
1	0.382	0.421	0.467	0.132	0.659
	0.278–0.298	0.321–0.464	0.366–0.775	5.584–13.496	10.358–19.304
2	8.680–31.183	1.216–23.117	1.969–8.194	0.105–0.421	0.389–1.000
	0.331–0.653	6.672–30.933	0.328–0.731	0.012–0.050	0.484–0.226

Table 3 (cont.)

Pipe batch #	O	V	Ca	Note
1	1.157	N/D	N/D	Fine iron oxides
	1.267–13.425	Same	Same	Iron and manganese oxysulphides
2	15.263–37.527	0.018–0.059	0.277–6.819	Al–Si–Mg–Ca system oxides
	10.206–17.722	0.074–0.062	0.074–0.261	Iron silicates

globular inclusions of iron oxides and larger size inclusions of manganese and iron oxysulphides (Figure 1, *a*). Also found are uniformly distributed in the structure inclusions of aluminium oxides, fringed by the sulphide phase. In steel of batch #2 pipes no oxysulphides are found. The metal contains numerous particles of complex oxides of about 1 μm size, the composition of which includes aluminium, silicon, magnesium, and calcium (Figure 1, *b*). Alongside uniform distribution through the volume, the particles create clusters in the form of bands. In addition to these particles, the steel also contains inclusions of iron silicates with a somewhat higher content of elements included into the particle composition.

Microstructure of steels of pipes from both batches is pearlitic-ferritic (Figure 2). It, however, differs considerably in terms of morphology. Ferrite grains in steel of batch #1 pipes have a coarse polygonal shape (Figure 2, *a, b*) with pearlite colonies located between them. Microstructure of steel of batch #2 pipes differs by smaller grain size and consists of ferrite and tempered products of eutectoid decomposition (Figure 2, *c, d*).

Width of ferrite band [4] of the weld of batch #2 pipes is 1.5 times greater than in the joints of batch #1 pipes (Figure 3, *a, b*). The extent of the other structural regions of the HAZ metal and their grain size are identical, which is due to the same heat input in welding. Figure 4, *a* shows a macrosection of the joint of batch #1 pipes, and Figure 4, *b* – of batch #2 welded in mode A. Increase of the ferrite component in the weld can be an indirect indication of a more intensive initiation of the centers of ferrite solidification, that may be due to presence of oxides in the weld, which contain vanadium and aluminium, known [5] to be ferritizers.

In [6] it is shown that structure formation in the joint zone of the parts in flash-butt welding is essen-

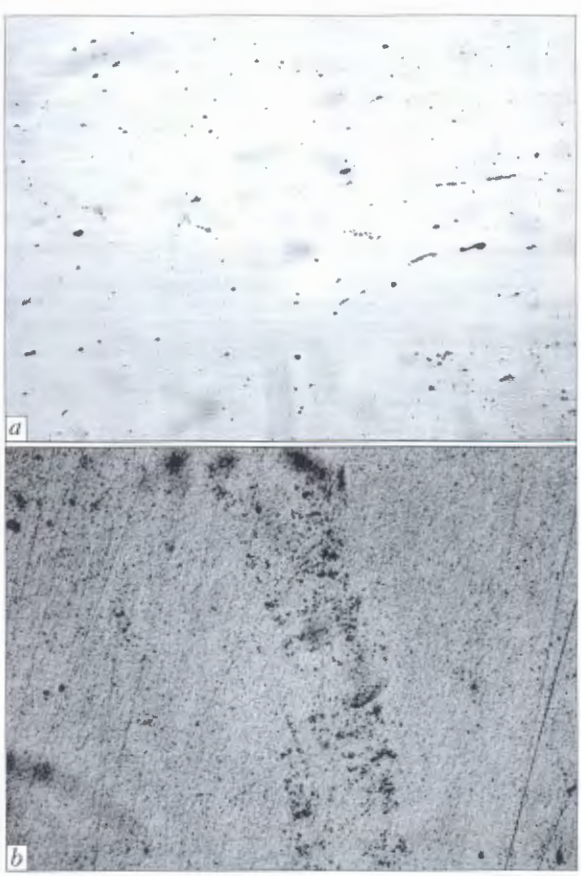

Figure 1. NMI in pipe steels of batch #1 (*a*) and 2 (*b*) (×250)

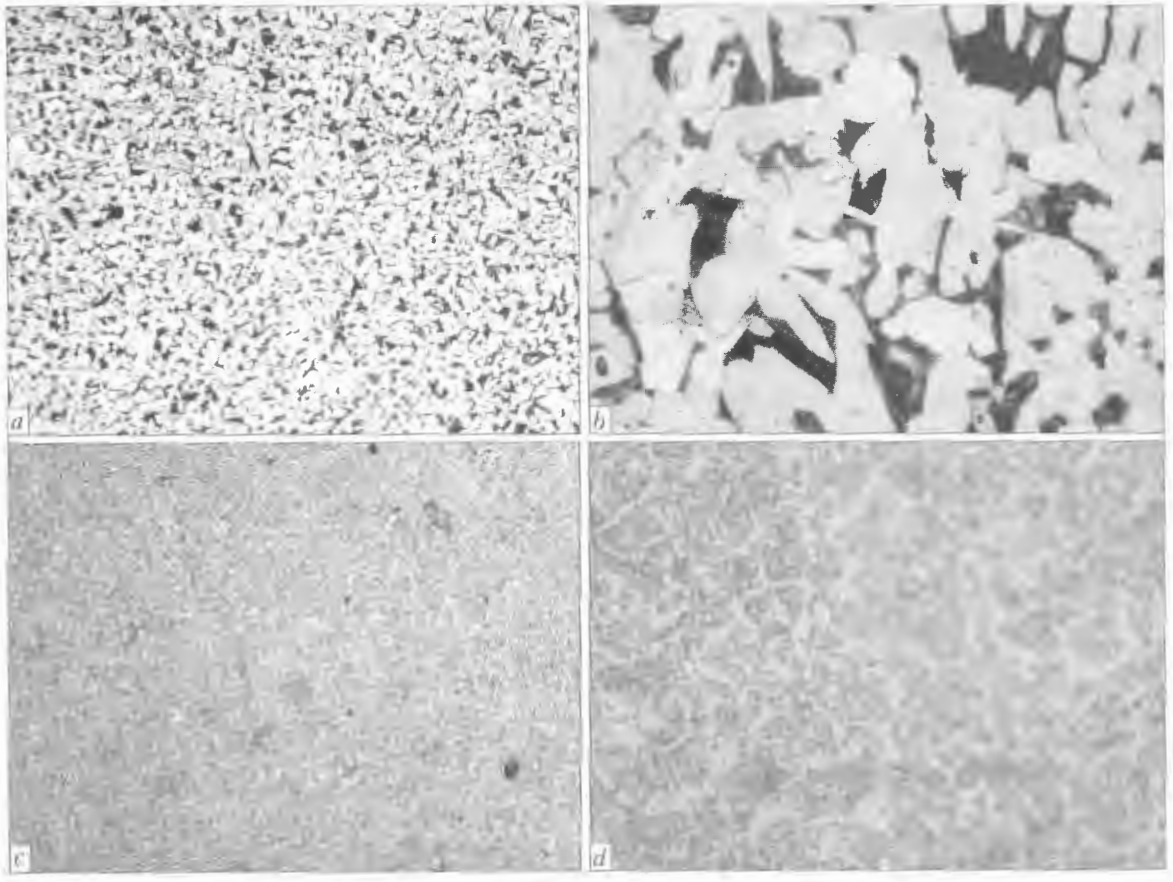

Figure 2. Microstructure of steel of pipes of batch #1 (*a, b*) and 2 (*c, b*) (*a, c* – ×100; *b, d* – ×500)

tially influenced by the condition of the liquid metal melt formed at flashing of the contacting parts. Formation of sound joints is possible with such flash-butt welding parameters, when the melt does not have

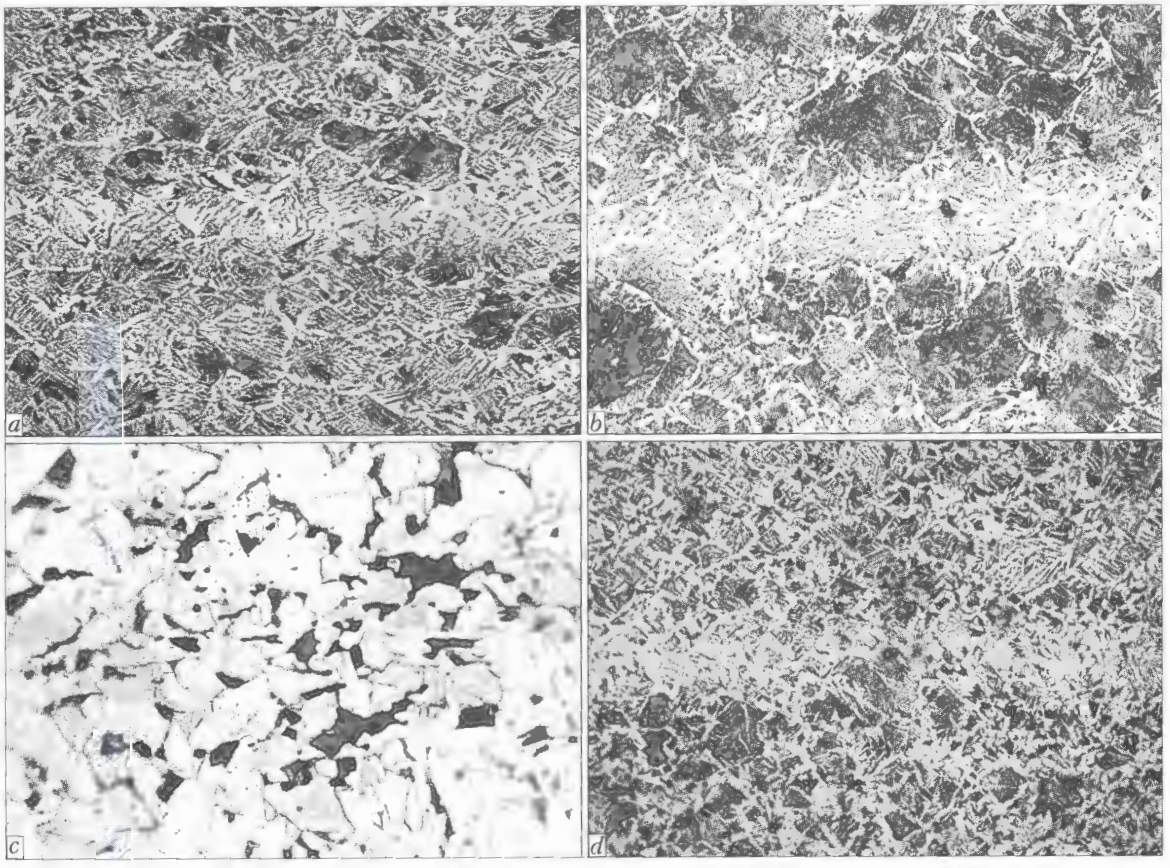

Figure 3. Microstructure of joints of pipes of batch #1 (*a, c*) and 2 (*b, d*); *a, b* – mode A; *c, d* – mode B (*a, b, d* – ×100; *c* – ×500)

Table 4. Chemical element content in NMI in different sections of joints of batch #2 pipes, wt.%

Joint section with NMI	Si	Al	Mn	Fe	V	O
Inclusions in the weld (Figure 3, *c*)	5.482–24.052	0.300–0.826	2.698–26.686	17.792–53.723	0.354–1.066	25.846–36.060
Inclusions in mat spots (Figure 5, *d*)	14.084–31.699	0.655–1.167	15.690–30.428	4.586–22.436	0.584–0.536	28.654–56.919
Lack-of-penetration film (Figure 5, *c*)	1.054	0.220	0.753	96.076	0.082	1.665

enough time to solidify by the moment of deformation of the edges of parts being welded. In this case its greater part is pressed out of the butt, and part remains in the butt, forming a structure with a ferritic fringe along the grain boundaries. The melt and its remains in the weld, respectively, have a higher content of oxygen. Therefore, the metal in the zone of the ferrite fringe, on the whole, has lower mechanical properties compared to adjacent sections. Presence of elements in the steel forming refractory oxide films on the melt surface, removal of which during the upsetting process is difficult, leads to preservation of oxide films in the weld structure, formation of which greatly depends on the content of oxide structures in the melt. Separate NMI form at a small content of oxides.

The ferrite band of joints of batch #1 pipes was found to have separate NMI of a globular shape (Figure 3, *a*), that of batch #2 — numerous NMI precipitates located not only in the joint plane, but also along the grain boundaries in near-contact regions (Figure 3, *b, c*). By composition, they are iron-manganese silicates containing aluminium and vanadium (Table 4).

Table 5 gives the results of mechanical testing of joints of pipes from both the batches, welded in mode A. Indices of testing samples of batch #1 are quite close to similar indices of testing base metal samples. Mechanical properties of joints of batch #2 pipes are much lower than those of the base metal. All the samples of this batch failed through the joint zone — the ferrite band. At visual inspection of fracture surface it is possible to see the characteristic sections, differing by their macro- and microstructure. In the sections, where a metallic bond is present, the fracture has coarse-crystalline structure (Figure 5, *a*, section 1). In the points of absence of the crystalline fracture the joint passes through a monolithic oxide film (see Figure 5, section 2). At flash-butt welding such a joint is classified as lack-of-penetration and features a low ductility and strength. Depending on the composition, the oxide films can have different colour, which distinguishes them on the fracture surface. Fractures of samples of batch #2 had sections, featuring a fine-grained structure (Figure 5, *a*, section 3). Fractographic studies of sections 1–3 show that in section 1 (Figure 5, *b*) a structure of transcrystalline cleavage characteristic for brittle fracture is observed. The structure of section 2 (Figure 5, *c*) is a monolithic oxide film of more than 20–30 μm thickness with inclusions of complex silicate-based oxides. Section 3 is characterized by pitting fracture. The shallow pits contain mainly fragments of the broken oxide film, the thickness of which does not exceed 10–20 μm, (Figure 5, *d*). Fine pits with small fracture ridges are indicative of plastic deformation of the metal in this section at the moment of crack initiation. At visual inspection these sections of fracture surface are coloured from grey to mat, irrespective of the steel composition. In practical application of flash-butt welding they are defined as «mat spots» (MS). At a small area of MS relative to the sample cross-sectional area, their influence on the static tensile testing indices is comparatively low.

Samples of batch #1 failed beyond the plane of weld and HAZ at standard mechanical testing, so that investigations were conducted on fractures of samples with notches along the welding line. Analysis of the obtained data shows that separate globular inclusions, close to those in the base metal, were found in the fractures of batch #1 samples. At testing of welded joints of batch #2 the lowest indices were observed in samples where oxide films and MS of a large area were found. Unlike NMI in batch #1 samples, they form as extended films in the joint plane, the area of which is equal to 10 to 60 % of its surface. According to the data of X-ray microprobe analysis (Table 4), the composition of oxide films includes, in addition to iron and silicon, also aluminium and vanadium, which are not the controlled elements for this steel. Vanadium content in the oxide film of MS is almost 70–100 times higher than its average value in steel.

The given data suggest that oxides containing aluminium, silicon, magnesium and vanadium in the steel composition have a predominating influence on formation of oxide films and MS in welds on batch #2

Figure 4. Macrosections of pipe welded joints (×2): *a* — batch #1, mode A; *b* — batch #2, mode A; *c* — batch #2, mode B

Table 5. Mechanical properties of base metal (BM) and joints of pipes of both the batches

Welding mode	Pipe batch #	σ_y, MPa		σ_t, MPa		δ, %	
		BM	Weld	BM	Weld	BM	Weld
A	1	394–398 / 397	388–391 / 390	559–565 / 564	555–563 / 557	22–24 / 23	21–23 / 22
	2	411–418 / 415	–	543–547 / 545	176–349 / 275	31–33 / 32	–
B	2	–	408–414 / 412	–	531–537 / 534	–	29–31 / 30

Table 5 (cont.)

Welding mode	Pipe batch #	KCV_{+20}, J/cm^2		Bend angle, deg	Nature of defects in the weld
		BM	Weld	Weld	
A	1	121–153 / 150	30–51 / 45	120	Defects are absent
	2	249–263 / 259	–	10–20 / 15	Oxide films of 10–40 mm^2 area and mat spots
B	2	–	32–63 / 59	120	Defects are absent

pipes. A combination of these elements leads to formation of complex low-melting oxides, the subsurface layer of the melt of which in welding contains refractory oxide films, which hinder oxide removal at upsetting. In the areas of oxide accumulation in steel (see Figure 1, *b*) the probability of oxide film formation is the highest. In welding of individual samples of batch #2 pipes, where vanadium content did not exceed 0.02 %, joints without defects in the joint plane were made in the same mode A, which was developed for pipes manufactured in 1990s, of a composition similar to that of the studied batch #1.

Work on improvement of mode A was conducted with a view to welding currently manufactured pipes, characterized by a high content of NMI. It was aimed at development of the methods of increasing the concentration of heating at melting of near-contact metal layers in combination with their high-speed deformation, ensuring a shortening of the duration of liquid melt solidification on the melting surface and its interaction with the air environment of the spark gap. This required development of a new system of controlling the flashing process and modification of some components of K584 welding machine. The conducted investigations resulted in development of welding mode B (see Table 1), providing sound joints of pipes of batch #2. Compared to mode A, it features a shorter duration of the welding process, higher energy concentration at flashing, and increased upsetting speed. Welded joints feature a shorter extent of the HAZ (see Figure 4, *c*), decrease of the grain point and width of the ferrite band (see Figure 3, *d*). Mechanical properties of welded joints of batch #2 are in compliance with the codes, and defects of oxide film type are absent in the fractures (Table 5, mode B).

Obtained results are indicative of a sufficient adaptability of the flash-butt welding technology to changes of the welded steel metal structure, in particular its content of NMI. They, however, do not provide a basis for elimination of control of NMI content in steels at determination of the welding modes and technologies. Particularly dangerous is the presence of segregation of inclusions, shown in Figure 1, *b*. In welding pipe samples in the sections, where segregations penetrated into the welded joint zone, it was not possible to ensure stable indices of mechanical tests even using the improved welding mode B and subsequent heat treatment. In the points of segregations coming to the joint zone oxide films of a large area were observed. To produce a stable quality of welded butt joints of the considered steels limitation of the content of some NMI, in particular, those with a high melting temperature, appears to be the most rational measure for critical structures. For instance, lowering of vanadium content in steels of batch #2 pipes from 0.05 to 0.02 % would allow welding these pipes in mode A specified by the codes with large allowances for the change of operating conditions without refitting and upgrading the welding equipment. This solution was used by some enterprises of the oil and gas industry of RF.

CONCLUSIONS

1. Presence of NMI in carbon and low-alloyed steels containing elements, which form high-melting oxide structures, impairs their weldability in flash-butt welding.

2. Modes of welding the above steels, established by the codes, require correction in the case of an increased content of uncontrollable impurities of metallurgical production in the steel, particularly those containing titanium, vanadium and calcium.

3. A technology of welding pipes of the studied steels with an increased NMI content was developed, which provides mechanical properties of welded joints meeting the code requirements.

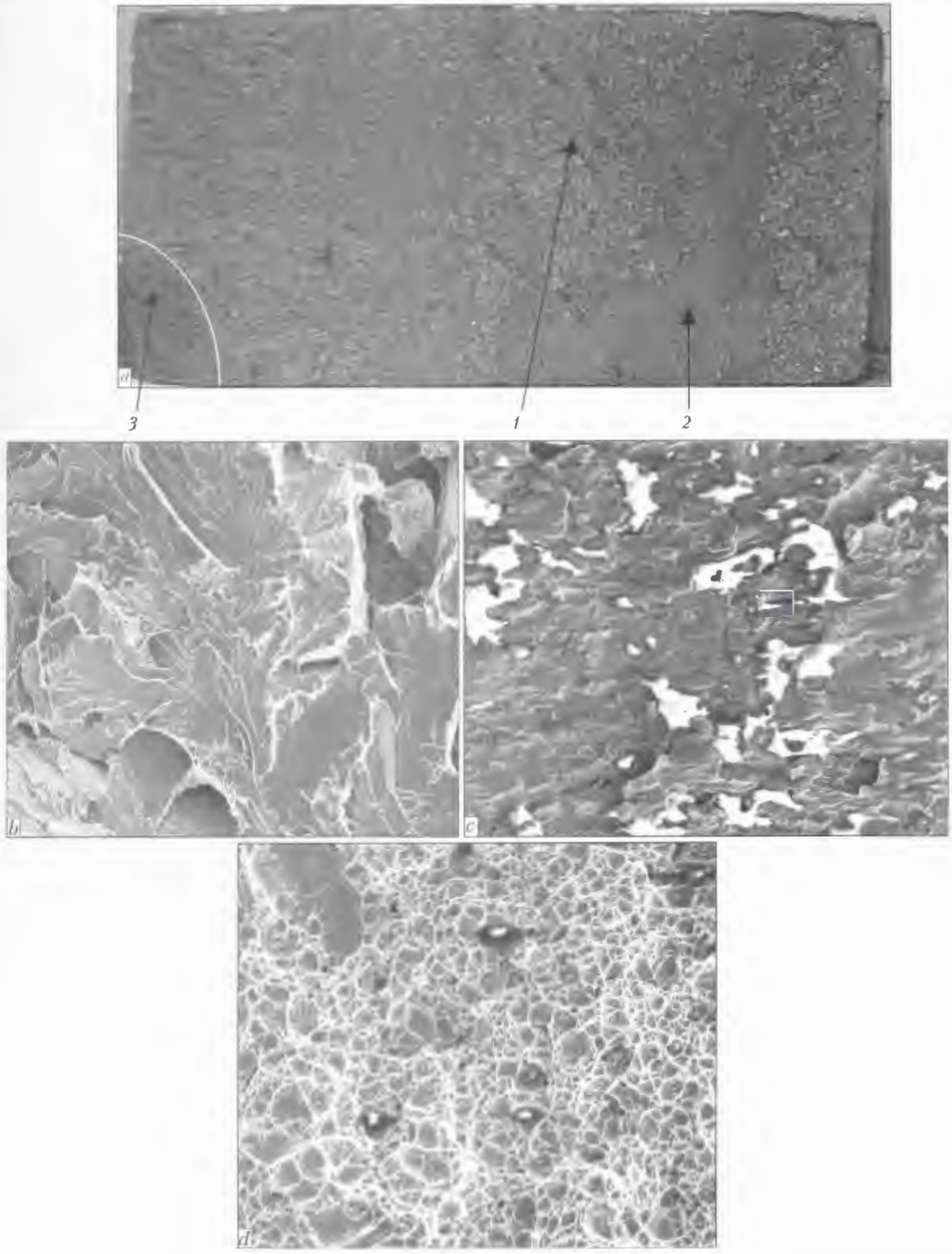

Figure 5. Fracture surface (×6) of joints of batch #2 pipes welded in mode A (*a*), and fractographic pattern (×300) in individual sections: *1* — coarse-crystalline structure; *2* — oxide film; *3* — mat spots

4. In manufacture of critical parts it is rational to monitor the rolled stock, supplied for welding, in order to determine local NMI segregations in it.

1. Kalinnikov, E.S. (1976) *Cold-resistant low-alloy steel*. Moscow: Metallurgiya.
2. Kuchuk-Yatsenko, S.I., Krivenko, V.G., Sakharnov, V.A. et al. (1986) *Flash-butt welding of pipelines*. Kiev: Naukova Dumka.
3. *VSN 006–89*: Construction of main and field pipelines. Welding. Moscow: Minneftegazstroj.
4. Kuchuk-Yatsenko, S.I., Kharchenko, G.K., Falchenko, Yu.V. et al. (2000) Features of ferrite band formation in vacuum pressure welding of steel. *The Paton Welding J.*, **6**, 10–15.
5. Lakhtin, Yu.M. (1983) *Metals science and heat treatment of metals*. Moscow: Metallurgiya.
6. Kuchuk-Yatsenko, S.I. (1992) *Flash-butt welding*. Kiev: Naukova Dumka.

SELECTION OF TECHNOLOGIES FOR REPAIR OF DEFECTS IN ACTIVE MAIN PIPELINES

V.I. MAKHNENKO, E.A. VELIKOIVANENKO and **O.I. OLEJNIK**
E.O. Paton Electric Welding Institute, NASU, Kiev, Ukraine

Repair technologies for removal of defects in main pipelines require substantiation for characteristic typical cases of fitness for service. For this, corresponding calculation algorithms are developed to determine the risk of failure of a repaired defect depending upon its size, repair method and operational conditions. The study describes the developed approach by an example of selection of the technology for repair of cracks.

Keywords: *main pipelines, safe operation, technical diagnostics, detected defects, selection of repair technology, leakproof sleeve, band, calculation algorithms, Monte-Carlo method, failure probability, fitness for service*

Ensuring a stable and safe operation of main pipelines is one of the key challenges at pipeline transport all over the world, including Ukraine, where the volumes of gas and oil annually transported via pipelines amount to 120 billion cubic metres and over 40 million tons, respectively. Stability related to the reliability of functioning of pipelines is determined, first of all, by safe operation of a pipeline, which is provided by the opportune measures on technical diagnostics of its state and appropriate repairs of detected defects. Among a large number of methods available for repair of pipelines, most attractive are the methods which do not require withdrawal of a pipeline (its part) from operation. Available are many approaches, which can be used to solve such problems, including with application of welding technologies [1–3]. The American Petroleum Institute developed a special standard [4] for utilisation of welding for repair of some local defects in active pipelines. Extensive work in this area has been performed in the last years by the E.O. Paton Electric Welding Institute of the NAS of Ukraine [1, 2, 5, 6]. Some of such developments have received recognition by corresponding specialists, and are used in practice [3].

Nevertheless, there are many issues related to utilisation of welding technologies that remain insufficiently studied. First of all, this applies to the remaining safe operation of pipelines repaired under the specified conditions, as specifics of the repair operations imposes a number of limitation on parameters of the welding technologies, shape and size of design solutions. Here it is often impossible to keep to the general recommendations (standards) used for welding repair of such structures under conventional conditions, i.e. withdraw them from operation and subject to required preparation for welding. Therefore, the evidence of fitness for service is of high importance for such technologies, allowing for specific loading on the repaired part of a pipeline.

The purpose of this study was to develop the calculation procedure, which would make it possible to estimate with a certain degree of conservatism the fitness for service of pipeline regions (on the basis of the safe operation condition) after applying the characteristic repair methods [3] related to removal of detected inadmissible defects.

Discontinuities of the crack type in a material are among the most dangerous defects. Such defects may be of the surface (on the external or internal surface of a pipe), through or sub-surface type (the latter are rarely found in main pipelines of conventional thicknesses). Selection of the repair method for such defects begins, as a rule, from estimation of the possibility of transforming a defect from the type of the inadmissible crack to a volumetric defect of the groove type [7], located along the generating line (defect length — s) or along the circumference (defect length — c) at measurement depth δ_{meas} (Figure 1).

Admissibility of this type of defects is estimated with allowance for a predictable decrease in thickness as a result of corrosion, using relationships taken from [7, 8]:

$$Y = \delta_{meas} - \{[\delta]R_j + v_{cor}t\}, \quad j = s, \quad c > 0, \qquad (1)$$

where

$$R_j \geq 0.2 \text{ at } \lambda = \frac{1.285s}{\sqrt{D[\delta]}} \leq 0.3475, \quad \frac{c}{D} \leq 0.348;$$

$$R_s = f(\lambda) \text{ at } 0.3475 < \lambda < 10;$$

$$R_c = \frac{-0.7568 + 10.511(c/D)^2}{1.0 + 13.838(c/D)^2} \text{ at } \frac{c}{D} > 0.348;$$

$$R_s \geq 0.885 \text{ at } \lambda \geq 10;$$

R_j is the admissible decrease in value $[\delta]$; D is the pipe diameter; $[\delta]$ is the minimum permissible thickness of a pipe, based on utilisation of the calculation code for a given region of intact pipe (ignoring corrosion); and v_{cor} is the rate of corrosion for a predicted range of time t of the operation till the next diagnostics.

Condition $Y > 0$, according to (1), determines admissibility of the detected defect. If $Y < 0$, i.e. the groove-like defect of a given size is inadmissible, it is necessary to apply the corresponding technologies to

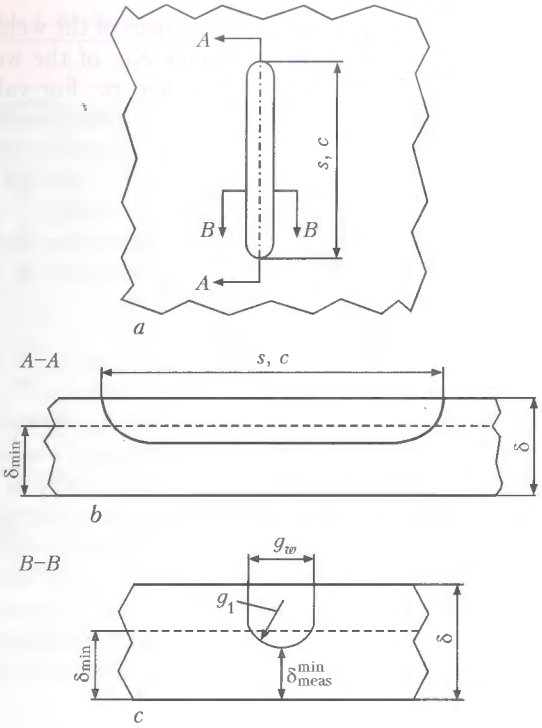

Figure 1. Schematic of elongated volumetric defects (groove-like defects): *a* – groove-like defect (top view); *b*, *c* – length (section *A*–*A*) and width (section *B*–*B*) of groove-like defect

remove it, such as repair welding or installation of a band (Figure 2).

In a case where the band takes up a substantial part of force loading [3], condition (1) can be replaced by

$$Y = \delta_{meas} - v_{cor}t. \qquad (2)$$

Relationship (2) corresponds to the condition of formation of a through corrosion defect. It can be seen that unloading of the groove-like defect zone, i.e. removal of summand $[\delta]R_j$ from (1), may formally cause a dramatic increase in time t up to formation of a leak. Allowing for substantial stochasticity of the δ_{meas} and v_{cor} values, it is more correct to make such estimations for time t in the probability form, as it is suggested, e.g. in [9].

Figure 3 shows failure probabilities P against time t, which were plotted by using the failure probability calculation procedure based on the Monte-Carlo method at the preset truncated normal laws of distribution of the δ_{meas} measured values and corrosion rate v_{cor}.

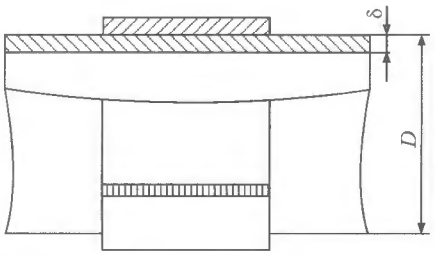

Figure 2. Schematic of the band used to repair corrosion-mechanical damages on the pipe wall with depth of up to 50 % of its thickness [3]

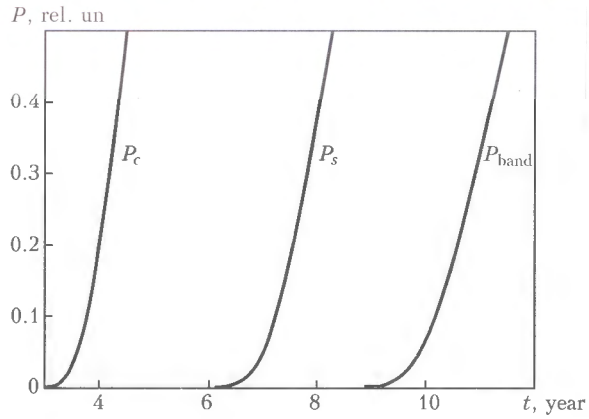

Figure 3. Calculated failure probability against time t from the beginning of the corrosion process for a groove-like defect along the generating line, P_s, and along the circumference, P_c, at the absence of band and after installing it, P_{band}, at time moment $t = 0$

The following values are assumed in the truncated normal distribution law, which is characterised by standard deviation ξ and lower deviation limit A, as the input data for δ_{meas}, s, c and v_{cor}, i.e. mean values $\bar{\delta}_{meas}$, $\bar{s}$, $\bar{c}$ and $\bar{v}_{cor}$: $\bar{s} = 40$ mm, $\bar{c} = 500$ mm, $\bar{\delta}_{meas} = 11.5$ mm, $\xi_\delta = 0.5$ mm, $\xi_s = 2$ mm, $\xi_c = 5$ mm, $\bar{v}_{cor} = 1.0$ mm/year, $\xi_v = 0.1$ mm/year, $A_\delta =$

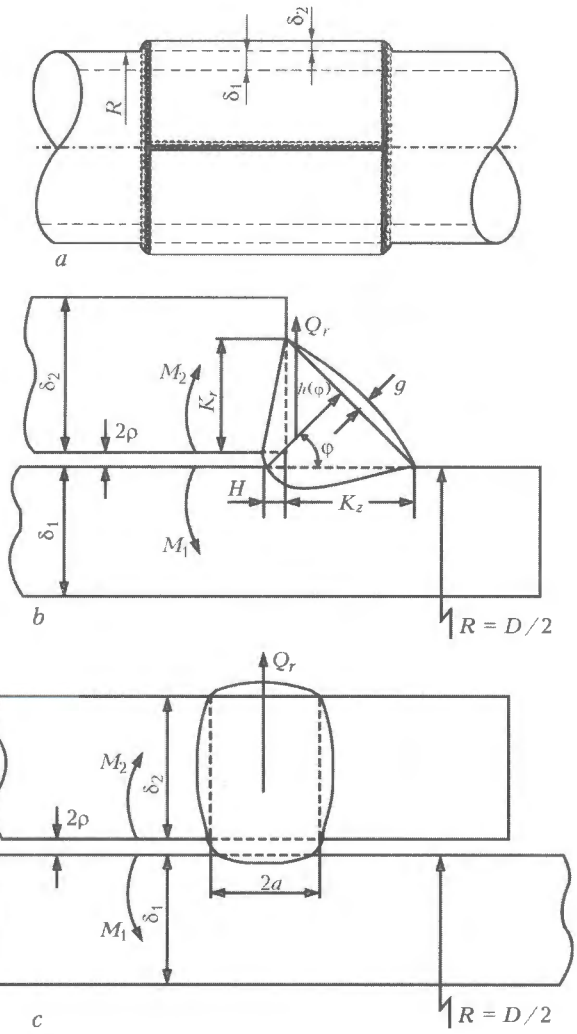

Figure 4. Schematic of the leak-proof sleeve (*a*) and loading the fillet (*b*) and slot circumferential welds (*c*) by working pressure in a cavity between the sleeve and the pipe

= 10.5 mm, and A_v = 0.8 mm/year. Curves P_s and P_c determine increase in the failure probability for the cases of a polished crack along the generating line (with length $\bar{s}$ = 40 mm) and along the circumference (with length $\bar{c}$ = 500 mm), based on criterion (1) at D = 1420 mm and [δ] = 16 mm.

It can be seen that the failure probability will be $P_c \approx 0.2$ after 4 years of operation of such groove-like thinnings in the presence of corrosion. However, at t = 4.5 years, the probability failure will be $P_c \approx 0.5$, i.e. reliability of this type of repair of external cracks of the corresponding sizes will be low.

Curve P_{band} in Figure 3 determines the failure probability for the same defects against time, allowing for installation of the band, which is capable of taking up a substantial part of loading, i.e. here only corrosion is taken into account by criterion (2). It can be seen that the band considerably decreases the failure probability against time. Nevertheless, after t = = 10 years from the beginning of the corrosion process, the failure probability is above 0.1, which is undesirable in many cases. From this standpoint, it is more reliable to use a leak-proof sleeve (Figure 4), which makes it possible to maintain performance after formation of a through defect. Failure probability P_2 for this variant of repair is determined as product

$$P_2 = P_1 P_{1,2}, \tag{3}$$

where P_1 is the probability of formation of a through defect with time as a result of corrosion, allowing for relationship (2); and $P_{1,2}$ is the probability of failure of the sleeve on a condition of the working gas pressure present between the sleeve and the pipe.

The failure criterion in this case, according to [5], is related to performance of welded joints used to join the sleeve to the pipe. The probability of tear of a fillet or slot weld (Figure 4) can be related to the criterion of brittle-tough fracture by the mechanism of spontaneous propagation of a sharp cavity adjoining the weld in the case of a working pressure formed in it:

$$\begin{aligned} Y &= -K_r + (1 - 0.14L_r^2)\,[0.3 + 0.7\exp(-0.65L_r^6)] \\ &\text{at } L_r \le L_r^{\max} = \frac{\sigma_y + \sigma_t}{2\sigma_y}, \\ &\text{at } L_r > L_r^{\max} \quad Y = -K_r, \end{aligned} \tag{4}$$

where K_r characterises the purely brittle fracture of the weld, $K_r = K_I/K_{IC}$ (K_I is the stress intensity factor in the weld metal under the given loading; K_{IC} is the fracture toughness of the weld metal); L_r = = σ_{ref}/σ_y characterises the purely tough fracture of the weld metal as a result of plastic instability, where σ_{ref} is determined, e.g., from the Mises theory through the stress tensor components in the weld metal under the given loading.

Study [5] describes the method for determination of values K_I and σ_{ref} through bending moments M and intersecting forces Q_r acting on a unit length of the circumferential weld (Figure 4). At a fixed working pressure in the cavity, the sufficiently stochastic values are the calculated geometrical sizes of the weld – h or $2a$, brittle fracture resistance K_{IC} of the weld and its mechanical properties σ_y and σ_t. For values $X = h, a, \sigma_y$ and σ_t, it is convenient to use the truncated normal law of distribution of these random values, which is determined by mean value X, standard deviation ξ_X and lower truncation limit A_X [9].

For the K_{IC} values, the Weibull distribution is more acceptable, according to which the probability is

$$p(K_{IC}) = 1 - \exp\left[-\left(\frac{K_{IC} - K_0}{K_d - K_0}\right)^{\eta}\right], \tag{5}$$

where K_0, K_d and η are the distribution parameters, which are usually determined over the results of 12-15 experiments [8], from which K_{IC} is calculated at p = = 0.5, 0.05 and 0.95. Then, by substituting the values of K_{IC} and p to equation (4), we obtain the system of three non-linear equations, from which we find the values of Weibull parameters K_0, K_d and η.

Consider the generator of random numbers Z within $0 \le Z \le 1$, and condition of adequacy of initial value X in the following form:

$$Z = \int_{A_X}^{X} \bar{\varphi}_X dX = P(X), \tag{6}$$

where $\bar{\varphi}_X$ is the normalised distribution law for value X; and $P(X)$ is the probability of value X.

Using relationship (6), we obtain the possibility to generate sampling of variants by Y for the Monte-Carlo method. Representativeness of the sampling is checked by increasing the quantity of variants N until mean value Y, standard deviation ξ_Y = $= \left[\frac{1}{N}\sum_{n}^{N} (Y - \bar{Y})_n^2\right]^{0.5}$ and failure probability $P_{1,2}$ remain almost unchanged. Failure probability $P_{1,2}$ is determined by the following relationship:

$$P_{1,2} = \int_{-A_Y}^{0} \varphi_{\bar{Y}} dY, \tag{7}$$

where $\bar{\varphi}_Y$ is the normalised law of distribution of value Y for the representative sampling.

Below we present the calculations of failure probability $P_{1,2}$ for the sleeve with the fillet and slot weld depending upon the thickness of the sleeve wall, δ_{sl}, at length $2L$ = 1000 mm for the fillet weld and $2L$ = = 1000 + 2·100 mm for the slot weld.

Table 1 gives corresponding variants of the calculations for different sizes h (of the fillet weld at $h(\varphi)$ = = const) and $2\bar{a}$ (of the slot weld) by indicating bending moment M and intersecting force Q_r in the weld metal formed at working pressure $P_{w.p}$ = 5.5 MPa.

Respectively, according to [5, 8], for the fillet weld

$$K_I = 4.295\frac{M}{h^{3/2}} + 0.5369\frac{Q_r}{\sqrt{h}}, \quad \sigma_{ref} = \frac{4M}{h^2} + \frac{Q_r}{h}, \tag{8}$$

Table 1. Results of calculation of geometrical parameters for leak-proof sleeve

δ_{sl}, mm	Fillet welds						
	$\bar{h}$, mm	M, MPa·mm^2	Q_r, MPa·mm	$\bar{K}_I$, MPa·mm$^{1/2}$	$\bar{\sigma}_{ref}$, MPa	$P_{1,2}$	
						I	II
20	12	13780	274	46.4	405.6	0.3670	1.0
20	20	23435	319	36.8	250	0.0837	0.867
28	20	25174	345	39.5	269	0.2300	0.969
28	22	27160	352	37.0	240	0.0450	0.839
28	24	29000	358	34.7	216	0.0030	0.577
28	26	30656	362	32.6	195	0	0.295
28	28	32120	370	30.6	177	0	0.188
28	–	–	–	–	–	–	–

Table 1 (cont.)

δ_{sl}, mm	Slot welds						
	$2\bar{a}$, mm	M, MPa·mm^2	Q_r, MPa·mm	$\bar{K}_I$, MPa·mm$^{1/2}$	$\bar{\sigma}_{ref}$, MPa	$P_{1,2}$	
						I	II
20	–	–	–	–	–	–	–
20	–	–	–	–	–	–	–
28	22	36915	447	38.5	327	0.7100	1.0
28	24	37160	425	34.1	277	0.1730	0.9370
28	26	37351	405	30.4	238	0.0048	0.5310
28	28	37492	388	27.4	206	0	0.1090
28	30	37590	374	24.8	181	0	0.0045
28	32	37661	361	22.6	159	0	0

and for the slot weld

$$K_I = 1.129\frac{M}{a^{3/2}} + \frac{Q_r}{\sqrt{\pi a}}, \quad \sigma_{ref} = \frac{M}{a^2} + \frac{Q_r}{2a}. \qquad (9)$$

The data of Table 1 on the bending moments in the weld correspond to mean values h and $2\bar{a}$. The Table also gives mean values K_I and $\bar{\sigma}_{ref}$, as well as results of calculation of $P_{1,2}$. Stochasticity of the h, a, K_{IC}, σ_y and σ_t values was taken into account. It was assumed that $\xi_h = 0.5$ mm, $A_h = h - 2\xi_h$, $\xi_a = 0.5$ mm, $A_a = \bar{a} - 2\xi_a$, $\bar{\sigma}_y = 270$ MPa, $\bar{\sigma}_t = 470$ MPa, $A_{\sigma_y} = 230$ MPa, $A_{\sigma_t} = 435$ MPa, and $\xi_{\sigma_y} = \xi_{\sigma_t} = 20$ MPa. For K_I, two variants of the values were used: I — $K_d = 107.5$ MPa·m$^{1/2}$, $K_0 = 20$ MPa·m$^{1/2}$ and $\eta = 4.0$, as for the base metal; and II — same as variant I, but $K_d = 42$ MPa·m$^{1/2}$.

It can be seen from the data of Table 1 that the fillet welds have some advantage in volume of the deposited weld metal, sleeve wall thickness δ_{sl} being the same. For example, at $\delta_{sl} = 28$ mm and $h = 2a = 28$ mm, the volume of the deposited metal per unit length of the fillet weld is $V_f \approx \pi h^2/4 = \pi\delta_{sl}^2/4 \approx 0.785\delta_{sl}^2$, and that per unit length of the slot weld is $2a\delta_{sl} = \delta_{sl}^2$. In addition, the fillet welds have an advantage in reliability, i.e. the risk of $P_{1,2}$ is lower in this case at the same values of $h = 2a$.

Allowing for the obtained values of $P_{1,2}$, it is possible to plot failure probability $P_2 = P_1P_{1,2}$. It can be seen that, compared with the band (see Figure 3), the use of the leak-proof sleeve can markedly reduce risk P_2, especially for the heavy sleeves, where $P_{1,2} \rightarrow \rightarrow 0$. It should be noted that, compared with study [5], where the deterministic approach was used at $K_I = 1000$ MPa·mm$^{1/2} = 31.6$ MPa·mm$^{1/2}$, which corresponds to $p(K_{IC}) < 0.05$, the probability approach used in the present study gives less stringent requirements for sizes of the welds, at which $P_{1,2} \approx 0$.

The considered variants of repair of a crack without withdrawing the pipeline from operation are inapplicable for cracks on the internal surface of the pipeline, as it does not provide for removal of metal from the crack zone to prevent the propagation of cracks during operation.

For such cases, study [3] suggests a variant of repair by using the structure which is characteristic of making of branch pipes on active pipelines. The structure consists of welded-on sleeve *2* with a hole (Figure 5), to which branch pipe *3* and flange *4* are preliminarily welded. The mechanism for removal of the zone with diameter d, within which crack *5* is

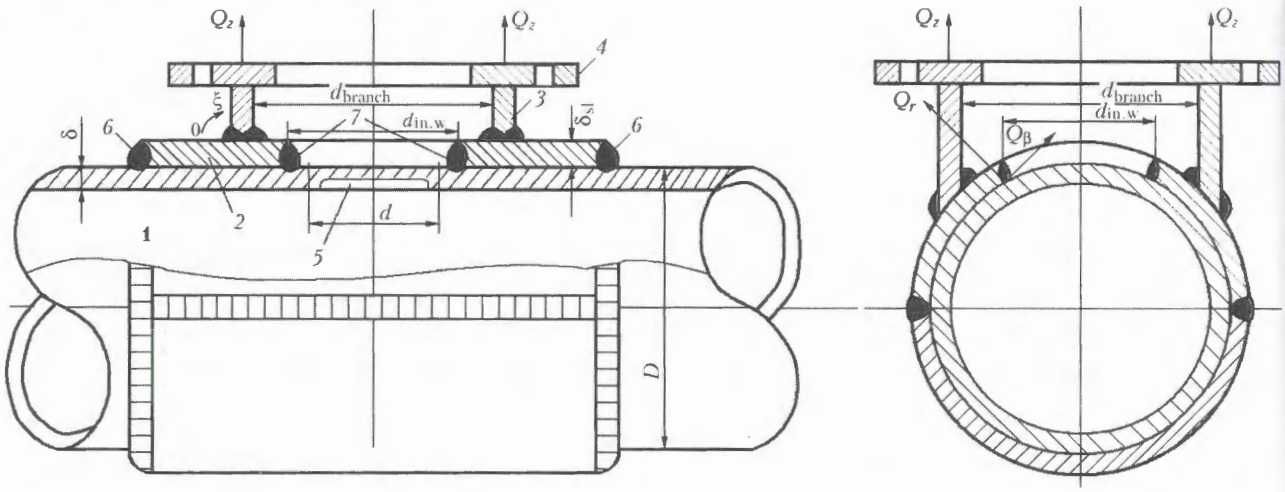

Figure 5. Schematic of the structure for removal of cracks and other defects from the internal surface of active pipeline: *1* — pipeline; *2* — sleeve; *3* — branch pipe; *4* — flange to fix the mechanism for removal of the zone with a crack and plugging the branch pipe; *5* — crack; *6*, *7* — external and internal welds, respectively, used to weld on the sleeve

located, is fixed to the flange. If the sleeve is welded to the pipe only with external circumferential welds *6*, its reliability will be determined with allowance for the working gas pressure present in the cavity between the sleeve and the pipe, by using the above described algorithm for the leak-proof sleeve. If it is possible to make sound internal weld *7* without external one *6*, in this case reliability of the structure will depend upon the ability of internal weld *7* to withstand the pressure in the branch pipe, i.e. intersecting forces Q_z will act on a unit length of the internal weld. In this case

$$Q_z = \frac{P_{w.p}(\pi d_{branch}^2)/4}{\pi d_{in.w}} \eta(\xi), \qquad (10)$$

where $P_{w.p}$ is the working pressure; $\eta(\xi)$ is the function of distribution of Q_z along the weld; d_{branch} is the diameter of the branch pipe; and $d_{in.w}$ is the diameter of the internal weld.

The maximal value of $\eta(\xi)$, according to [10], occurs in a cross section of the pipe coinciding with axis of the branch pipe. If $h/d_{in.w} < 0.2$ and $d_{in.w}/d_{branch} \to 1.0$, the maximal value of $\eta(\xi)$ can be written down as follows:

$$\eta_{max}(\xi) = 0.9 + \frac{10.6 d_{branch}}{D} \times \times \left(1 - 0.4 \frac{\delta + \delta_{sl}}{d_{branch}}\right) + 4.0 \frac{h}{d_{branch}}. \qquad (11)$$

Table 2. Results of calculations of failure probability for internal weld (see Figure 5)

d = 500 mm		d = 400 mm		d = 300 mm	
$\bar{h}$, mm	p	$\bar{h}$, mm	p	$\bar{h}$, mm	p
14.0	0.00054	10.0	0	6.0	0
13.0	0.02570	9.0	0.00360	5.5	0.00334
12.0	0.20900	8.0	0.18900	5.0	0.12000

Considering the above limitation, we obtain the following instead of (10):

$$Q_z^{max} = P_{w.p} \frac{d_{branch}}{4} \times \times \left[0.9 + \frac{10.6 d_{branch}}{D}\left(1 - 0.4 \frac{\delta + \delta_{sl}}{d_{branch}}\right) + 4.0 \frac{h}{d_{branch}}\right]. \qquad (12)$$

Decomposition of vector Q_z into components along radius r and weld circumference β yields

$$Q_r^{max} = Q_z^{max} \sqrt{1 - (d/D)^2}, \quad Q_\beta^{max} = Q_z^{max} \frac{d}{D}. \qquad (13)$$

Modes I and II of the stress intensity factor, determined by value Q_r^{max} for K_I and Q_β^{max} for K_{II} will take place, respectively, at the apex of the welded cavity adjoining the internal weld.

For low d_{branch}/D ratios, which is characteristic of the given procedure for repair of internal cracks of a relatively small length, the value of Q_r^{max} will differ but insignificantly from that of Q_z^{max}, according to (13), this making it possible to use relationships (8) to calculate K_I and σ_{ref} at $M = 0$.

The risk of spontaneous growth of the sharp cavity adjoining the internal weld is determined by criterion (4), allowing for stochasticity of the initial value by h, K_{IC}, σ_y and σ_t. Table 2 gives the results of this calculations for D = 1420 mm, δ = 19 mm and δ_{sl} = = 28 mm at d = 500–300 mm, depending upon the leg of the fillet weld, h, at the absence of welds *6*. It can be seen from the Table that the repair structure for removal of cracks from the internal surface of a pipeline is characterised by a sufficiently high reliability, provided that the h value, i.e. cross section of the weld joining the sleeve to the pipe, is properly selected (see Figure 4). The higher the d_{branch}/D ratio, the higher should be the h values to ensure the required reliability.

It should be noted that sleeve wall thickness δ_{sl} within $\delta \le \delta_{sl} \le 1.5\delta$ has an insignificant effect on the failure probability at the absence of the external weld

(see Figure 5). In the presence of the latter, the risk of failure of a structure will be determined by the product of the corresponding failure probabilities from Table 2 by those from Table 1 at corresponding δ_{sl}, i.e. the risk of failure can be reduced even greater.

As noted above, with the Monte-Carlo method used to calculate the failure probability, based on the corresponding criterion of a limiting state

$$Y = f(X) \qquad (14)$$

using random numbers Z, we can form a sampling of combinations of corresponding parameters X, on the basis of which we can derive normalised distribution density $\varphi_Y = \partial P / \partial Y$, the integration of which, according to [8], yields the value of the unknown probability.

To illustrate, Figure 6 shows distribution density $\overline{\varphi}_Y$ for value Y by criterion (4) for a variant of d = = 300 mm and h = 5.5 mm from Table 2, which was obtained on the basis of sampling from $N = 10^4$ combinations of initial parameters X determined by condition (6), like in [9].

Modern computer facilities make it possible to use the values of such samplings without any serious limitations, i.e. reliability of the results obtained is determined primarily by reliability of initial parameters X, which are included into limiting state criterion (14). These are geometrical sizes of characteristic elements (thinnings, cracks, welds) and mechanical properties of a material within the zone of the said characteristic elements. Corresponding recommendations on this issue of technical diagnostics can be found in study [8], and it is planned to consider it in more detail in a separate article.

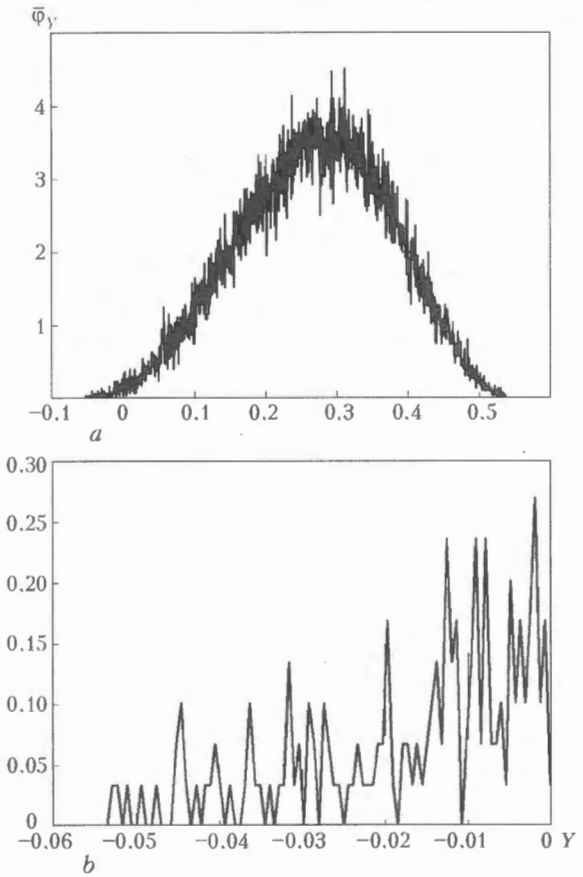

Figure 6. Distribution density $\overline{\varphi}_Y$ for value Y by criterion (4) for a variant of d = 300 mm and h = 5.5 mm (*a*), and more detailed presentation of the «tail» of curve $\overline{\varphi}_Y$ within the $Y \le 0$ zone, where failure probability P is determited (*b*)

CONCLUSIONS

1. Technologies for repair of defects detected in main pipelines without withdrawing them from operation are of high practical interest, but they require substantiation of fitness for service for typical cases.

2. The developed calculation algorithms for estimation of the risk of failure of the repaired defects of the crack type on the internal and external surfaces of a pipeline make it possible to rank the repair technologies depending upon the required fitness for service.

3. The probability approach used as a basis for the calculations makes it possible to allow for spread of the input data on geometrical sizes, mechanical properties and service conditions by the corresponding increase of the risk of failure, thus stimulating the maximal possible accuracy in generating the input data by technical diagnostics.

1. But, V.S., Vasilyuk, V.M., Fedorenko, Yu.T. et al. (2006) Trends in development of repair technologies for main pipelines under service conditions. In: *Proc. of Sci. Seminar on Serviceability of Pipeline Transportation Systems* (Kiev, 11 April, 2006), 31–38.
2. But, V.S., Gretsky, Yu.Ya., Rozgonyuk, V.V. et al. (2001) Substantiation of a new approach for performing welding operations on pipelines under pressure. *Naft. i Gazova Promyslovist*, **4**, 33–39.
3. But, V.S., Olijnyk, O.I. (2006) Strategy of development of repair technologies for active main pipelines. In: *Problems of life and operational safety of structures, constructions and machines*. Ed. B.E. Paton. Kiev: PWI.
4. *API Standard 1104*: Welding of pipelines and related facilities. Appendix II: Welding. Publ. Sept. 1999.
5. Makhnenko, V.I., But, V.S., Velikoivanenko, E.A. et al. (2003) Estimation of permissible sizes of welds for mounting T-joints and sleeves on active main pipelines. *The Paton Welding J.*, **8**, 6–11.
6. Makhnenko, V.I., But, V.S., Velikoivanenko, E.A. et al. (2001) Mathematical modelling of pitting defects in active oil and gas pipelines and development of a numerical method for estimation of permissible parameters of arc welding repair of defects. *Ibid.*, **11**, 2–9.
7. (2000) *Fitness-for-service*. American Petroleum Institute Recommended Practice 579.
8. Makhnenko, V.I. (2006) *Safe service life of welded joints and assembly units on modern structures*. Kiev: Naukova Dumka.
9. Makhnenko, V.I., Velikoivanenko, E.A., Olejnik, O.I. (2008) Risk analysis as a formalization mean for decision-making related to unscheduled repair of welded structures. *The Paton Welding J.*, **5**, 5–10.
10. (1989) *PNAE G-7-002-86*: Norms of strength design of equipment and pipelines for nuclear power plants. Moscow: Energiya.

EFFECT OF THE TYPE OF CONCURRENT GAS FLOW ON CHARACTERISTICS OF THE ARC PLASMA GENERATED BY PLASMATRON WITH ANODE WIRE

M.Yu. KHARLAMOV[1], I.V. KRIVTSUN[2], V.N. KORZHIK[2], S.V. PETROV[2] and A.I. DEMIANOV[2]
[1]V. Dal East-Ukrainian National University, Lugansk, Ukraine
[2]E.O. Paton Electric Welding Institute, NASU, Kiev, Ukraine

Mathematical model is presented, describing the heat and mass transfer processes occurring in interaction of external gas environment with a turbulent flow of the arc plasma generated by plasmatron with an anode wire. Comparative numerical analysis of spatial distributions of heat, gas-dynamic and other characteristics of the turbulent jet of the argon plasma blown about with laminar argon and air flows, as well as emitted into a quiescent gas, was conducted.

Keywords: *arc plasma, plasmatron, anode wire, mathematical model, numerical analysis, turbulent jet, concurrent flow, heat and mass transfer*

In many engineering applications of low-temperature arc plasma, such as heat treatment of surfaces, spraying of coatings, various plasma-chemical and other processes, the turbulent plasma flows formed by electric-arc generators (plasmatrons) are emitted into a gas environment of the composition other than that of the used plasma gas, most often into air. In such cases, the arc plasma flow in an external region may either be a current-free plasma jet (when both arc electrodes are inside a plasmatron) or contain an exposed region of the arc discharge column (e.g. in plasmatrons with an external anode wire [1], which are used for plasma-arc spraying of coatings). Moreover, the plasma flow may be emitted into a quiescent gas environment (submerged jet) or blown about with a concurrent air or shielding (inert) gas flow [1]. In all the cases the composition of the external gas environment (if it differs from that of the plasma gas) exerts a certain effect on characteristics of the arc plasma flow being formed. Therefore, for correct description and mathematical modelling of such flows, it is necessary to allow for mixing of the plasma gas with the external gas environment.

In the majority of available mathematical models of turbulent plasma jets, the latter are considered as being emitted into the gas environment with a composition identical to that of the plasma gas [1–4]. One of few solutions of the problem of adding the ambient gas of a different chemical composition to the turbulent gas jet is given in [5]. It consists in using conditions of similarity of the profiles of excessive temperature and concentration of an impurity. However, this approach does not describe peculiarities of the turbulent diffusion boundary layer in the case of plasma flows considered in this study, and is unacceptable for complex configurations of the flows.

The purpose of this study was to develop a mathematical model to describe gas-dynamics and heat exchange under conditions of the turbulent arc plasma flow, allowing for the processes of convective diffusion, which take place in mixing of the plasma gas with the external gas environment (concurrent gas flow), as well as a corresponding change in the composition, thermal-physical properties and coefficients of transfer of the plasma.

The model developed for calculation of characteristics of the turbulent gas plasma flows in plasmatrons with anode wires, including in the presence of a blowing gas flow [1], was used as a basis for the model suggested. Schematic of the plasmatron considered in this study is shown in Figure 1. The direct current arc is burning between a refractory cathode and current-conducting wire, which is located behind the plasmatron nozzle exit section at distance Z_2 from the initial section of the calculation region ($z = 0$) near the cathode tip. It is assumed that the entire arc current is closed to the wire, and at $z > Z_2$ the plasma flows in a no-current inertia manner. The plasma gas fed at flow rate G_1 to the plasma-shaping nozzle with length Z_1 and radius R_n is heated by the electric arc and flows into the external gas environment. It should be noted that by changing length Z_2 of the arc in parameters of the model, it is possible to model its burning inside the plasmatron nozzle ($Z_2 > Z_1$), which corresponds to the indirect-action plasmatron. The exposed region of the arc plasma flow can be blown about with a coaxial flow of the ambient gas at flow rate G_2. In this case, the blowing gas is fed via the annular channel with $R_1 \le r \le R_2$ (Figure 1) at angle α to the plasmatron axis (it can be assumed that $G_2 = 0$ in modelling of the arc plasma flowing into the quiescent gas). Pressure in the external gas environment is assumed to be atmospheric. If compositions of the plasma gas and external gas environment (blowing gas) are different, they begin mixing at $z > Z_1$.

To describe mixing of the arc plasma flow with the external gas, we made the following assumption, along with the conventional ones used to model similar flows [1, 6]:

• plasma component of the mixture is inert (plasma gas – argon) and does not enter into chemical reactions with the external gas;

• mixing of the plasma gas with the external gas environment of a different composition can be described by equations of convective diffusion, allowing for the turbulent component of the coefficient of mutual diffusion of components;

• when the turbulent plasma jet is blown about with a coaxial laminar flow of the cold gas, this gas has the same composition as the gas environment.

We used the system of magnetogasdynamic (MGD) equations in an approximation of the turbulent boundary layer, written down for the time-averaged values of temperature T, radial $\bar{v}$ and axial u components of the plasma velocity with the corresponding initial and boundary conditions to calculate gas-dynamic, thermal and electric characteristics of the arc plasma generated by the plasmatron under consideration [1]. To determine turbulent components of the coefficients of viscosity and thermal conductivity of the plasma, we used the k–ε model of turbulence, which is described in [1] for the conditions considered in this study. The above system of equations was supplemented with the equation of convective diffusion of the plasma gas in the external gas environment:

$$\rho\left(u\frac{\partial m_1}{\partial z}+\bar{v}\frac{\partial m_1}{\partial r}\right)=\frac{1}{r}\frac{\partial}{\partial r}\left(r\rho\overline{D}_{1,2}\frac{\partial m_1}{\partial r}\right), \quad m_1+m_2=1. \tag{1}$$

Here $m_1(r, z)$ and $m_2(r, z)$ are the relative weight concentrations of the plasma and ambient gases, respectively, in the plasma mixture (here and below, index 1 designates characteristics of the plasma gas, and index 2 – characteristics of the ambient gas), which are determined as follows:

$$m_i=\frac{\rho_i}{\rho}, \tag{2}$$

where ρ_i is the reduced density of components ($i = 1, 2$), which characterises their weight per unit volume of the plasma mixture; ρ is the averaged density of the mixture; and $\overline{D}_{1,2}$ is the coefficient of turbulent diffusion, having the following form:

$$\overline{D}_{1,2}=D_{1,2}+D_t=D_{1,2}+\frac{\eta_t}{\rho \mathrm{Sm}_t}; \tag{3}$$

$D_{1,2}$ is the coefficient of mutual molecular diffusion in the plasma mixture; D_t is the turbulent component of the diffusion coefficient; η_t is the coefficient of turbulent viscosity, determined by using the k–ε model of turbulence [1]; Sm_t is the Schmidt number of turbulence, which was assumed to be equal to one, according to the recommendations given in [4].

The mutual diffusion coefficient for the binary plasma mixture was calculated by the Chapman–Enskog formula [7]:

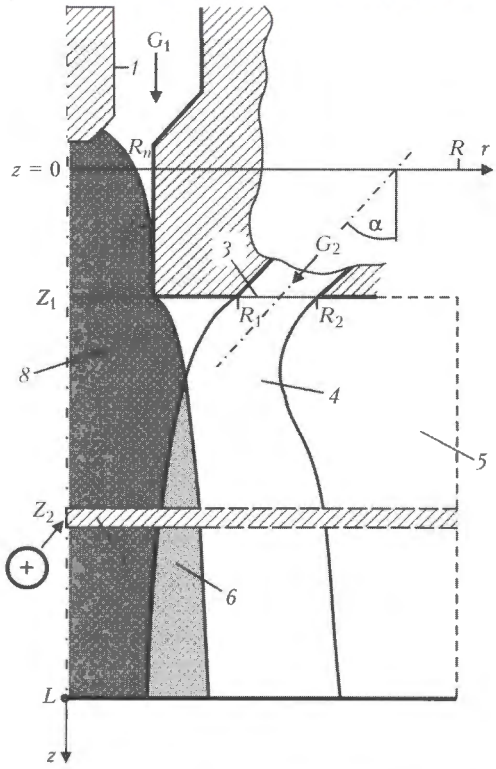

Figure 1. Schematic of plasmatron with anode wire: *1* – cathode; *2* – nozzle; *3* – blowing gas feed channel; *4* – blowing gas; *5* – external gas environment; *6* – mixing region; *7* – anode wire; *8* – arc plasma; see the rest of the designations in the text

$$D_{1,2}=2.66\cdot10^{-2}\frac{\sqrt{T^3(M_1+M_2)/(2M_1M_2)}}{p\sigma_{1,2}^2\Omega^{(1,1)}(T^*_{1,2})}, \tag{4}$$

where M_1 and M_2 are the molecular weights of the plasma and ambient gas, respectively; p is the pressure; $\sigma_{1,2}$ is the effective section of collisions of particles in the model of solid spheres for gas components of the mixture; $\Omega^{(1,1)}(T^*)$ is the function of reduced temperature $T^* = kT/\varepsilon_{1,2}$, the table of the values of which is given, e.g. in [7]; k is the Boltzmann constant; and $\varepsilon_{1,2}$ is the effective energy parameter of interaction of the particles that are the gas mixture components.

The system of MGD equations [1], as well as diffusion equation (1), should be supplemented with the relationships that determine dependence of thermodynamic characteristics, molecular transfer coefficients and optical properties of the two-component plasma upon the temperature, pressure and concentration of components. Detailed tables of temperature dependencies of these values for different gases are given, e.g. in [3, 8]. The following relationships can be used to determine the molecular coefficients of viscosity and thermal conductivity [7, 8]:

$$\eta_m=\sum_{j=1}^{2}x_j^2\times\left[x_j^2/\eta_j+1.385\sum_{k=1,\,k\neq j}^{2}x_jx_kRT/(PM_jD_{j,k})\right]^{-1}, \tag{5}$$

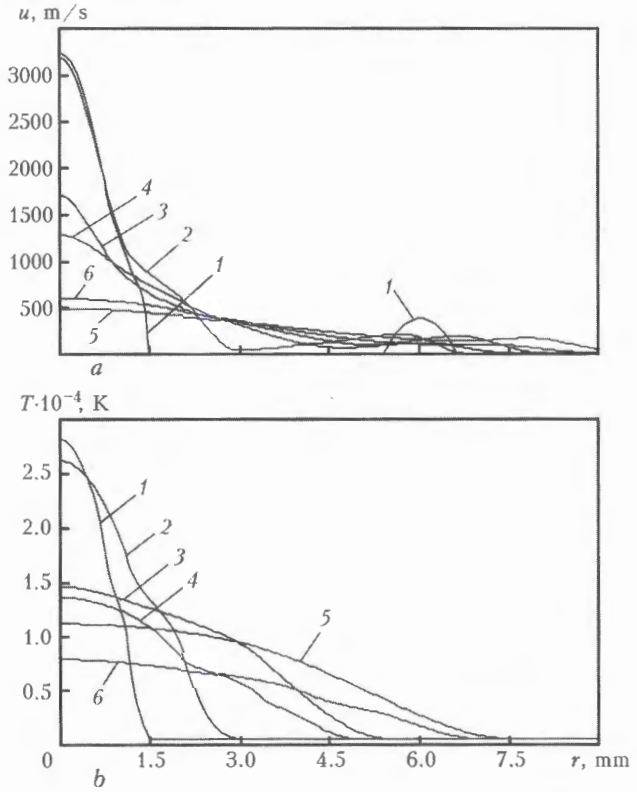

Figure 2. Radial distribution of velocity u (*a*) and temperature T (*b*) of the plasma blown about with annular flow of argon (*1, 2, 3, 5*) and air (*1, 2, 4, 6*) at $I = 200$ A, $G_1 = 1$ m^3/h, $G_2 = 20$ m^3/h: *1* — $z = 3$ (plasmatron nozzle exit section); *2* — 9.3 (anode wire region); *3, 4* = 50; *5, 6* — 150 mm

$$\chi_m = \left(\sum_{j=1}^{2} \chi_j x_j + \left[\sum_{j=1}^{2} x_j / \chi_j \right]^{-1} \right) / 2, \qquad (6)$$

where η_m and η_j are the coefficients of viscosity, respectively, of the mixture and j-th component ($j = 1, 2$); χ_m and χ_j are the coefficients of thermal conductivity, respectively, of the mixture and j-th component; and x_j is the volume concentration of the j-th component determined by the following relationship

$$x_j = \frac{m_j / M_j}{\sum_{k=1}^{2} m_k / M_k}.$$

The rest of the plasma properties in mixing were approximately calculated as follows:

$$\Gamma(T) = m_1 \Gamma_1(T) + m_2 \Gamma_2(T), \qquad (7)$$

where $\Gamma = \{\rho, C_p, \sigma, \psi\}$ are, respectively, the mass density, specific heat at constant pressure, specific electrical conductivity and volume power density of natural radiation.

Consider the statement of boundary conditions for convective diffusion equation (1). The symmetry condition is used at axis ($r = 0$):

$$\partial m_1 / \partial r = 0. \qquad (8)$$

Assuming that only the plasma gas can be inside the plasmatron nozzle, the following initial condition is set for the inlet section ($z = 0$ and $0 \le r \le R_n$):

$$m_1(r, 0) = 1, \qquad (9)$$

and the following condition is set for the plasmatron nozzle walls (at $r = R_n$ and $0 \le z < Z_1$):

$$m_1 = 1. \qquad (10)$$

For external boundaries of the exposed part of the calculation region, i.e. at $r = R$ and $z > Z_1$, it is assumed that

$$m_1 = 0. \qquad (11)$$

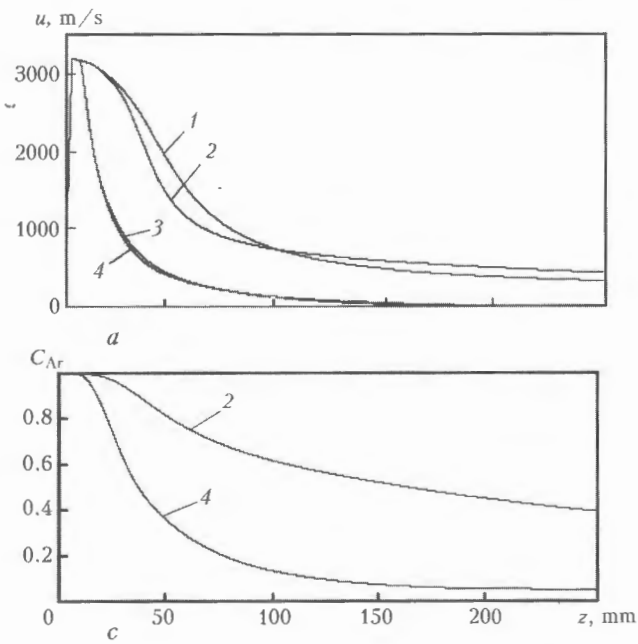

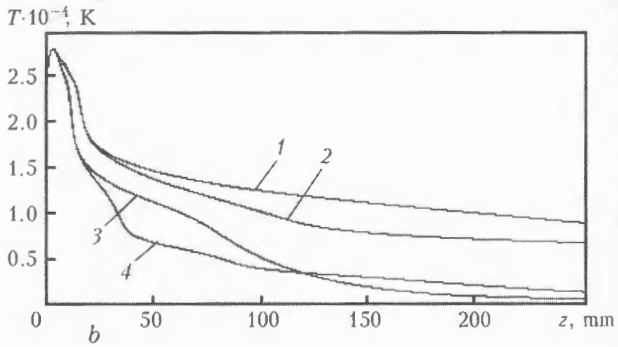

Figure 3. Longitudinal variations of velocity u (*a*), temperature T (*b*) of the plasma and relative concentration of argon x_{Ar} (*c*) in the plasma jet flowing into the argon (*1, 3*) and air (*2, 4*) environments at different working parameters of the plasmatron ($I = 200$ A, $G_1 = 1$ m^3/h): *1, 2* — $G_2 = 20$ m^3/h for argon and air, respectively; *3, 4* — $G_2 = 0$

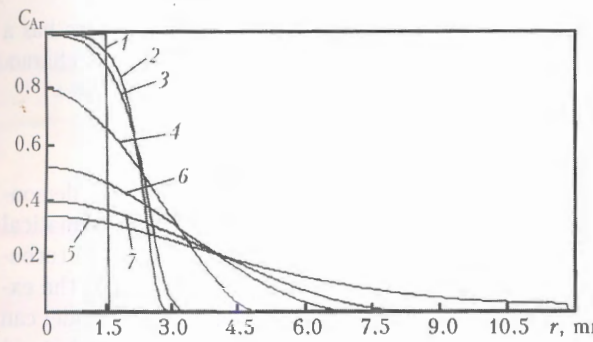

Figure 4. Profiles of relative concentration of argon in the plasma jet blown about with the annular air flow (*1, 2, 4, 6, 7*) and flowing into the quiescent gas environment (*1, 3, 5*) (I = 200 A, G_1 = = 1 m^3/h, G_2 = 20 m^3/h): *1* — z = 3 (plasmatron nozzle exit section); *2, 3* — 9.3 (anode wire region); *4, 5* — 50; *6* — 150; *7* — 250 mm

The system of MGD equations for the turbulent boundary layer [1], together with convective diffusion equation (1), relationships (2) through (7), and corresponding boundary conditions (8) through (11), makes it possible to determine gas-dynamic and thermal characteristics of the plasma jet, allowing for variations in properties of the plasma when the plasma gas is mixed with the external gas environment. In analogy with the equations of motion and energy, equation (1) was solved by the finite difference method using the main difference scheme for integration of the boundary layer equations [9].

Mathematical modelling of the effect of the type of ambient gas on the arc plasma flow formed by plasmatron with an anode wire was carried out for actual conditions of the plasma arc spraying process, where argon was used as the plasma gas, and air — as the external gas environment and blowing gas (argon was used for comparison). The following geometrical parameters of the calculation region were chosen (see Figure 1): radius and length of the plasma-shaping channel were 1.5 and 3.0 mm, respectively; anode wire was located at $z = Z_2$ = 9.3 mm; annular channel for feeding the blowing gas had an internal radius of 4.78 mm and external radius of 7.22 mm in the outlet section ($z = Z_1$ = 3 mm), and was inclined to the plasmatron axis at an angle of 37.5°; length L of the external part of the calculation region was 250 mm, and its radius was R = 12 mm. Temperature of the cold walls of the channels and ambient gas was assumed to be equal to 300 K. Working parameters of the plasmatron were as follows: arc current I = 200 A, plasma gas flow rate G_1 = 1 m^3/h, and blowing gas flow rate G_2 = 20 m^3/h.

Results of numerical modelling of characteristics of the argon plasma flowing into the air and argon environments both in the presence of the blowing gas flow and for the corresponding submerged jet are shown in Figures 2–7. In particular, Figures 2–4 show radial profiles and longitudinal distributions of axial components of the velocity and temperature of the plasma flowing into each of the environments considered, as well as corresponding distribution of the concentration of argon in the plasma jet emitted into air.

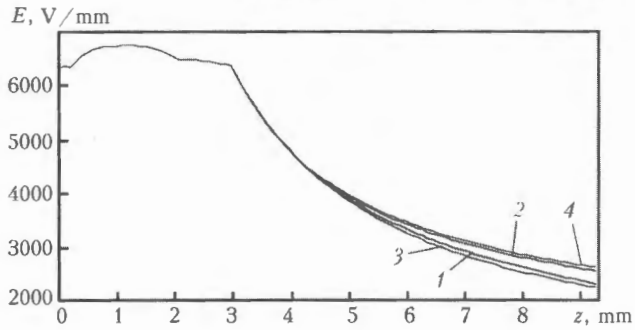

Figure 5. Longitudinal variations in intensity E of the electric field in the arc region of the flow at different working parameters of the plasmatron: *1–4* — same as in Figure 3

As follows form these Figures, the submerged jet emitted into any of the above gases expands very rapidly, and intensively gets mixed up with the external gas environment. As described in [1], blowing of the plasma jet with the annular laminar flow of cold gas of the same composition as the plasma gas hampers expansion of the plasma jet. Turbulence is partly suppressed by the annular gas flow surrounding the jet, while energy and impulse of the jet persist at larger distances, compared with the submerged jet.

The similar result was obtained with blowing of the argon plasma jet with the concurrent air flow (see Figures 2 and 3). As follows from these Figures, the type of the ambient gas does not have a substantial effect on the flow rate. Temperature in initial sections of the exposed region of the flow does not substantially change either. Further on, however, at a distance of about 25–30 mm from the nozzle exit section, as a result of mixing of gases the argon plasma jet blown about with air begins cooling down more intensively than the jet blown about with argon. In this case, the exposed region of the arc column gets more contracted, and the intensity of the electric field in an external region of the arc discharge grows to some extent (see Figure 5).

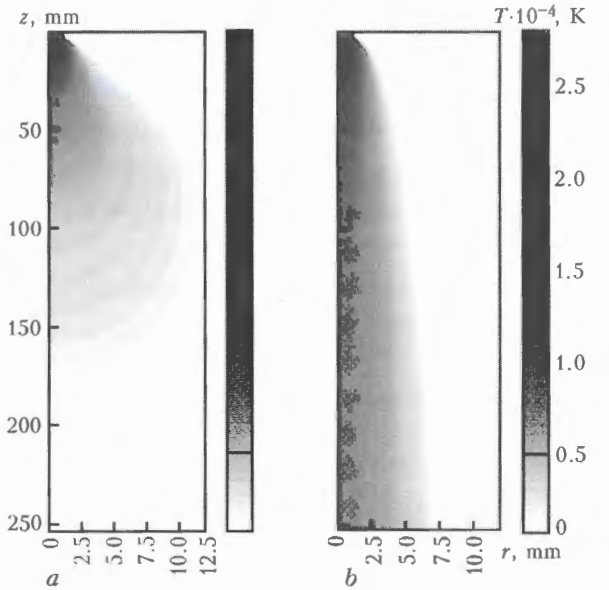

Figure 6. Distribution of temperature of the argon plasma jet flowing into the air environment without (*a*) and with (*b*) blowing

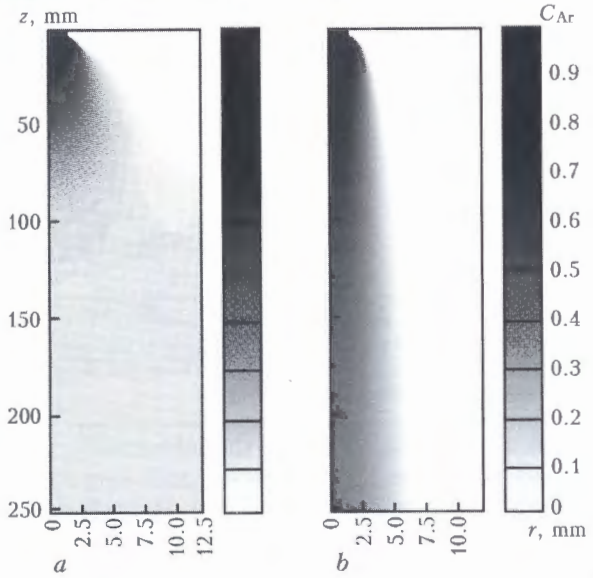

Figure 7. Distribution of relative concentration of argon in the plasma jet flowing into the air environment without (*a*) and with (*b*) blowing

Effect of the composition of the environment on thermal characteristics of the arc plasma flow is especially pronounced for the submerged jet flowing into the air environment. In this case, mixing of the argon plasma with air is intensified (see Figure 3, 4), and thermal conductivity of the mixture, because of high values of χ for air, increases, this leading to a more rapid decrease in the jet temperature.

The argon concentration fields and plasma temperatures corresponding to a flow into the air environment, for the turbulent plasma jet blown about with a laminar flow, and for the submerged plasma jet, are shown in Figure 6 and 7. As follows from the modelling results presented in the above Figures, blowing of the jet with the concurrent air flow causes restructuring of the flows. In particular, this results in formation of a high-temperature arc trace, where the concentration of argon persists at a sufficiently high level. For example, at a distance of about 50 mm from the nozzle exit section the concentration of argon in the plasma mixture is over 0.8 %, while at a distance of 100 mm it is 0.6 % (see Figure 3, *c*, and Figure 7). Cross section of the blown jet grows insignificantly with increase in the distance, and the jet core has a sufficiently uniform distribution of plasma characteristics.

CONCLUSIONS

1. The conducted numerical investigations demonstrate wide possibilities of the suggested mathematical model for calculation of characteristics of the turbulent flow of the arc plasma interacting with the external gas environment. This mathematical model can be generalised for a case of complex multi-component interaction of different gases and their mixtures, including in the presence of chemical reactions between components.

2. The submerged turbulent jet of the argon plasma flowing into the air environment very rapidly gets mixed up with air. Because of its unlimited expansion and increase in thermal conductivity of the formed plasma mixture, it cools down more intensively than the same jet flowing into quiescent argon.

3. Blowing of the turbulent jet of the argon plasma with the annular laminar flow of cold gas leads to formation of a very narrow and relatively high-temperature core of the flow, the concentration of argon in which remains high at substantial distances (about 0.5 % at a distance of 150 mm from the nozzle exit section).

1. Kharlamov, M.Yu., Krivtsun, I.V., Korzhik, V.N. et al. (2007) Mathematical model of arc plasma generated by plasmatron with anode wire. *The Paton Welding J.*, **12**, 9–14.
2. Favalli, R.C., Szente, R.N. (1998) Physical and mathematical modeling of non transferred plasma torches. *Brazilian J. of Physics*, **1**, March, 25–34.
3. Engelsht, V.S., Asanov, D.S., Gurovich, V.Ts et al. (1983) *Mathematical modelling of electric arc*. Frunze: Ilim.
4. (1990) *Theory of electric arc column*. Ed. by M.F. Zhukov. Novosibirsk: Nauka.
5. Lojtsyansky, L.G. (1973) *Mechanics of fluids and gases*. Moscow: Nauka.
6. Borisov, Yu.S., Krivtsun, I.V., Muzhichenko, A.F. et al. (2000) Computer modeling of the plasma spraying process. *The Paton Welding J.*, **12**, 40–50.
7. Arefiev, K.M. (1983) *Phenomena of transport in gas and plasma*. Leningrad: Energoatomizdat.
8. Boulos, M.I., Fauchais, P., Pfender, E. (1994) *Thermal plasmas: Fundamentals and applications*. Vol. 1. New York; London: Plenum Press.
9. Paskonov, V.M., Polezhaev, V.I., Chudov, L.A. (1984) *Numerical modelling of heat- and mass exchange processes*. Moscow: Nauka.

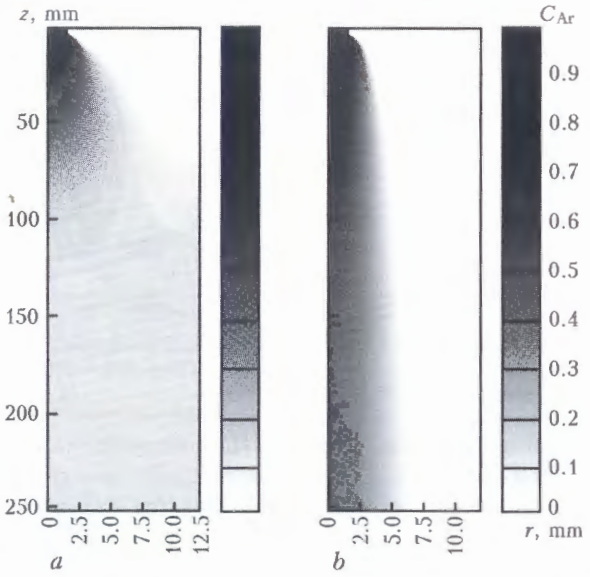

Figure 7. Distribution of relative concentration of argon in the plasma jet flowing into the air environment without (*a*) and with (*b*) blowing

Effect of the composition of the environment on thermal characteristics of the arc plasma flow is especially pronounced for the submerged jet flowing into the air environment. In this case, mixing of the argon plasma with air is intensified (see Figure 3, 4), and thermal conductivity of the mixture, because of high values of χ for air, increases, this leading to a more rapid decrease in the jet temperature.

The argon concentration fields and plasma temperatures corresponding to a flow into the air environment, for the turbulent plasma jet blown about with a laminar flow, and for the submerged plasma jet, are shown in Figure 6 and 7. As follows from the modelling results presented in the above Figures, blowing of the jet with the concurrent air flow causes restructuring of the flows. In particular, this results in formation of a high-temperature arc trace, where the concentration of argon persists at a sufficiently high level. For example, at a distance of about 50 mm from the nozzle exit section the concentration of argon in the plasma mixture is over 0.8 %, while at a distance of 100 mm it is 0.6 % (see Figure 3, *c*, and Figure 7). Cross section of the blown jet grows insignificantly with increase in the distance, and the jet core has a sufficiently uniform distribution of plasma characteristics.

CONCLUSIONS

1. The conducted numerical investigations demonstrate wide possibilities of the suggested mathematical model for calculation of characteristics of the turbulent flow of the arc plasma interacting with the external gas environment. This mathematical model can be generalised for a case of complex multi-component interaction of different gases and their mixtures, including in the presence of chemical reactions between components.

2. The submerged turbulent jet of the argon plasma flowing into the air environment very rapidly gets mixed up with air. Because of its unlimited expansion and increase in thermal conductivity of the formed plasma mixture, it cools down more intensively than the same jet flowing into quiescent argon.

3. Blowing of the turbulent jet of the argon plasma with the annular laminar flow of cold gas leads to formation of a very narrow and relatively high-temperature core of the flow, the concentration of argon in which remains high at substantial distances (about 0.5 % at a distance of 150 mm from the nozzle exit section).

1. Kharlamov, M.Yu., Krivtsun, I.V., Korzhik, V.N. et al. (2007) Mathematical model of arc plasma generated by plasmatron with anode wire. *The Paton Welding J.*, **12**, 9–14.
2. Favalli, R.C., Szente, R.N. (1998) Physical and mathematical modeling of non transferred plasma torches. *Brazilian J. of Physics*, **1**, March, 25–34.
3. Engelsht, V.S., Asanov, D.S., Gurovich, V.Ts et al. (1983) *Mathematical modelling of electric arc*. Frunze: Ilim.
4. (1990) *Theory of electric arc column*. Ed. by M.F. Zhukov. Novosibirsk: Nauka.
5. Lojtsyansky, L.G. (1973) *Mechanics of fluids and gases*. Moscow: Nauka.
6. Borisov, Yu.S., Krivtsun, I.V., Muzhichenko, A.F. et al. (2000) Computer modeling of the plasma spraying process. *The Paton Welding J.*, **12**, 40–50.
7. Arefiev, K.M. (1983) *Phenomena of transport in gas and plasma*. Leningrad: Energoatomizdat.
8. Boulos, M.I., Fauchais, P., Pfender, E. (1994) *Thermal plasmas: Fundamentals and applications*. Vol. 1. New York; London: Plenum Press.
9. Paskonov, V.M., Polezhaev, V.I., Chudov, L.A. (1984) *Numerical modelling of heat- and mass exchange processes*. Moscow: Nauka.

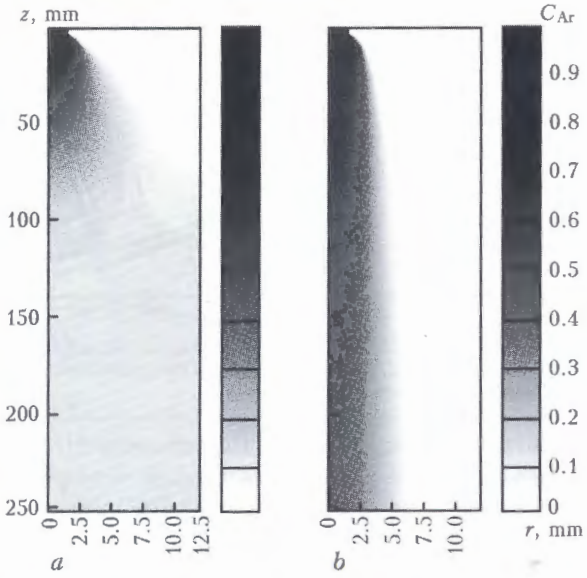

Figure 7. Distribution of relative concentration of argon in the plasma jet flowing into the air environment without (*a*) and with (*b*) blowing

Effect of the composition of the environment on thermal characteristics of the arc plasma flow is especially pronounced for the submerged jet flowing into the air environment. In this case, mixing of the argon plasma with air is intensified (see Figure 3, 4), and thermal conductivity of the mixture, because of high values of χ for air, increases, this leading to a more rapid decrease in the jet temperature.

The argon concentration fields and plasma temperatures corresponding to a flow into the air environment, for the turbulent plasma jet blown about with a laminar flow, and for the submerged plasma jet, are shown in Figure 6 and 7. As follows from the modelling results presented in the above Figures, blowing of the jet with the concurrent air flow causes restructuring of the flows. In particular, this results in formation of a high-temperature arc trace, where the concentration of argon persists at a sufficiently high level. For example, at a distance of about 50 mm from the nozzle exit section the concentration of argon in the plasma mixture is over 0.8 %, while at a distance of 100 mm it is 0.6 % (see Figure 3, *c*, and Figure 7). Cross section of the blown jet grows insignificantly with increase in the distance, and the jet core has a sufficiently uniform distribution of plasma characteristics.

CONCLUSIONS

1. The conducted numerical investigations demonstrate wide possibilities of the suggested mathematical model for calculation of characteristics of the turbulent flow of the arc plasma interacting with the external gas environment. This mathematical model can be generalised for a case of complex multi-component interaction of different gases and their mixtures, including in the presence of chemical reactions between components.

2. The submerged turbulent jet of the argon plasma flowing into the air environment very rapidly gets mixed up with air. Because of its unlimited expansion and increase in thermal conductivity of the formed plasma mixture, it cools down more intensively than the same jet flowing into quiescent argon.

3. Blowing of the turbulent jet of the argon plasma with the annular laminar flow of cold gas leads to formation of a very narrow and relatively high-temperature core of the flow, the concentration of argon in which remains high at substantial distances (about 0.5 % at a distance of 150 mm from the nozzle exit section).

1. Kharlamov, M.Yu., Krivtsun, I.V., Korzhik, V.N. et al. (2007) Mathematical model of arc plasma generated by plasmatron with anode wire. *The Paton Welding J.*, **12**, 9–14.
2. Favalli, R.C., Szente, R.N. (1998) Physical and mathematical modeling of non transferred plasma torches. *Brazilian J. of Physics*, **1**, March, 25–34.
3. Engelsht, V.S., Asanov, D.S., Gurovich, V.Ts et al. (1983) *Mathematical modelling of electric arc*. Frunze: Ilim.
4. (1990) *Theory of electric arc column*. Ed. by M.F. Zhukov. Novosibirsk: Nauka.
5. Lojtsyansky, L.G. (1973) *Mechanics of fluids and gases*. Moscow: Nauka.
6. Borisov, Yu.S., Krivtsun, I.V., Muzhichenko, A.F. et al. (2000) Computer modeling of the plasma spraying process. *The Paton Welding J.*, **12**, 40–50.
7. Arefiev, K.M. (1983) *Phenomena of transport in gas and plasma*. Leningrad: Energoatomizdat.
8. Boulos, M.I., Fauchais, P., Pfender, E. (1994) *Thermal plasmas: Fundamentals and applications*. Vol. 1. New York; London: Plenum Press.
9. Paskonov, V.M., Polezhaev, V.I., Chudov, L.A. (1984) *Numerical modelling of heat- and mass exchange processes*. Moscow: Nauka.

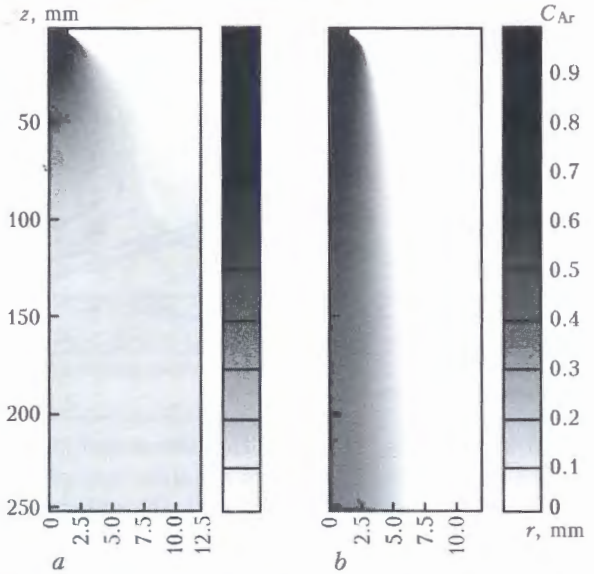

Figure 7. Distribution of relative concentration of argon in the plasma jet flowing into the air environment without (*a*) and with (*b*) blowing

Effect of the composition of the environment on thermal characteristics of the arc plasma flow is especially pronounced for the submerged jet flowing into the air environment. In this case, mixing of the argon plasma with air is intensified (see Figure 3, 4), and thermal conductivity of the mixture, because of high values of χ for air, increases, this leading to a more rapid decrease in the jet temperature.

The argon concentration fields and plasma temperatures corresponding to a flow into the air environment, for the turbulent plasma jet blown about with a laminar flow, and for the submerged plasma jet, are shown in Figure 6 and 7. As follows from the modelling results presented in the above Figures, blowing of the jet with the concurrent air flow causes restructuring of the flows. In particular, this results in formation of a high-temperature arc trace, where the concentration of argon persists at a sufficiently high level. For example, at a distance of about 50 mm from the nozzle exit section the concentration of argon in the plasma mixture is over 0.8 %, while at a distance of 100 mm it is 0.6 % (see Figure 3, *c*, and Figure 7). Cross section of the blown jet grows insignificantly with increase in the distance, and the jet core has a sufficiently uniform distribution of plasma characteristics.

CONCLUSIONS

1. The conducted numerical investigations demonstrate wide possibilities of the suggested mathematical model for calculation of characteristics of the turbulent flow of the arc plasma interacting with the external gas environment. This mathematical model can be generalised for a case of complex multi-component interaction of different gases and their mixtures, including in the presence of chemical reactions between components.

2. The submerged turbulent jet of the argon plasma flowing into the air environment very rapidly gets mixed up with air. Because of its unlimited expansion and increase in thermal conductivity of the formed plasma mixture, it cools down more intensively than the same jet flowing into quiescent argon.

3. Blowing of the turbulent jet of the argon plasma with the annular laminar flow of cold gas leads to formation of a very narrow and relatively high-temperature core of the flow, the concentration of argon in which remains high at substantial distances (about 0.5 % at a distance of 150 mm from the nozzle exit section).

1. Kharlamov, M.Yu., Krivtsun, I.V., Korzhik, V.N. et al. (2007) Mathematical model of arc plasma generated by plasmatron with anode wire. *The Paton Welding J.*, **12**, 9–14.
2. Favalli, R.C., Szente, R.N. (1998) Physical and mathematical modeling of non transferred plasma torches. *Brazilian J. of Physics*, **1**, March, 25–34.
3. Engelsht, V.S., Asanov, D.S., Gurovich, V.Ts et al. (1983) *Mathematical modelling of electric arc*. Frunze: Ilim.
4. (1990) *Theory of electric arc column*. Ed. by M.F. Zhukov. Novosibirsk: Nauka.
5. Lojtsyansky, L.G. (1973) *Mechanics of fluids and gases*. Moscow: Nauka.
6. Borisov, Yu.S., Krivtsun, I.V., Muzhichenko, A.F. et al. (2000) Computer modeling of the plasma spraying process. *The Paton Welding J.*, **12**, 40–50.
7. Arefiev, K.M. (1983) *Phenomena of transport in gas and plasma*. Leningrad: Energoatomizdat.
8. Boulos, M.I., Fauchais, P., Pfender, E. (1994) *Thermal plasmas: Fundamentals and applications*. Vol. 1. New York; London: Plenum Press.
9. Paskonov, V.M., Polezhaev, V.I., Chudov, L.A. (1984) *Numerical modelling of heat- and mass exchange processes*. Moscow: Nauka.

MODELING OF RESIDUAL STRESSES IN LASER WELDING

A. BOKOTA and W. PIEKARSKA
Politechnika Czestochowska, Czestochowa, Poland

Mathematical model and calculation of strains and stresses, occurring in laser welding of a steel sheet, are presented. For determination of the temperature field equation of heat conductivity with a convective term is used, solved by the method of Green function. Model of phase transformations is based on the diagram of continuous cooling of welded steel in Avrami, Koistinen and Marburger equations. When determining temporal and residual stresses depending upon a heat load and phase transformations, connection of thermophysical parameters with temperature and phase composition of steel is taken into account. In the model of stresses structural and transformation strains are taken into account.

Keywords: *laser welding, steel, welded joints, model, numeric investigation, phase composition, structural and transformation strain, stressed state*

In consideration of the laser welding process comprehensive descriptions and models that would make it possible to estimate phenomena which accompany this process are usually absent. The reasons of occurrence of specific processes that are not characteristic of other methods of welding are high speed and specific shape of a weld, because laser beam is characterized by high concentration of energy. Metal in a welding zone is heated up to a high temperature at significant gradient of the latter [1–3]. As a result, a significant thermal strain and strain stipulated by transformations, occur and due to this — formation of temporal and residual stresses [4–9].

In majority of works, mainly experimental ones, influence of welding parameters on characteristics of welded joints are considered, and existing digital models relate to determination of the temperature field, fusion zone and HAZ. In [4, 6, 7] the model of mechanical phenomena in laser welding is proposed, but without taking into account transformation strain.

Of special significance from technological viewpoint is assessment of influence of structural transformations on strain and level of stresses in the welding zone. Occurring stresses form mechanical characteristics and strength of a welded joint. Such assessment is possible if information is available about value and form of phase transformations, occurring in a certain thermal cycle.

In the work for calculation of a specific phase composition in solid state and accompanying isotropic thermal and structural strains the model of phase transformation for welded low-alloy steel was used [8, 10]. It is assumed that the material being welded is elasto-plastic. Values of temporal and residual stresses, occurring due to heat loads and phase transformations, were obtained by solution of equilibrium equations by the method of finite elements using law of non-isothermal plastic flow with isotropic hardening and condition of Huber–Mises [11]. In the model dependence of thermophysical parameters upon temperature and phase composition of the metal are taken into account [5, 8, 12]. Calculation of phase transformations and stresses allows avoiding expensive experiments, carried out for getting data, necessary for optimal carrying out of the laser welding.

Calculation of the temperature field is carried out according to equation of unsteady heat flow with a convective term:

$$a\nabla^2 T(\mathbf{x}, t) - \frac{\partial T(\mathbf{x}, t)}{\partial t} + \nabla T(\mathbf{x}, t)\mathbf{v} = -\frac{Q}{C}, \qquad (1)$$

where a is the temperature equalization factor; C is the specific heat capacity; Q is the power of volumetric heat sources, in which heat from the laser beam is taken into account; $\mathbf{v}$ is the vector of the laser beam movement speed; $\mathbf{x} = \mathbf{x}(x_\alpha)$ is the vector of a considered point position.

Equation (1) is solved for a linear heat source with a certain immersion h_z by the method of Green function superposition, suggested in [3].

Temperature field in the considered point determines the heat source with distribution of power in the form

$$Q(\mathbf{x}') = \begin{cases} \tilde{Q}(1 - R)/(\pi r^2 h_z), & x' = 0,\ y' = 0,\ -h_z \le z' \le h_z, \\ 0, & |z'| > h_z, \end{cases} \qquad (2)$$

where h_z is the laser penetration depth, [m]; $\tilde{Q}$ is the laser beam power, W; R is the reflection factor; r is the laser beam radius, m.

It is assumed that stationary solution in the considered area exists for time t, and mobile system of coordinates $\{x', y', z'\}$ moves relative the base one at the speed $\mathbf{v} = \mathbf{v}(u, 0, 0)$.

Using Green function and adding temperature T_0 we obtain

$$T(\mathbf{x}, t) = \frac{1}{C}\int_0^t \int_\Omega Q(\mathbf{x}', t')\, G(|\mathbf{x} - (\mathbf{x}' - d)|, (t - t')\, d\Omega' dt' + T_0. \qquad (3)$$

Integrating expression (3) in regard to spatial coordinates and taking into account equation (2) we

obtain semi-analytical solution of equation (1); numeric integration (3) by time is carried out by Romberg method.

Phase transformations, thermal and structural strains. Specific volume of austenite, formed during heating, is determined according to Mekhl–Avrami formula [13–15]:

$$\tilde{\eta}_A(T, t) = 1 - \exp(-bt^n), \quad (4)$$

where $\tilde{\eta}_A$ is the weight share of austenite formed due to heating; t is the time of heating; $b = b(T)$ and $n = n(T)$ are the coefficients established according to conditions of beginning ($\eta_s = 0.01$) and end ($\eta_f = 0.99$) of the transformations [15].

Weight share of the phase, formed during cooling of austenite, is determined by temperature and rate of cooling within the temperature range $T_{8/5}$. Quantitatively weight share of the new phase (ferrite, pearlite, or bainite) is also determined taking into account rate of cooling $w_{8/5}$ according to Mekhl–Avrami formula (diffusion transformations) and already existing specific components:

$$\eta(\cdot)(T, t) = \eta^{*}(\cdot)\tilde{\eta}_A(1 - \exp(-b(t(T))^n)) + \eta^0(\cdot), \quad (5)$$

where $\eta^{*}(\cdot)$ is the maximal experimentally established weight share of the phase at a certain rate of cooling; $\tilde{\eta}_A$ is the weight share of austenite formed due to heating; $\eta^0(\cdot)$ is the amount of the initial structure phase without transition into austenite.

Weight share of martensite is determined according to the modified Koistinen–Marburger formula [10, 15, 16]:

$$\eta_M(T) = \eta^{*}(\cdot)\tilde{\eta}_A\left(1 - \exp\left(\left(-\frac{M_s - T}{M_s - M_f}\right)^m\right)\right), \quad T \in [M_s, M_f(w_{8/5})], \quad (6)$$

where m is the experimentally determined coefficient (for the tested steel $m = 2.5$); M_s and M_f are the temperatures of beginning and end of martensite transformation.

Increments of isotropic strains, depending upon temperature and phase transformations (structural strains), are determined according to formulas [8, 10]:

$$d\varepsilon^{TPh} = \sum_{i=1}^{i=5} \alpha_i \eta_i dT - \varepsilon_A^{Ph} d\eta_A,$$
$$d\varepsilon^{TPh} = \sum_{i=1}^{i=5} \alpha_i \eta_i dT + \sum_{j=1}^{j=5} \varepsilon_j^{Ph} d\eta_j, \quad (7)$$

where $\alpha_i = \alpha_i(T)$, i = A, B, F, M, P are the coefficients of linear dilatation of respectively austenite, bainite, ferrite, martensite and pearlite; ε_A^{Ph} is the isotropic strain of phase transformation of initial structure into austenite; j = B, F, M, P; $\varepsilon_j^{Ph} = \varepsilon_j^{Ph}(T)$ are the isotropic strains of austenite phase transformation respectively into ferrite, bainite, martensite and pearlite.

We assume values of coefficients of linear dilatation and changes of volume depending upon phase transformations according to experimental data, obtained on the installation with reproduction of thermal cycles at different rates of heating and cooling [10].

Stresses. Stresses in laser welding were calculated by solution of equilibrium equation, expressed in the rates:

$$\operatorname{div}(\dot{\sigma}(\mathbf{x}, t)) = 0, \quad \sigma^T = \sigma. \quad (8)$$

Formulas of Hook's law, expressed in the rates, have the form

$$\dot{\sigma} = \mathbf{E}\dot{\varepsilon}^e + \dot{\mathbf{E}}\varepsilon^e, \quad \varepsilon^e = \varepsilon - \varepsilon^p - \varepsilon^{TPh} - \varepsilon^{tp}, \quad (9)$$

where $\sigma = \sigma(\sigma_{\alpha\beta})$ is the stress tensor; E is the tensor of the material constants; ε^e, ε, ε^p are respectively the tensors of elastic, total and plastic strains; ε^{TPh} is the tensor of isotropic and thermal strains and strains, occurring due to phase transformations in a solid body ($\varepsilon^{TPh} = \varepsilon^T + \varepsilon^{Ph}$); ε^{tp} is the tensor of transformation strain.

Plastic strain is determined taking into account law of non-isothermal plastic flow [4, 11. 17]

$$\dot{\varepsilon}^p = \dot{\Lambda}\frac{\partial f}{\partial \sigma} = \dot{\Lambda}\frac{3S}{2Y}, \quad \dot{f} = 0, \quad f = 0, \quad (10)$$

where $\dot{\Lambda}$ is the scalar multiplier of plasticity; $f = f(\sigma, Y(T, \varepsilon^p)$ is the function of plastic flow that depends upon stress tensor and yield strength; S is the stress tensor deviator.

Value of plastic deformation is determined using the model of non-isothermal plastic flow with isotropic hardening and Huber–Mises conditions of plasticity, and function of the flow equals

$$f = \sigma_{ef} - Y(T, \sum \eta_k, \varepsilon_{ef}^p) = 0, \quad (11)$$

where σ_{ef} is the equivalent stress; ε_{ef}^p is the efficient plastic strain; $Y = Y(T, \Sigma\eta_k, \varepsilon_{ef}^p)$ is the yield strength of the material that depends upon phase composition $\Sigma\eta_k$ at temperature T and equivalent plastic deformation ε_{ef}^p;

$$Y(T, \sum \eta_k, \varepsilon_{ef}^p) = Y_0(T, \sum \eta_k) + Y_H(T, \sum \eta_k, \varepsilon_{ef}^p); \quad (12)$$

$Y_0 = Y_0(T, \Sigma\eta_k)$ is the yield strength of the material that depends upon temperature and phase composition when plastic strain is absent; $Y_H = Y_H(T, \Sigma\eta_k, \varepsilon_{ef}^p)$ is the yield strength increment due to hardening of the material.

Young's modulus and tangent modulus depend upon temperature, and yield strength — upon temperature and phase composition:

$$E = E(T), \quad E^t = E^t(T), \quad Y_0 = \sum_{i=1}^{5} Y_i(T)\eta_i. \quad (13)$$

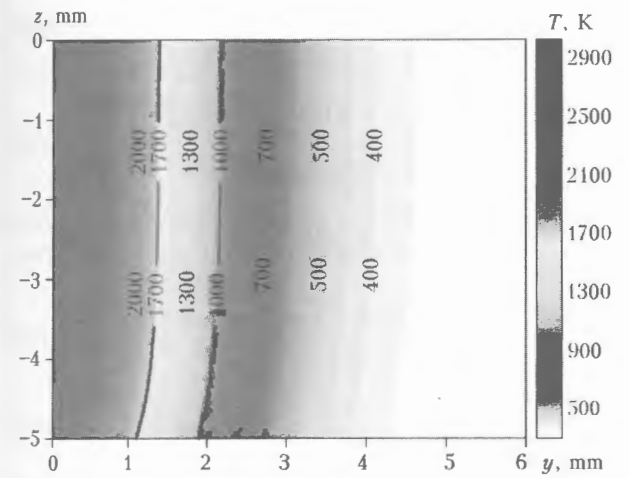

Figure 1. Distribution of temperature in cross section of specimen (maximal temperature zone)

Rate of the yield strength change is determined by the dependence

$$\dot{Y} = \kappa \dot{\varepsilon}^p + H_T^Y \dot{T} + \sum H_{\eta_k}^Y \dot{\eta}_k, \qquad (14)$$

where κ, H_T^Y, $H_{\eta_k}^Y$ are respectively the modules of hardening, thermal weakening and structural hardening-weakening [7, 8, 17].

It is evident that rate of equivalent plastic strain ($\dot{\varepsilon}_{ef}^p = \dot{\Lambda}$) depends upon increment of stresses above yield strength, gradients of thermophysical parameters and structural state of the material.

On basis of Leblond model [13, 18] we assume that transformation strain is

$$\dot{\varepsilon}^{tp} = \begin{cases} 0, & \eta_i \le 0.03, \\ -K_{1i} \dfrac{S}{Y(\eta_1)} \ln(\eta_i)\, \dot{\eta}_i; & \eta_i \ge 0.03, \end{cases} \qquad (15)$$

where $K_{1i} = 3\varepsilon_{1i}^{ph}$ are the volumetric structural strains of i-phase formation from initial phase «1»; $Y(\eta_1)$ is the yield strength for initial phase.

Equilibrium equation is supplemented by respective boundary and initial conditions:

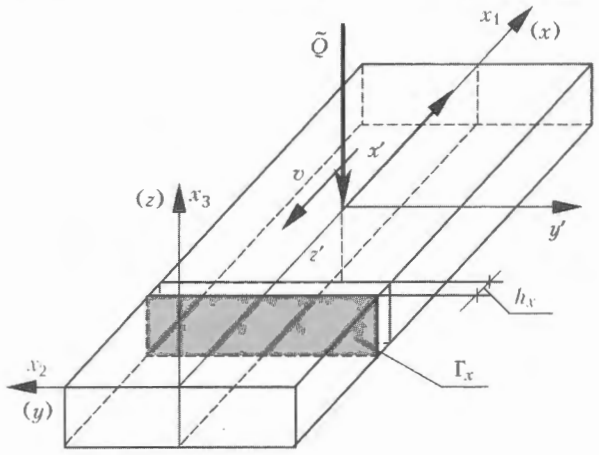

Figure 3. Scheme of laser-welded rectangular specimen

$$\sigma(\mathbf{x}, t_0) = \sigma(\mathbf{x}, T_{kr}) = 0, \quad \varepsilon(\mathbf{x}, t_0) = \varepsilon(\mathbf{x}, T_{kr}) = 0, \qquad (16)$$

where T_{kr} is the temperature assumed as initial in generation of stresses in the melting zone. The problem is solved by the method of finite elements, and in the process of iteration the modified algorithm of Newton–Rapson is used [11].

Example of calculations. Let us consider example of calculations of a temperature field, number of phases and stresses in a rectangular specimen of 100 × × 20 × 5 mm size, welded by laser welding.

In the calculations the following values were assumed: reflection factor $R = 0.25$, heat source power $Q = 3.8$ kW, and speed of movement of the beam of 2 mm diameter $v = 42$ m/h [1, 7]. Results of the calculations are presented in Figures 1 and 2.

Proceeding from considered geometry of the specimen (a prism), we use for solution of stresses and strains modified conditions of a plane strain, when conditions of equality to zero of total normal force $N\big|_{\Gamma_x}$ are fulfilled in cross section Γ_x of the specimen (Figure 3). The calculations allowed determining mean values of strain, which meet the condition [8]:

$$\int_{\Gamma_x} \dot{\sigma}_x d\Gamma = \dot{N}\big|_{\Gamma_x} = 0, \quad \int_{\Gamma_x} \sigma_x d\Gamma = N\big|_{\Gamma_x} = 0. \qquad (17)$$

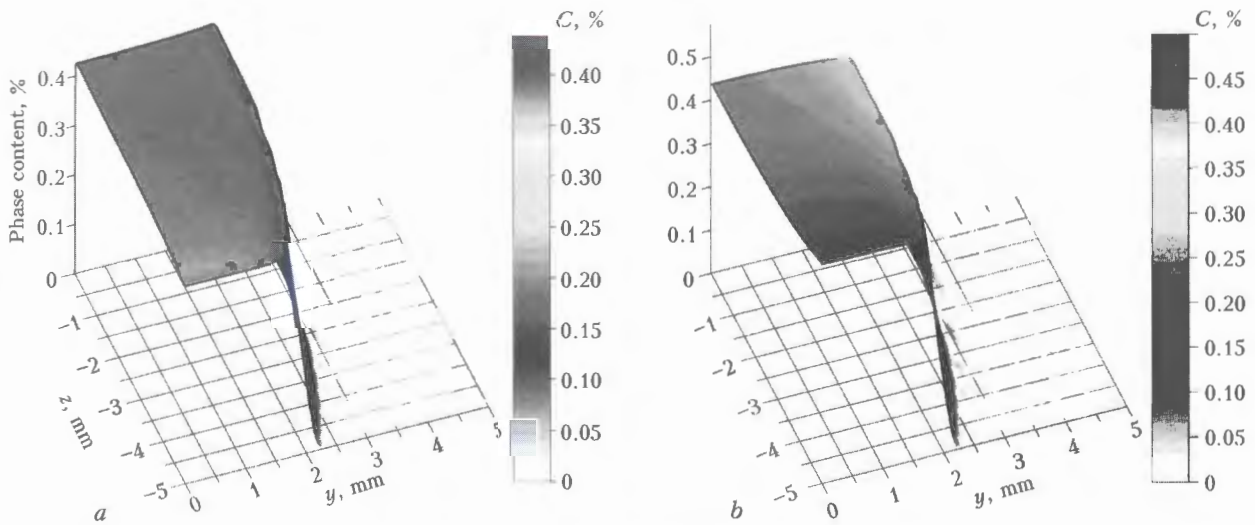

Figure 2. Distribution of bainite (*a*) and martensite (*b*) in HAZ metal after welding

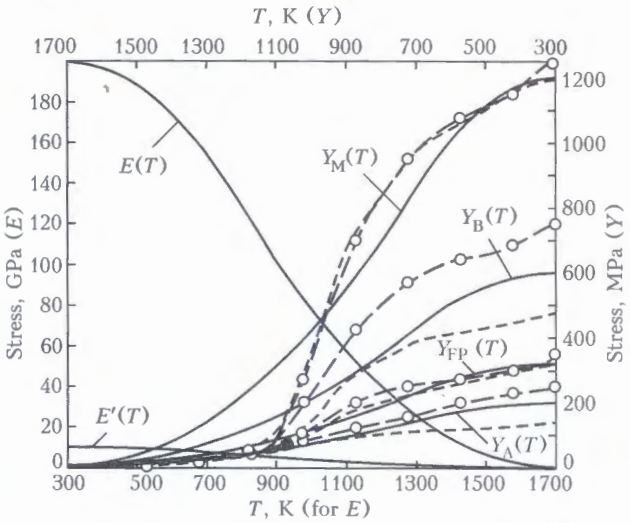

Figure 4. Dependence of Young's modulus, tangent modulus and yield strength upon temperature according to [5] (dash line) and [12] (dash-dotted line); solid curves — calculation

Using formulas of Hook's law for longitudinal stress ($\dot{\sigma}_{11} = \dot{\sigma}_x$)

$$\dot{\sigma}_{11} = \dot{\sigma}_x = (2\mu + \lambda)\dot{\varepsilon}^e_x + \lambda\,\dot{\varepsilon}^e_{\gamma\gamma} + \\ + (2\dot{\mu} + \dot{\lambda})\varepsilon^e_{11} + \dot{\lambda}\,\dot{\varepsilon}^e_{\gamma\gamma}\mu, \quad \gamma = 2.3 \tag{18}$$

and dependences (17), we obtain following equation for determining rate of mean total longitudinal strain:

$$\dot{\varepsilon}_{11} = \dot{\varepsilon}_x = \\ = \frac{\dot{N}\big|_{\Gamma_x} - \int\limits_{\Gamma_x} \lambda\dot{\varepsilon}^e_{rr}d\Gamma - \int\limits_{\Gamma_x}((2\dot{\mu} + \dot{\lambda})\varepsilon^e_{11} + \dot{\lambda}\,\varepsilon^e_{rr})d\Gamma + \int\limits_{\Gamma_x}(2\mu + \lambda)(\dot{\varepsilon}^p_{11} + \dot{\varepsilon}^T_{11}{}^{ph} + \dot{\varepsilon}^{pp}_{11}))d\Gamma}{\int\limits_{\Gamma_x}(2\mu + \lambda)d\Gamma}, \tag{19}$$

where $\lambda = \lambda(E, \nu)$, $\mu = \mu(E, \nu)$ are the Lame constants; ν is the Poisson's ratio [11].

Application of modified model of the plane strain acquires total normal force equal to zero in any cross section of the rectangle.

We assume for low-carbon low-alloy steel (S355J2G3) the following thermophysical parame-

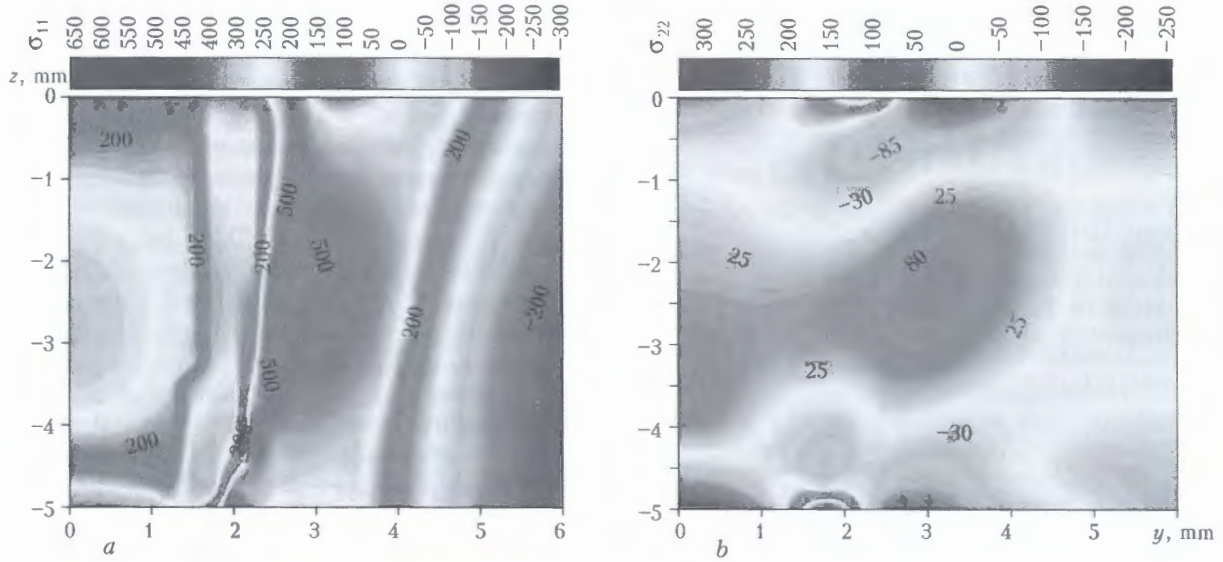

Figure 5. Distribution of axial σ_{11} (*a*) and normal σ_{22} (*b*) residual stresses in cross section of specimen

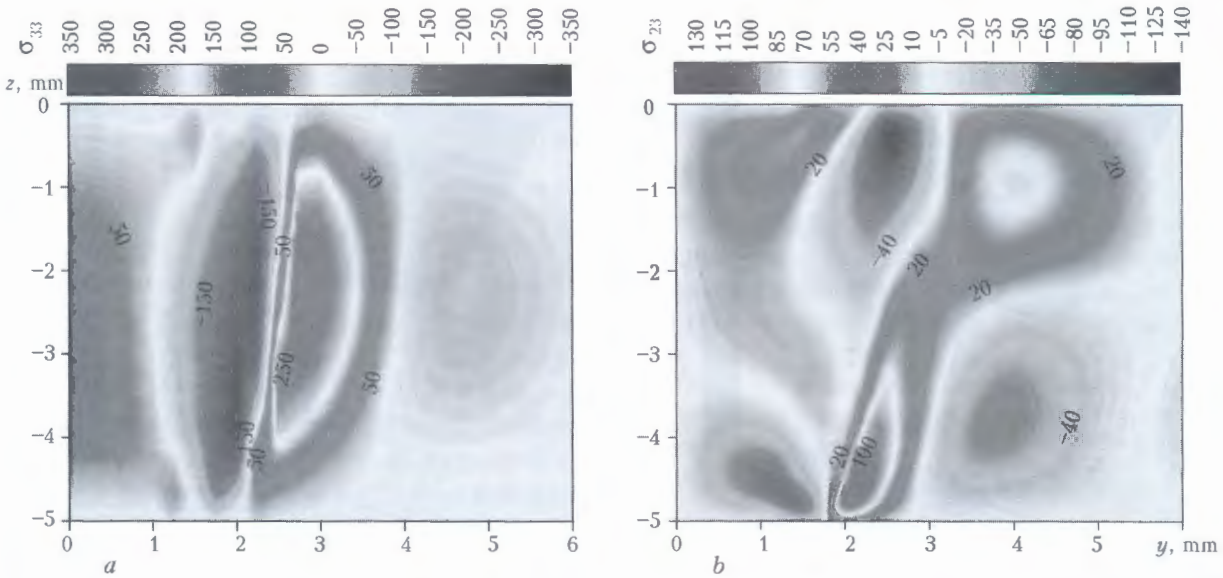

Figure 6. Distribution of normal σ_{33} (*a*) and tangent σ_{23} (*b*) residual stresses in cross section of specimen

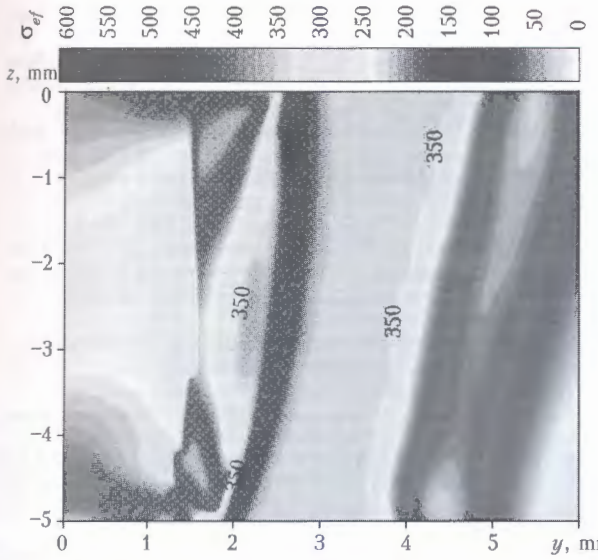

Figure 7. Residual efficient stresses σ_{ef} in cross section of specimen

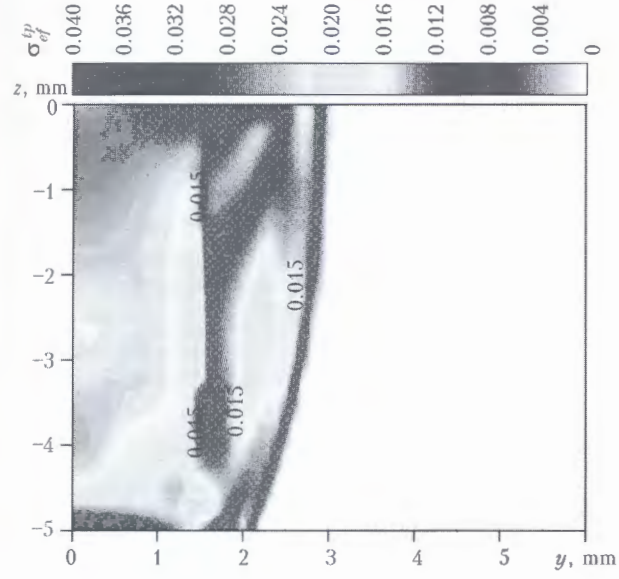

Figure 8. Efficient transformation strain σ_{ef}^{tp} in cross section of specimen

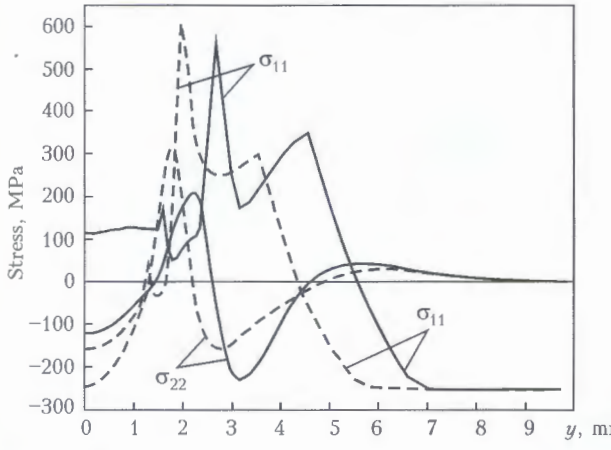

Figure 9. Distribution of residual stresses in near-surface layers of upper (solid curve) and lower (dash curve) surfaces of specimen

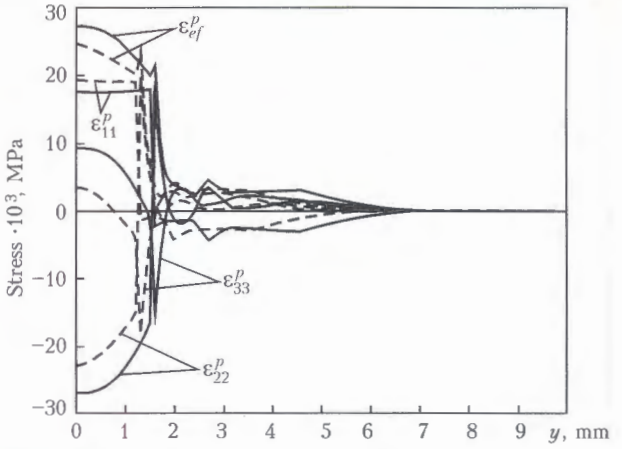

Figure 10. Distribution of plastic strain in layer of central part of specimen ($z = -2.5$)

ters: $T_0 = 300$ K, $T_{sol} = 1650$ K, $T_{liq} = 1750$ K, $T_{cr} = 0.5(T_{liq} + T_{sol})$, $E(T_0) = 2.0 \cdot 10^5$, $E(T_{cr}) = 10$ MPa, $E^t(T) = 0.05E(T)$. Yield strengths of formed structures $Y_0(T_0, \eta_k)$ (austenite, bainite, ferrite, martensite and pearlite) have values 200, 600, 320, 1200 and 320 MPa respectively [2, 4, 5], and for $T = T_{cr}$ yield strength $Y_0(T_{cr}, \eta_k) = 5$ MPa. Within temperature range T_0–T_{cr} values of thermophysical parameters are approximated by parabolic functions (Figure 4).

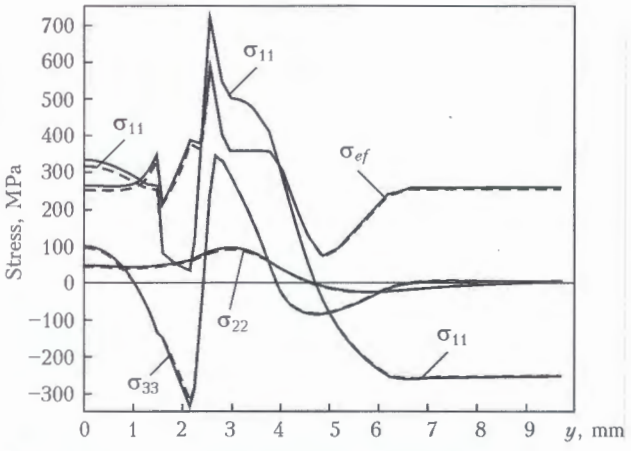

Figure 11. Distribution of residual stresses in layer of central part of specimen ($z = -2.5$) taking (dash curve) and without taking into account (solid curve) transformation strains

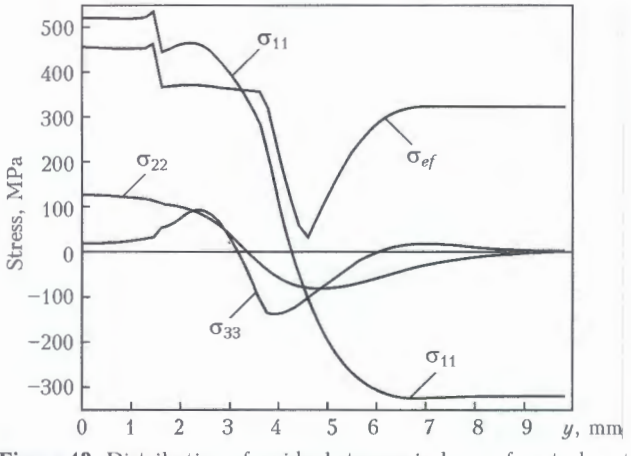

Figure 12. Distribution of residual stresses in layer of central part of specimen ($z = -2.5$) without taking into account phase strains ($\varepsilon^{Ph} = 0$)

Results of calculation of distribution of residual stresses and plastic strain in the HAZ metal and the near-weld zone are presented in Figures 5–10.

Distribution of stresses in the HAZ metal of a welded joint, produced by laser welding (Figures 5–7, 9 and 11) is not favorable from the operation viewpoint. This relates both to axial (σ_{11}, Figure 5, *a* and Figure 9) and normal stresses in perpendicular to the axis direction (σ_{22}, Figure 5, *b*). These stresses are sufficiently high tensile stresses and, in addition, stresses σ_{22} act in the near-surface layers of the metal (Figure 5, *b* and Figure 9). Level of stresses is significantly affected by structural strain, in absence of which the results will be different (Figure 12). Transformation strain affects level of stresses to a smaller degree (Figure 11), which allows taking it not into account in modeling of stressed state of a welded joint at assumed parameters of welding.

1. Khaskin, V.Yu., Pavlovsky, S.Yu., Tarashchuk, V.P. et al. (2001) Peculiarities of welding thin-sheet low-carbon steels using a pulsed-periodic radiation of CO_2-laser. *The Paton Welding J.*, **2**, 42–46.
2. Kyrsanidi, An.K., Kermanidis, Th.B., Pantelakis, Sp.G. (1999) Numerical and experimental investigation of the laser forming process. *J. Materials Proc. Technol.*, **87**, 281–290.
3. Liu, Y.-N., Kannatey-Asibu, E. (1993) Laser beam welding with simultaneous Gaussian laser preheating. *J. of Heat Transfer, Transact. of ASME*, **115**, 34–41.
4. Karlsson, L. (1986) *Thermal stresses in welding. Thermal stresses I*. Ed. by R.B. Hetnarski. Elsevier Science Publ. B.V.
5. Makhnenko, V.I., Velikoivanenko, E.A., Makhnenko, O.V. et al. (2000) Investigation of effect of phase transformations on residual stresses in circumferential welding of pipes. *The Paton Welding J.*, **5**, 2–7.
6. Junek, L., Slovacek, M., Prantl, A. (2002) Thermal and stress analysis of fusion welding process incorporating microstructure effect. In: *Proc. of Int. Conf. on Mathematical Modeling and Information Technologies in Welding and Related Technologies* (Catsiveli, Crimea, 16–20 Sept. 2002). Ed. by V.I. Makhnenko, Kiev: PWI, 161–170.
7. Bokota, A., Piekarska, W. (2003) State stresses in the heat-affected zone during laser welding process. *Mechanical Eng.*, **6**, 27–32.
8. Bokota, A., Piekarska, V. (2004) Stress state of joints made by laser welding with heating. In: *Proc. of Int. Conf. on Mathematical Modeling and Information Technologies in Welding and Related Technologies* (Katsiveli, Crimea, 13–17 Sept. 2004). Ed. by V.I. Makhnenko. Kiev: PWI, 32–37.
9. Ossenbrink, R., Michailov, V., Wohlfahrt, H. (2004) Numerical simulation of welding stresses and distortions in consideration of temporal and local changes of strain rate. *Ibid.*, 144–148.
10. Pekarska, V. (2007) Numerical simulation of metal structure in HAZ in welding of increased strength steel. *The Paton Welding J.*, **4**, 5–10.
11. Zienkiewicz, O.C., Taylor, R.L. (2000) *The finite element method*. Vol. 1–3. 5th ed. Butterworth-Heinemann.
12. Coret, M., Combescure, A. (2002) A mesomodel for the numerical simulation of the multiphasic behavior of materials under anisothermal loading (application to two low-carbon steels). *Int. J. of Mechanical Sci.*, 1947–1963.
13. Coret, M., Calloch, S., Combescure, A. (2004) Experimental study of the phase transformation plasticity of 16MND5 low carbon steel induced by proportional and nonproportional biaxial loading paths. *European J. of Mechanics A/Solids*, **23**, 823–842.
14. Hougardy, H.P. (1990) Calculation of the isothermal transformation into different microstructures from measurements with continuous cooling. *Materials Technology, Steel Research*, 61(**10**).
15. Melander, M. (1985) *Computational and experimental investigation of induction and laser hardening*. Linkoping Studies in Sci. and Techn.: Dissertation 124. Linkoping.
16. Koistinen, D.P., Marburger, R.E. (1959) A general equation prescribing the extent of the austenite-martensite transformation in pure iron-carbon alloys and plain carbon steels. *Acta Metallurgica*, **7**, 59–60.
17. Guer, H.C., Tekkaya, E.A. (2001) Numerical investigation of nonhomogeneous plastic deformation in quenching process. *Materials Sci. and Eng.*, 164–169.
18. Taleb, L., Sidoroff, F. (2003) A micromechanical modeling of the Greenwood–Johnson mechanism in transformation induced plasticity. *Int. J. of Plasticity*, 1821–1842.

QUALITY ASSESSMENT OF LASER-WELDED JOINTS OF DIE-CAST MAGNESIUM ALLOYS*

P. KOLODZIEJCZAK[1] and W. KALITA[2]
[1]Warsaw University of Technology, Warsaw, Poland
[2]Institute of Fundamental Technological Research, PAS, Warsaw, Poland

The paper presents the methods applied for the quality assessment of the magnesium alloy joints obtained by the CO_2-laser welding. Die-cast magnesium alloys AZ91 and AM50 have been butt-welded using helium as a shielding gas.

Keywords: *laser welding, magnesium alloys, shielding gas, welded joint quality, microstructure, distribution of hardness and microheterogeneity, static strength, corrosion resistance*

The magnesium alloys gained lately increasing interest of automotive industry mainly because of their much lower density with respect to traditional materials like steel and aluminum alloys. In the recent years the development of new magnesium alloys with mechanical properties comparable with traditional materials [1] led to their applications as the die-casting parts [2]. In effect it was possible to fulfill the sharpening requirements for enviromental protection [3] and transportation safety [4] through the vehicle mass reduction and consequently the fuel savings. However, the production and processing of sheet elements and modular lightweight structures of magnesium alloys are still in progress. In this matter the special concern is given to welding, particularly to laser beam welding of magnesium alloys [5–17].

The unique features of laser welding may be summarized as follows:

- very high power density of focused beam enables to join the elements with keyhole effect of welding (deep and narrow seam);
- specific energy (defined as the ratio of laser power to welding speed) necessary to obtain the firm joint is much smaller than in conventional methods, so the heat-affected zone is thin;
- no filler material is required.

The main parameters of laser welding, i.e. laser power and velocity of scanning, are the ones of simple choice: usually for given thickness of elements to be joined the maximum disposable power is applied and appropriate velocity is accomodated for stable and full penetration welding. The process parameters are the focal point position, kind of shielding gas and means of its supplying. Although the helium shielding is much more expensive than argon or nitrogen, the welding with helium provides better shape of the seam, surface quality, less pores and faster welding.

The optimum position of beam focal point (with respect to facing surface) depends on the material properties, its thickness and focus length. For magnesium alloys with low melting (~ 660 °C) and boiling point (~ 1100 °C) the plates of up to 5 mm thickness may be butt-welded with focal position at the facing surface [5].

Several methods should be utilized for the quality assessment of the laser-welded joints. Due to the action of the laser beam and fusion zone creation the microstructure of processed material changes considerably. Microscopic structure inspection provides informations about the shape of the fusion zone, changes in grain size, appearance of precipitates, porosity and occurrence of cracks. In consequence the hardness profiles on the cross sections perpendicular to the direction of beam scanning are different from those of parent material. The irradiation by the focused laser beam may cause evaporation of material and thermocapillary convection, and recrystallization can alter the chemical compound after welding, so the analysis with X-ray microprobe to determine the elemental distribution is desirable. The mechanical properties of the joints are revealed by the tests on the Instron stand for static tensile strength and the resistance of the joints to transverse loads. After the fracture of workpieces the SEM images of fractures may be compared with fractures of the parent material.

Corrosion properties of magnesium alloys strongly depend on the method of their production. The development of new technologies permitted to obtain high purity alloys and the corrosion resistance greatly improved [18, 19]. The changes in the processed material introduced by laser welding (modification of composition, compound separation, occurrence of intermetallic phases, increased precipitations) may alter the corrosion resistance of the weld in comparison to parent material. For the samples of as-cast materials and samples with the joints the comparative corrosion resistance tests can be performed by simple immersion test, as well as by electrochemical method, followed by microscopic examinations. For more detailed examination of welded structural components also the fatigue tests and the tests for strain rate sensitivity (as for crashworthy components [20]) may be included.

*From the International Conference «Laser technologies in welding and materials processing», 29 May–1 June, 2007, vil. Katsieveli, Crimea, Ukraine.

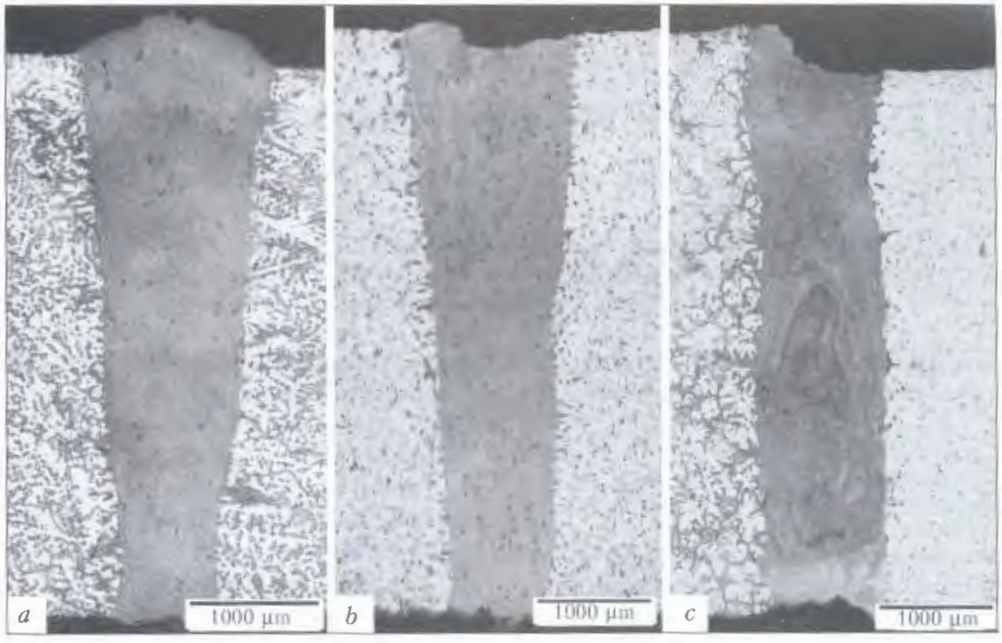

Figure 1. Macrosections of butt-welded joints of similar and dissimilar alloys: *a* — AZ91–AZ91; *b* — AM50–AM50; *c* — AZ91–AM50

This paper presents some results of application of these methods for the quality assessment of the joints of magnesium alloys obtained by the CO_2 laser beam keyhole welding.

Experimental details. The butt welding of plates of similar and dissimilar alloys has been performed with CO_2 fast axial flow laser at maximum power of 2.5 kW. The beam with the mode close to TEM_{10} was focused to the diameter of 0.25 mm by the ZnSe lens of 5". No filler metal has been used. Two cast magnesium alloys AM50 (5.0 Al, 0.3 Mn, < 0.2 Zn) and AZ91 (9.0 Al, 0.17 Mn, 0.7 Zn) were machined from the as-cast bars to the plates with thicknesses from 2.0 to 4.5 mm, width of 50 mm and the length of welding edges of 100 mm. In this paper we present results obtained for the plates 4.5 mm thick.

After some attempts the conditions of welding were chosen as follows: laser power has been set at 2 kW, welding speed — at 4 m/min, and after evaluation of the influence of the focal point position (with respect to material surface) on the profile of fusion zone, the beam focal position has been set on the upper surface of plates. The helium shielding of the facing surfaces was provided from the nozzle of 4 mm in diameter with the flow rate of 15 l/min, and the bottom surfaces were shielded by the blow of argon.

The microstructures and the hardness profiles have been evaluated on the cross-sections perpendicular to the direction of beam scanning, as well as on the cross-sections done parallelly to the facing surface along the seam. In order to find any changes due to the action of laser beam (e.g. evaporation of material and convection) the analysis of elemental distribution of basic elements has been performed with X-ray microprobe. The mechanical properties of the joints have been revealed by the tests on the Instron stand for static tensile strength and on the 3-point bending stand. After the fracture of workpieces the SEM images of fractures were obtained to compare with fractures of the parent material. The comparative corrosion resistance tests have been performed by electrochemical method (cyclic voltametry) followed by microscopic examinations.

Results and discussion. The macrostructures of the butt-welded joints of similar and dissimilar alloys are presented in Figure 1. The boundaries of the fusion zones are nearly parallel and the aspect ratios of welds (thickness of a plate to mean width of the fusion zone)

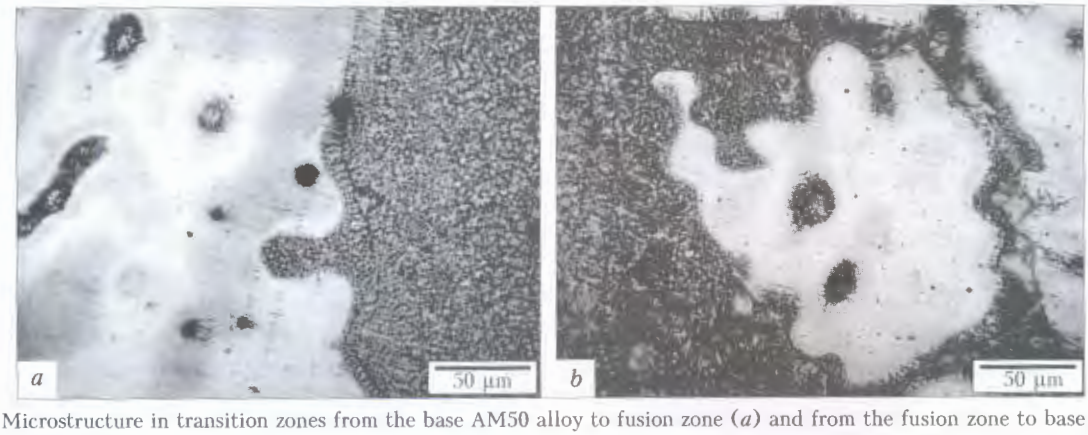

Figure 2. Microstructure in transition zones from the base AM50 alloy to fusion zone (*a*) and from the fusion zone to base AZ91 alloy (*b*) in AM50–AZ91 joint

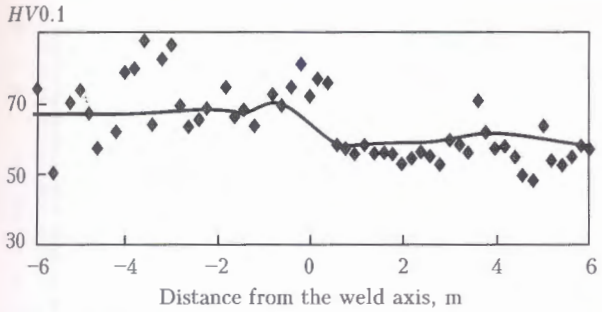

Figure 3. Microhardness profile for joint of dissimilar alloys AZ91–AM50 measured at 1.5 mm from the facing surface

are of high value indicating that the keyhole effect of beam penetration was responsible for the joining. The parent materials contained no pores, and after welding the fusion zones are practically free of them. Also, no cracks are observed.

Due to the short (less than 4 ms) time of beam irradiation and fast solidification, the fusion zones are characterized by significant grain refinement. The sharp transitions from the base metal to the fusion zone may indicate that there is no heat-affected zone. On the microscopic blow-up it may be observed that the distinguished direction of crystallization concerns only one-grain layer on the AM50 side of the joint (Figure 2).

The measurements of hardness distributions in the cross sections of welds (perpendicular to the direction of welding) for joints of similar alloys have shown significant increase of hardness in the fusion zones in comparison to the base material. These results may be associated not only with the high grain refinement in the weld but also with the increase of precipitations at the grain boundaries and appearance of intermetallic compounds. For the joints of dissimilar alloys no such effects are observed (Figure 3).

For the determination of the changes in the chemical composition of material caused by the influence of beam action, the measurements of elemental distributions have been performed by means of the Philips X-ray microprobe XL-30. It was found that due to the very low boiling point of magnesium (~1100 °C) in comparison with that of aluminum (~2300 °C), the percentage share of magnesium in the joints has been slightly decreased by evaporation of this element (especially in the AZ91–AZ91 joint). Due to the high grain refinement in the fusion zones the amplitudes of the elemental concentration changes have been

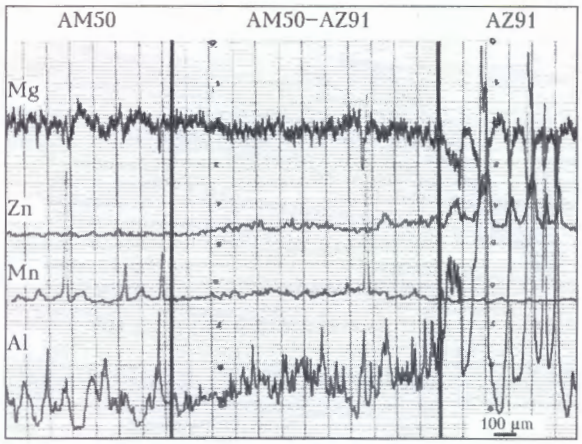

Figure 4. Elemental distributions across the joint of AM50 and AZ91 alloys measured at the half of the cross section thickness

much smaller than outside welds. Particularly, interesting are the elemental distributions in the joints of dissimilar alloys AM50–AZ91. Measurements performed at different depths of the joints may indicate the influence of thermocapillary convection and consequent mixing. In effect the greatest changes in the composition across the joint can be observed near the facing and bottom surfaces, while the profiles of elemental distributions at the half of the thickness are relatively smooth (Figure 4).

The static tensile tests of samples of parent alloys and the welds were performed on the Instron stand. The stress versus strain curves for joints of similar alloys and the base metals are presented in Figure 5. It has been observed that the fracture of welded samples for all alloys appeared far from the fusion zone boundaries, namely in the region of base metal. As it could be expected, the samples with joints have smaller elongation at fracture than the parent materials, however there are differences for tensile stress: for AM50–AM50 joint the stress at fracture is lower and for AZ91–AZ91 higher than those for base metal samples. For the AZ91–AM50 joints the workpieces broke at the AZ91 side, also far from the fusion zone. The comparison of stress–strain curves for all joints is given in Figure 6. According to anticipations the elongation at fracture for dissimilar joints has the value between those of the joints of brittle alloy AZ91 and the ductile alloy AM50. Since the fracture of the welded samples occurred far from the fusion zones, the SEM images of fracture surfaces of the workpieces

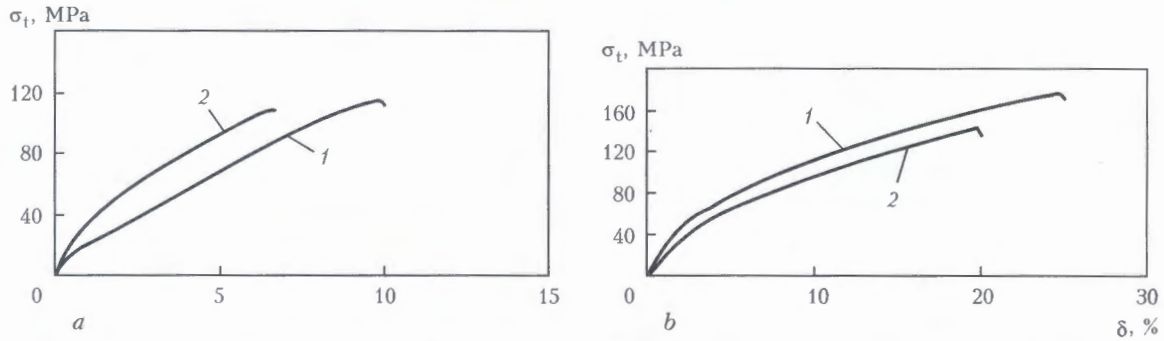

Figure 5. Tensile stress–strain curves for samples of parent materials (*1*) and the joints (*2*) of AZ91–AZ91(*a*) and AM50–AM50 (*b*)

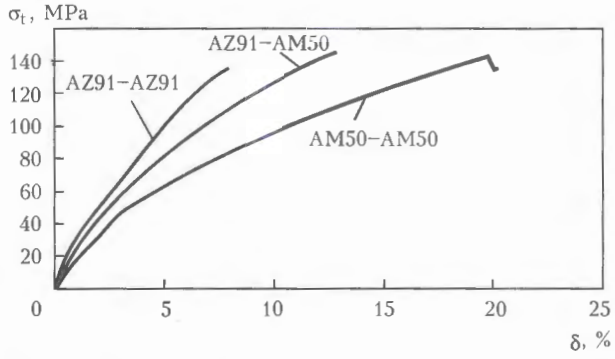

Figure 6. Tensile stress–strain curves for the joints of similar and dissimilar alloys

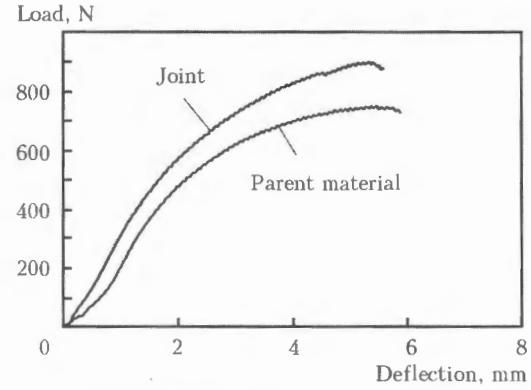

Figure 7. Load versus deflection for AZ91 alloy

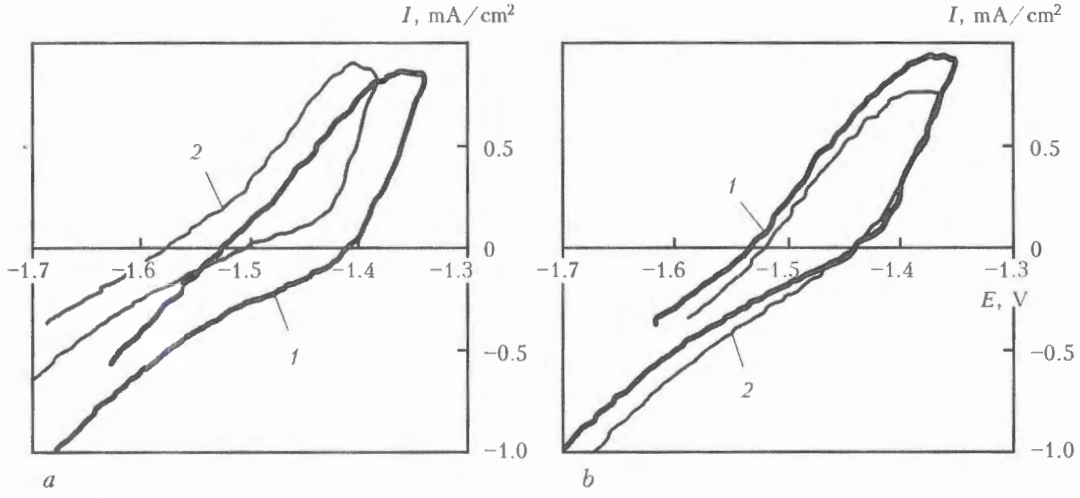

Figure 8. Current–potential curves for welded (*1*) and unwelded (*2*) AZ91 (*a*) and AM50 (*b*) alloys

of parent materials and samples with the joints displayed no differences.

The static bend tests were performed on the 3-point bend stand (support rollers spacing of 70 mm, the rollers diameter of 30 mm). The differences between the samples with weld and unwelded material have been observed only for the joint of brittle AZ91 alloy, where the peak load for base metal is lower than for the joint (Figure 7).

Corrosion behavior of welded and unwelded samples of approximately equal (1 cm^2) surface area was examined by means of electrochemical method. Measurement were carried out in the aerated 0.9 % NaCl solution; three electrode cell consisted of working electrode (magnesium alloy), counter (platinum) and reference electrode (saturated calomel electrode). The measurements were realized with a potential sweep 1 mV/s from −100 to +300 mV. The polarisation curves for welded and unwelded samples for AZ91 and AM50 alloys are shown in Figure 8.

From the comparison of polarisation curves for welded and unwelded samples it may be concluded that practically there are no differences in corrosion resistance.

CONCLUSIONS

1. Welding of similar and dissimilar alloys in the same conditions (for plate 4.5 mm thick, 2 kW laser power, 4 m/min speed, in helium shielding and focal position at facing surface) resulted in high aspect ratios of the fusion zones with nearly parallel boundaries, practically pores free and without cracks. No heat-affected zone may be observed.

2. The high grain refinement and increased precipitations in the fusion zones heightened the hardness in these regions in comparison with parent material.

3. In the static tensile tests the fractures for all joints occurred far from the weld, namely in joints of dissimilar alloys on the side of brittle alloy AZ91. The plastic properties of samples with welds are lower than for the parent materials. In the bending tests the differences between the welded and unwelded samples can be observed only for the joints of brittle AZ91 alloy.

4. The results of corrosion immersion tests performed in 0.9 % NaCl solution showed that welding of dissimilar magnesium alloys, in this case AZ91–AM50, increases a susceptibility to galvanic corrosion even if the differences between electrode potential values are not apart each other. However an influence of a weld is rather negligible. The corrosion resistance tests performed by electrochemical method for joints of similar alloys have shown practically no differences in comparison with parent material.

1. Friedrich, H., Schumann, S. (2001) Research for a «new age of magnesium» in the automotive industry. *J. Materials Processing Technology*, **117**, 276–281.

2. Longworth, S.J.P. (2001) *The bolting of magnesium components in car engines*: Diss. for Master of Philosophy Degree to University of Cambridge.
3. Aghion, E., Bronfin, B., Elieze, D. (2001) The role of magnesium industry in protecting the environment. *J. Materials Processing Technology*, **117**, 381–385.
4. Mordike, B.L., Ebert, T. (2001) Magnesium. Properties–applications–potential. *Material Sci. and Eng. A*, **302**, 37–45.
5. Weisheit, A., Galun, R., Mordike, B.L. (1998) CO_2 laser beam welding of magnesium-based alloys. *Welding Res. Suppl.*, 77(**4**), 149–154.
6. Dhari, M., Masse, J.E., Mathieu, J.F. et al. (2001) CO_2 laser weldability of WE43 magnesium alloy for aeronautic industry. In: *Proc. of LANE* (Erlangen, Germany, Aug. 28–31, 2001), 297–310.
7. Zhao, H., Debroy, T. (2001) Pore formation during laser beam welding of die-cast magnesium alloy AM60B — mechanism and remedy. *Welding Res. Suppl.*, 204–210.
8. Sun, Z., Wei, J., Pan, D. et al. (2001) A comparative evaluation on microstructures in TIG and laser welded AZ31 magnesium alloy. In: *SIMTech Technical Report PT/01/008/JT*, 1–8.
9. Hakekamp, H., Goede, M., Bormann, A. et al. (2001) Laser beam welding of magnesium alloys — new possibilities using filler wire and arc welding. In: *Proc. of LANE* (Erlangen, Germany, Aug. 28–31, 2001), 333–338.
10. Watkins, K.G. (2003) Laser welding of magnesium alloys. In: *Proc. of Magnesium Technology Conf.* (San Diego, USA, March 2–6, 2003), 153–156.
11. Stern, A., Munitz, A., Koln, G. (2003) Application of welding technologies for joining of Mg alloys. Microstructure and mechanical properties. *Ibid.*, 163–170.
12. Lathabai, S., Barton, K.J., Harris, D. et al. (2003) Welding and weldability of AZ31B by gas tungsten arc and laser beam. *Ibid.*, 157–162.
13. Kalita, W., Kolodziejczak, P., Pokhmurska, H. (2003) Welding of Mg-based alloy AM20 by CO_2 laser beam. In: *Proc. of Int. Conf. on Laser Technologies in Welding and Materials Processing* (Katsiveli, Ukraine, May 19–23, 2003), 214–216.
14. Dasgupta, A.K., Mazumder, J. (2004) Laser welding of AM60 magnesium alloy. In: *Proc. of Magnesium Technology Conf.* (Charlotte, USA, March 14–18, 2004), 43–48.
15. Kolodziejczak, P., Kalita, W., Hoffman, J. et al. (2004) Laser welding of magnesium-based alloys of MgAlZn group. *Advances in Manufacturing Sci. and Techn.*, 28(**4**), 45–53.
16. Kalita, W., Kolodziejczak, P., Kwiatkowski, L. et al. (2004) Properties of the butt-welded joints of CO_2 laser welded Mg alloys. In *Proc. of LANE* (Erlangen, Germany, Sept. 21–24, 2004), Vol. 1, 317–328.
17. Kalita, W., Kolodziejczak, P., Kwiatkowski, L. (2005) Properties of the CO_2-laser welded joints of dissimilar magnesium alloys. In: *Proc. of 2nd Int. Conf. on Laser Technologies in Welding and Materials Processing* (Katsiveli, Ukraine, May 23–27, 2005), 79–84.
18. Li, P.Y., Yu, H.J., Chen, S.C. et al. (2003) Factors affecting the corrosion resistance of cast magnesium alloys. In: *Proc. of Magnesium Technology Conf.* (San Diego, USA, March 2–6, 2003), 51–58.
19. Kwiatkowski, L., Grobelny, M., Kalita, W. et al. (2005) Corrosion properties of the butt-welded joints of laser welded Mg alloys. *Inzynieria Powierzchni A*, II(**2**), 191–197.
20. Abbott, T., Easton, M., Schmidt, R. (2003) Magnesium for crashworthy componenents. In: *Proc. of Magnesium Technology Conf.* (San Diego, USA, March 2–6, 2003), 227–230.

LASER-BASED WELDING AND BRAZING IN AUTOMOTIVE PRODUCTION — INVESTIGATIONS TO REDUCE FAILURES AND IMPERFECTIONS*

F. ALBERT, A. GRIMM, C. KAGELER and M. SCHMIDT
Bayerisches Laserzentrum GmbH, Erlangen, Germany

Laser welding and brazing are gaining more importance in today's automotive production. Both methods offer the potential for fast joining processes and a decrease of rework. A robust process management is, however, a precondition to achieve defect-free welding and brazing results. Two research projects are focusing on this problem at the Bavarian Laser Center (Bayerisches Laserzentrum). Solutions for laser welding of zinc-coated steel sheets in an overlap configuration and laser brazing of visible joints are examined.

Keywords: *laser welding and brazing, automotive production, thin sheet structures, zinc-coated sheet, joint defects, power modulation parameters*

Welding of zinc-coated thin steel sheets in an overlap joint configuration is mainly used in production of car bodies. Even when latest research results and technological improvements are taken into account, it is difficult to control or predict the behaviour of a laser welding process of such sheets in a zero-gap assembly. In the majority of cases, the coatings on the sheet surface have a lower evaporation temperature than the melting point of steel itself (T^{st}_{melt} > 1800 K; T^{Zn}_{evap} = 1180 K). When welding in a zero-gap assembly, the degassing of the vaporized zinc between the sheets is impossible in most cases. Therefore, it exhausts through the keyhole, disturbing the balance of pressure and the hydrodynamic processes in the weld pool. Results are imperfections or failures in the weld (Figure 1).

However, there are several possibilities to have an external influence on the laser welding process and the weld quality. One method presented in this paper is based on the modulation of the laser power, which should generate a stable keyhole dynamic and the possibility to permit the permanent degassing of vaporized zinc through the keyhole, as well as to avoid failures as a result of keyhole collapses. The interactions of the power modulation with the keyhole and the liquid material are analyzed by means of high-speed images, optical process signals and welding results.

Figure 1. Weld of zinc-coated steel sheets in zero-gap overlap joint configuration

Laser brazing is also an important joining technology for visible joints of car bodies. Even today failures like pores, holes, spilling and one-sided melting of the sheets cannot be completely avoided and post-process quality checks are mandatory. In this case the accuracy of the used robot and fluctuations of laser power or focal position are the determining factors for the formation of failures. The expensive post-process checks could be avoided by means of a pyrometer-based on-line quality control, which is also discussed in this article. The use of this temperature-based on-line monitoring system allows detecting the mentioned failures. Furthermore, it is the basis of a closed-loop process control in order to adjust the position of the robot, as well as the laser power and focal position. The realized system-technology and results of brazing experiments and pyrometer signals will be discussed.

Laser welding of zinc-coated steel sheets. The experimental setup is shown in Figure 2. Based on a

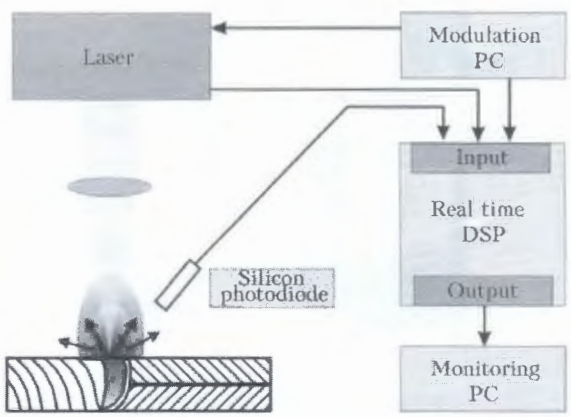

Figure 2. Schematic diagram of the experimental setup

*From the International Conference «Laser technologies in welding and materials processing», 29 May–1 June, 2007, vil. Katsieveli, Crimea, Ukraine.

deep-penetration process, two zinc-coated steel sheets with thicknesses of 0.6 and 0.7 mm are overlap-welded with a technical zero-gap. The zinc coatings have an average thickness of 10 μm. The laser source is a Yb:YAG disk-laser with a maximum continuous output power of 4 kW at 1030 nm. The beam quality product is about 9.2 mm·mrad (M^2 = 27.4), the focus diameter is 600 μm, and the focal length is 450 mm.

The optical emissions of the welding process are detected by a silicon photodiode with a spectral range from approximately 400 up to 1100 nm filtered by a band pass at 530 nm. The laser output power, the modulation signal and the process emissions are detected simultaneously with a sample rate of 50 kHz. The viewing angle from the photodiode is about 80°, oriented to the horizontal reference line.

In order to affect the keyhole oscillations, the laser output power is modulated around an average power P = 3.6 kW. As mode of modulation, a normal sinus curve is mostly chosen. To avoid resonance effects when modulating near the eigenfrequency of the keyhole dynamic over a longer period of time, the carrier frequency is changed by a frequency modulation. The carrier signal directly represents the current laser output power. By changing the frequency shift or the offset, for instance, the range of the laser output power can be defined. An exemplary modulation signal used in the experiments can be seen in Figure 3.

With regard to avoiding failures during deep-penetration laser welding of zinc-coated steel sheets an important aspect is the existence of small pressure fluctuations of the keyhole in a certain frequency range. Welding results of non-contaminated sheets show that the welding depth, for example, is much more constant, the smaller the frequency range is where the fluctuations arise [1].

To describe this phenomenon some basic considerations are necessary, namely in deep-penetration laser welding complex physical processes superpose each other. A keyhole with an opening towards the laser beam is generated by the vaporizing material. It is

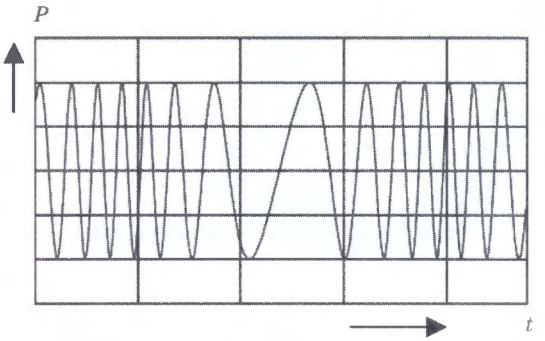

Figure 3. Exemplary waveform of the frequency modulation used to the laser output power control

surrounded by the pool which consists of liquid steel. The gaseous material flows towards the opening of the capillary causing a decrease of pressure within the keyhole. If a stable welding process is needed, this loss of pressure has to be compensated by continuously vaporizing new material. The equilibration of the vaporization–pressure, generated by the vaporizing steel, and the pool–pressure of the liquid steel keep the keyhole open. This balance of pressures is formed by the external pressure, consisting of the surface pressure p_{surf}, the hydrostatic pressure p_{hst} and the hydrodynamic pressure p_{hdn}, and the internal pressure, consisting of the ablation pressure p_{abl}, as well as the gas flow pressure p_{gas}. The interaction of these internal and external pressures leads to a specific dynamic of the keyhole. A FFT-analysis of the optical emissions during a non-modulated laser welding process of two zinc-coated steel sheets (overlap configuration, 100 μm gap) shows this characteristic eigenfrequency of the keyhole oscillation (Figure 4).

An imbalance of pressures inside and outside of the keyhole can occur by varying process parameters like varying zinc thickness or geometry (gap size), laser power and welding speed. When welding zinc-coated sheets an area of high pressure, vapour exists around the melt pool. If the gap between the sheets is narrow, the vapour cannot extend outwards, pres-

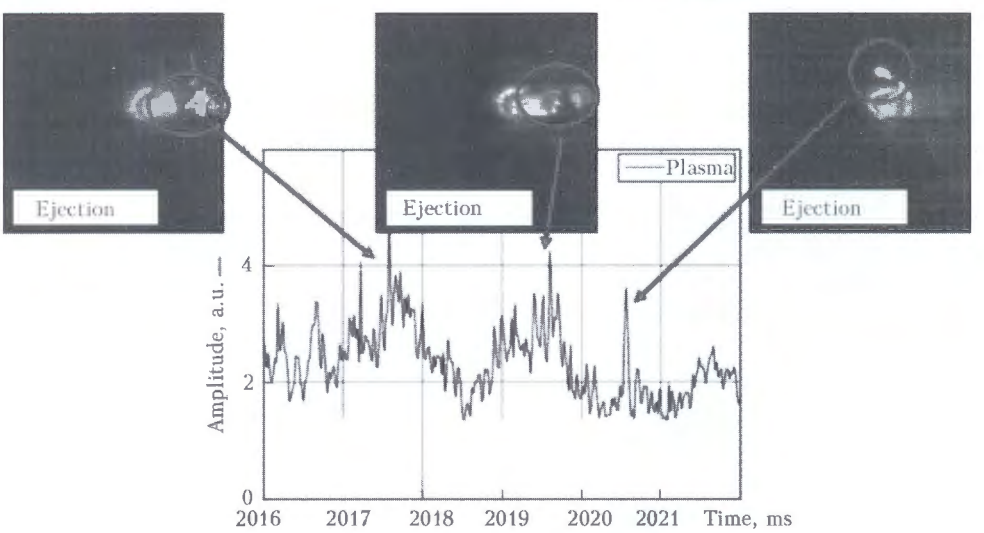

Figure 4. Time signal of optical emissions during CW-laser overlap welding of two zinc-coated steel sheets with thickness of 0.6 and 0.7 mm and zero-gap at P = 3600 W, v_w = 6 m/min, λ = 1030 nm, d_{spot} = 600 μm

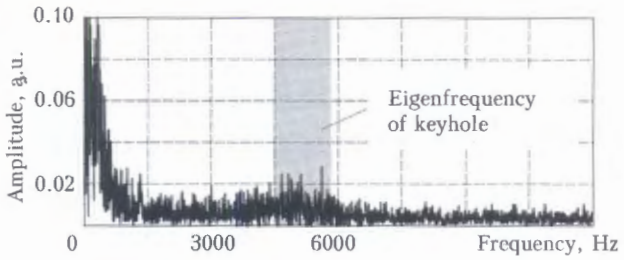

Figure 5. Frequency spectrum of CW-laser overlap welding of two zinc-coated steel sheets with thickness of 0.6 and 0.7 mm and 100 μm gap at P = 3600 W, v_w = 6 m/min, λ = 1030 nm, d_{spot} = 600 μm

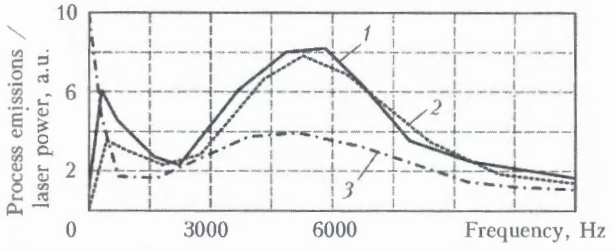

Figure 7. Transfer function for laser welding of zinc-coated steel sheets 0.6 and 0.7 mm thick at P = 3.6 kW, v_w = 6 m/min, d_{spot} = = 600 μm: *1* — 40; *2* — 120; *3* — 200 W

sure fluctuations of the keyhole arise and failures are generated. The explosive degassing process disturbs the welding process and the keyhole collapses due to the disequilibrium of pressures (Figure 5). With expelling, a high amount of the liquid steel from the melt pool is carried away, causing cavities, spillings or pores within the weld. As a result the mechanical properties of the weld are directly affected in a negative way [2–7]. Furthermore the eigenfrequency of the keyhole is not detectable in this case and the whole welding process is instable.

It is the aim to define effective modulation parameters for positively influencing the welding process by an always opened keyhole. This demand is pursued if the frequency range of the power modulation is near the eigenfrequency of the keyhole dynamic. This is equitable if the peaks in frequency range of process emissions are in the same range as the frequency of power modulation. In experiments the attenuation of the process can be determined by calculating a transfer function with frequency information of process emissions and laser power.

During one welding process of at least 300 mm weld length the frequency of power modulation is changed between f = 0 and f = 10 kHz and the optical emissions, as well as the modulation parameters are detected. This information allows the generation of the transfer function and the definition of useful modulation frequencies (Figure 6).

Figure 7 exemplary shows such a transfer function for a welding process under conditions described above. A low attenuation can be seen between 4.5 and 6.0 kHz. The necessary carrier frequency for the power modulation has to be in the same range.

Other facts about the modulation like modulation depth (amplitude), as well as the frequency shift and the velocity of frequency shift, are not detectable. Last data have to be determined by further experimental investigations.

As can be seen in Figure 8, power modulation with a carrier frequency in the described range leads to an open keyhole during the whole welding process. Without modulation the size of the keyhole will be disturbed and collapses are detectable by high-speed pictures.

First welding results clarify a reduction of failures (cavities) when a power modulation is applied. Figure 9 presents the number of cavities at 300 mm long welds. The results prove that a reduction of failures is possible but still to the actual state of research no zero defect rate is reached.

An analysis of further results reveals that failures can also form behind the keyhole. A stable keyhole is thus only one step to minimize failures. Additional efforts have to be made to realize a second degassing possibility and to reach welds without defects.

On-line quality control for laser brazing. This part of the article deals with the development of an on-line monitoring system for laser brazing with high-power diode lasers which permits the on-line detection of failures like pores, holes, spilling and one-sided melting. Furthermore, this system is the basis of a closed-loop process control in order to abandon the expensive post-process quality controls.

A promising new approach for on-line process monitoring and control is the locally defined measurement of the temperature field of both joining partners. First tests have confirmed a correlation between temperature and seam quality. The temperature meas-

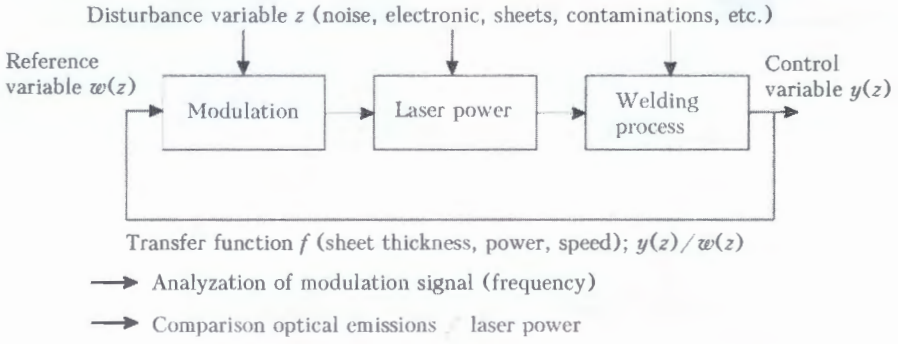

Figure 6. Model for determining transfer function and defining modulation parameters

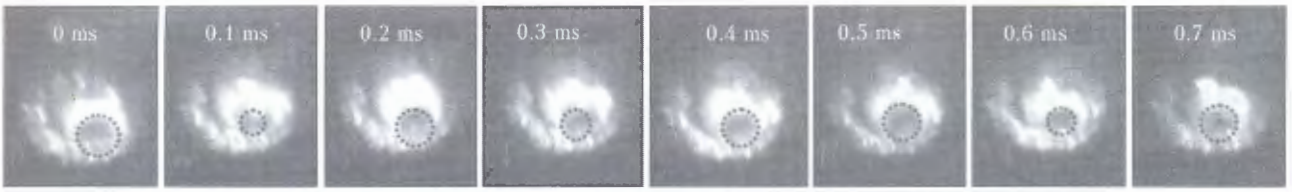

Figure 8. High-speed pictures of the keyhole in welding of sheets 0.6 and 0.7 mm thick with power modulation at P = 3.6 kW, $f_{carrier}$ = = 4.5 kHz, v_w = 6 m/min, d_{spot} = 600 μm

urement via pyrometers turned out to be most advantageous (Figure 10).

A new on-line process monitoring and control system based on temperature measurement promises an enormous reduction of manufacturing costs for laser brazing. Thus, this process will become even more attractive for the automotive industry. With the assistance of a capable temperature measurement system based on pyrometers, this project wants to detect failures in the seam so that these failures can be avoided in a closed-loop controlled process afterwards. This can be achieved by investigations in the measurement of temperature during the brazing process and integration of thermal detectors as to receive information about the effects of unadjusted temperature control on the brazing result. A further aim is the implementation of the temperature measurement into a brazing head with a wire feeding system for high-power diode lasers with best conditions of detection. Last but not least, the result will be a temperature-based robot- and laser-control.

The research is realized on a laser brazing system, including a wire feeding device and a fiber-guided high-power diode laser with a maximum output power of 2.7 kW. Due to the optics which are integrated in the brazing head and the light conduction cable, the laser spot diameter at the end of the wire is 3.1 mm. The most important parts of the experimental setup are two integrated pyrometer optics which are connected by optical fibers to pyrometers. A two-color measurement technology is used to be independent of the emission factor that detects temperatures between 500 and 1300 °C at wavelengths of 1.52 and 1.64 μm with a response time t_{90} of up to 2 ms. The measuring is carried out in mono-mode at ε = 0.8. Due to the process dynamics and the continuous change between molten and solid materials at the processing zone, it has to be considered that a proper identification of the emissivity and thus an absolute specification of the temperature is not possible. The diameters of the measuring spot can be adjusted between 1 and 5 mm.

The investigations are done on linear edge raised joints of DX 54 D + Z100 deep drawing steel sheets, a typical thin sheet for automotive body parts, with a thickness of 0.8 mm. Brazing speed of 2.1 m/min and laser power of 2700 W have turned out to be ideal parameters in terms of surface quality of the seam and filling degree.

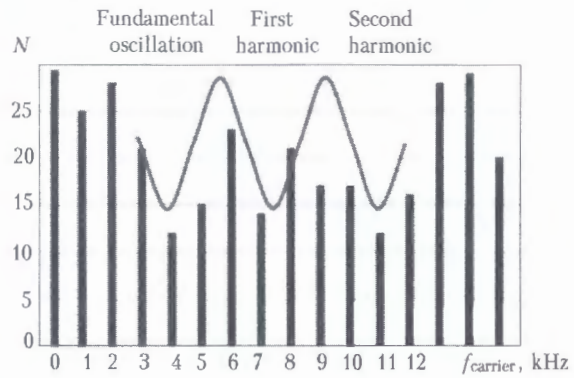

Figure 9. Number of cavities N at 300 mm long weld in relation to the carrier frequency f of power modulation at P = 3.6 kW

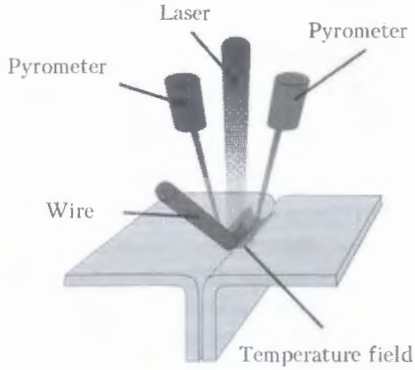

Figure 10. Principle setup of the process monitoring system

Figure 11 shows some top views of intentional defective parts with linear edge raised joints. Starting from an ideal adjustment of the brazing head towards the joint (Figure 11, *a*) the lateral deviation of the path is constantly extended up to 0.3 mm (Figure 11,

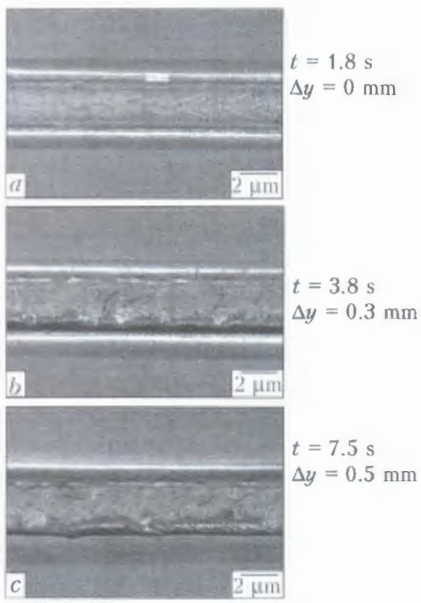

Figure 11. Top views of clear seam (*a*), lateral misalignment of 0.3 (*b*) and 0.5 (*c*) mm

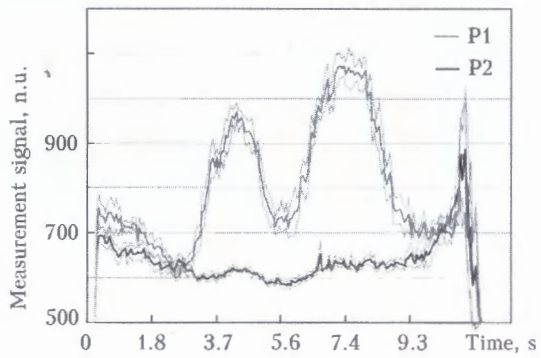

Figure 12. Signal sequence at lateral misalignments of 0.3 mm (3.8 s) and 0.5 mm (7.5 s), number of samples $n = 5$

b). Afterwards the brazing head returns back to the ideal position in order to be moved out of this location again. Lateral misalignment in this time is up to 0.5 mm (Figure 11, *c*); at the end there is no intentional misalignment.

The two pictures with the lateral deviation indicate obvious melting of the lower steel sheets, whereas the melting at the misalignment of 0.5 mm naturally exceeds the melting (see Figure 11, *b*).

With the help of the measurement system which is described above, signal sequences of these processes are acquired (Figure 12).

The sequence above clearly reveals the two misalignments. Furthermore, the two failures differ in their signal amplitude which can be traced back to the different deviation and melting respectively.

Intentional variations of the laser power can also be detected in the signal sequences. Both pyrometer signals increase at power variations $\Delta P = 700$ W each at 3.7 and 7.6 s (Figure 13).

Consequently, the sensor signals allow a differentiation between types of failures and different intensity of the failures.

The results prove the possibility of an on-line quality monitoring system for laser brazing. The investigations of best condition for detection as well as first applications of the measurement system at intentional defective parts clearly show the existing potential.

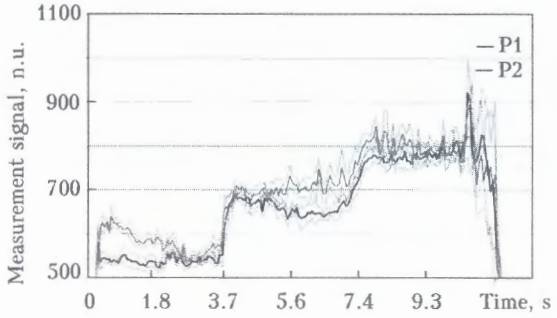

Figure 13. Signal sequence at variations of the laser power of 700 W, $n = 5$

The current steps of the project include the qualification of the measurement system for fillet joints and complex 3D seam geometries. In the future the knowledge should be the basis for a temperature-based closed-loop process for brazing with high-power diode lasers.

Acknowledgment. *This work has been funded by the BMBF — Project FM-LaB, and the Stiftung Industrieforschung — Project Temperaturgeregeltes Laserstrahlhartloten mit Hochleistungsdiodenlaser. The authors wish to acknowledge for the support.*

1. Otto, A. (1997) *Transiente Prozesse beim Laserstrahlschweissen*: Dissertation. Reihe Fertigungstechnik — Erlangen, Bd. 65, Bamberg: Meisenbach.
2. Geisel, M. (2002) *Prozesskontrolle und -steuerung beim Laserstrahlschweissen mit der nichtlinearen Methodik*: Dissertation. Reihe Fertigungstechnik — Erlangen, Bd. 123, Bamberg: Meisenbach.
3. Hohenstein, R., Otto, A., Geiger, M. (1998) Systemanalyse des dynamischen Verhaltens beim Laserstrahlschweissen. In: *Strahl-Stoff-Wechselwirkung bei der Laserbearbeitung 2*. Bremen: BIAS, 125–130.
4. Kaplan, A. (1994) *Modellrechnung und numerische Simulation von Absorption, Warmeleitung und Stromung des Laser-Tiefschweissens*: Dissertation. TU Wien.
5. Beck, M. (1996) *Modellierung des Lasertiefschweissens*. Stuttgart: Teubner.
6. Kroos, J. (1993) *Stabilitat und Dynamik der Dampfkapillare beim Schweissen von Metallen*: Dissertation. TU Braunschweig.
7. Klein, T. (1997) *Freie und erzwungene Schwingungen der Dampfkapillare beim Laserstrahlschweissen von Metallen*. Aachen: Shaker.

METHODS OF MANUFACTURING AND APPLICATION OF RAPIDLY QUENCHED BRAZE ALLOY

I.N. PASHKOV, I.I. ILIINA, I.V. RODIN, S.V. SHOKIN and S.A. TAVOLZHANSKY
CJSC ALARM, Moscow, Russia

Methods of manufacturing rapidly quenched braze alloys in the form of 0.3–6.0 mm diameter wire from hard-to-deform materials in the plastic state are considered. Composition of braze alloys on Cu–P, Cu–P–Sn, Cu–Zn–P–Ni base and other systems develop the quasi-eutectic structure containing supersaturated solid solution with distributed phases of copper phosphide as a result of quenching. Examples of application of rapidly quenched braze alloys are given.

Keywords: *brazing, rapidly quenched braze alloys, band, wire, microstructure, manufacturing methods, application*

Processes of braze alloys manufacturing by the method of quenching from the melt, on the one hand, allow reaching high cooling speeds, which leads to a cardinal change of the structure and properties of the produced material, and on the other hand — to obtain products in such condition (for example, fibers, flakes, needles and foils) and form, which is difficult to achieve by the traditional methods. The mentioned advantages are manifested to the greatest degree in the case of producing metals and alloys brittle by their nature and hard-to-form. Besides, when providing a constant melt feeding, the process of producing materials from the melt is easy to automate and to make it continuous or semi-continuous.

Casting by drawing from the melt, continuous casting and casting by freezing are the most interesting from the point of view of making long-sized blanks, semi-finished products and items manufacturing.

Solidification of molten metal with ultrahigh (more than 10^5 K/s) speeds of cooling allows producing practically all the range of amorphous and microcrystalline materials with rather high efficiency that is already used for a long time in foreign and home practice. Technology of melt rapid solidification on a rotating disk-crucible allows producing calibrated AMS braze alloys in the form of a thin plastic band of 20–100 μm thickness and 2–50 mm width [1]. MIFI-AMETO is the manufacturer of these braze alloys in Russia.

High reactivity, purity and homogeneity of the braze alloy are the advantages of the given method that predetermine its high technological properties in brazing, possibility of accurate braze alloy portioning and diversity of its compositions, which cannot be produced by other methods, ensuring precise assembly of the brazed joint, its high quality, etc. The disadvantages of the method include high labour consumption in implementation of the technology and high product price, the need for very precise and fixed gaps in assembly of brazed joints (optimum size — 0.025–0.050 mm), considerable limitation of selection methods and equipment when choosing the brazing procedure and equipment. Application of AMS braze alloys makes higher demands of machining of the parts being brazed. Their application is complicated in mass production of brazed structures, for example, when the ends of as-delivered extruded tubes are joined by brazing. So, in manufacturing of heat exchangers, household and industrial refrigerators, radiators, etc., the gap value can vary in broad ranges in assembly (from about zero up to 0.7 mm), which is due to large tolerances on pipe diameters.

Process of braze alloy quenching from the melt was studied at one-sided heat removal [2–4] for solving the tasks of providing the users with higher metal-content products, for example wire (of 0.3–3.0 mm diameter) from brittle braze alloys.

Method of melt extraction was further developed at ALARM Company (Moscow). The method consists in extraction of the blank from the melt pool by a rotating crucible, solidifying on the crucible surface, blank separation from disk-crucible surface and winding on a special device in the form of a coil. This way, it is possible to produce wire or its segments of a not-circular cross-section (in the shape of a bean seed) of variable diameter of 0.3–3.0 mm.

Method of melt rotor casting into a rotating crucible channel was used for making rods of 3–6 mm diameter. Increase of the time of solidified material cooling on the crucible surface, simultaneously with its fastening in the channel by a running belt, allowed making copper-phosphorus braze alloys of a trapezoidal cross-section in one technological operation. Cutting with flying shares is performed immediately after separation from the crucible surface to obtain up-to-size products. To avoid product failure and violation of their integrity, the main purpose was to ensure a certain temperature of products at the moment of their separation from the disk-crucible surface. This task was solved, on one hand, by choosing the optimal crucible design, and on the other hand — by increasing time of cooled wire staying on its surface. Cooling speed is enough for formation of a fine granulation structure. Rods of copper-phosphorus braze alloys of a large cross-section can be successfully applied instead of rods angle-cast usually made at enterprises

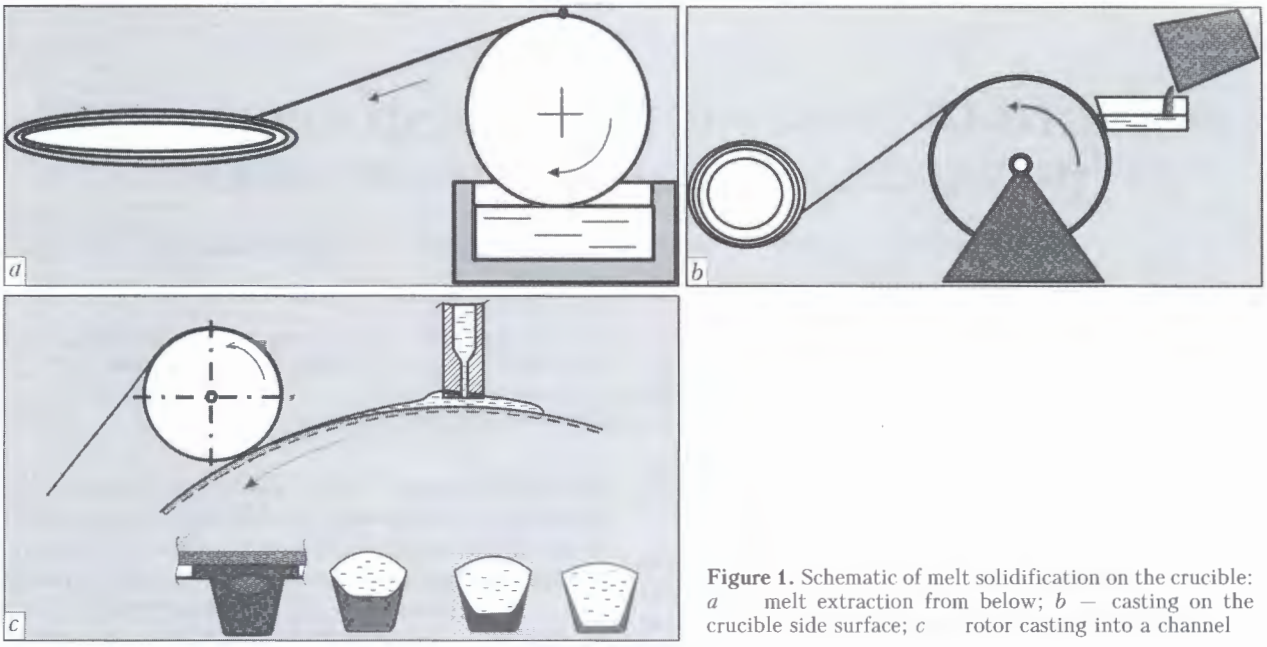

Figure 1. Schematic of melt solidification on the crucible: *a* — melt extraction from below; *b* — casting on the crucible side surface; *c* — rotor casting into a channel

from phosphorus-copper ingots that are difficult to make sufficiently strong, when their diameter is less than 10 mm. High efficiency of the method and its apparent simplicity, not requiring complex equipment, made it potentially promising for mass manufacturing of wire (rods) from hard-to-deform materials in the plastic state [3]. The schematic of melt solidification on the mould is given in Figure 1.

Utilization of high cooling rates yields high chemical and microstructural homogeneity as a result of a uniform phase distribution in the material structure. Here, the brittle phases (phosphides, intermetallics) are in the finely-dispersed state that causes increased ductility of the products and its further treatability to give it the necessary shape, for example, round cross-section wire with calibrated geometrical sizes. Homogeneous microstructure of the joint without porosity or cavities is formed in brazing with such braze alloys that in its turn promotes improvement of the brazed joint quality.

Rapid quenching from the melt is less sensitive to alloy composition compared to the traditional methods of material forming thus providing a rather wide spectrum of braze alloy compositions of the set geometry.

Processes of making wire from copper–phosphorus, copper–phosphorus–tin, copper–zinc–phosphorus–nickel alloys on copper–phosphorus base and alloys of copper–zinc–tin, copper–manganese on copper–zinc base were studied. Investigations in the microanalyzer of electron microscope Jeol 6400 showed that a metastable state of the structure with grain size below 10 μm is achieved as a result of high cooling speeds. Metallographic analysis of P14 braze alloy shows that the structure is a quasi-eutectic and consists of a supersaturated solid solution with distributed phases of copper phosphide (Figure 2).

Owing to the finely-dispersed state of the phosphides and homogeneous nature of their distribution, wire and band from braze alloys on the base of this system, have higher plastic properties, for example, P14 braze alloy wire can withstand bending over through 180° several times.

P21 braze alloys on the base of copper–zinc–tin system and P47 braze alloy on the base of copper–zinc–manganese system are advanced materials from

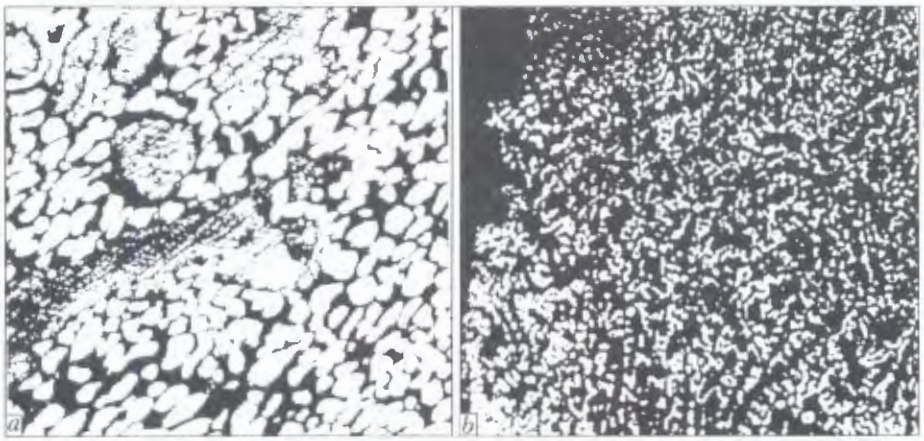

Figure 2. Microstructure of P14 braze alloy (copper–phosphorus–tin) in the cast state (*a* — ×200) and after quenching on disk-crucible (*b* — ×400)

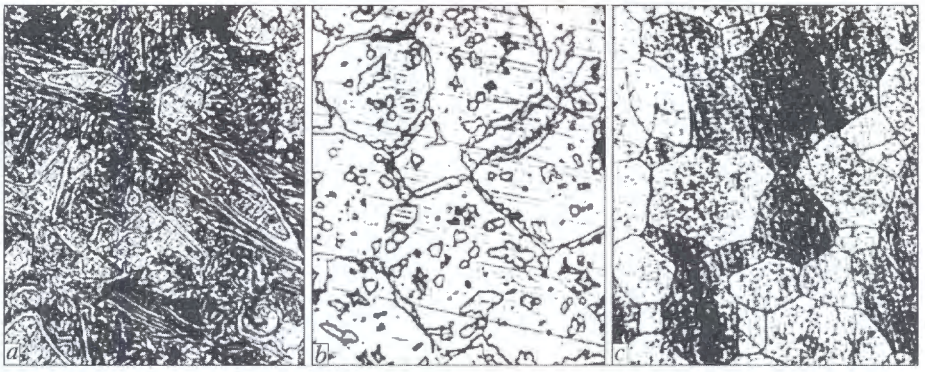

Figure 3. Microstructure of P21 braze alloy of copper–zinc–tin system in the cast (*a* — ×200), hot-pressed (*b* — ×800) state and after high speed melt solidification (*c* — ×800)

point of view of silver braze alloy replacement in the processes of brazing steels and steels with copper. The mentioned alloys belong to multi-phases brasses owing to alloying element presence in them. In the cast state they are characterized by low ductility and are hard-to-form. The interest to these braze alloys is caused by relatively low melting temperatures and, hence, of brazing compared to the usually used brasses. That is important in brazing steels to copper alloys, steels for which heating above 900 °C is undesirable, as well as in manufacturing hard alloy tools.

Rapid quenching from the melt allowed producing these materials in the shape of wire and band of a higher ductility as a result of metastable structure formation [5]. As is seen from Figure 3 and X-ray structural analysis, P21 braze alloy produced by high-speed melt solidification has a single-phase structure of β-brass as a distinct from the three-phase structure in the cast state.

P21 braze alloy has a complex composition of more than five components. Its base is copper–zinc–tin alloy, the structure of which in the cast state consists of three phases: α, β and γ-brasses. Presence of γ-brass makes the main contribution to imparting brittle properties to the alloy. Two-phase brass, in which the brittle γ-phase still remains, can be produced after hot pressing of the mentioned braze alloy in the process of making rods of 3 mm diameter, as a result of thermal impact at temperatures of about 600 °C and material deformation. High-speed melt solidification (HSMS) allowed fixing the area, in which this melt has a single-phase β-brass structure, that determined the higher plastic properties of the braze alloy in comparison with hot-pressed and cast state.

As was noted earlier, rapid quenching leads to formation of non-equilibrium structure with oversaturated solid solutions. The structure is characterized by crystal growth anisotropy because of one-sided cooling in braze alloy manufacturing by HSMS method. Plasticizing of braze alloy wire is possible in this case by applying diffusion annealing, which leads to the redistribution of elements without visible grain growth.

The advantage of rapid quenching for this type of alloys consists in that the wire or band of preset dimensions is produced in one technological operation. A characteristic feature of rapid quenching is that the product surface features a low content of oxide films, and later on this positively influences the brazing processes, especially when the braze alloy is placed in the seam formation zone beforehand.

Products made by HSMS method and characterized by a special cross-sectional shape, can be regarded as semi-finished products for manufacturing calibrated wire of a round cross-section, as well as wire which has a longitudinal channel along its length for filling with flux or paste on its base. Wire deformation can be carried out by traditional methods of treatment of alloy forming, as for example by drawing or shaped rolling.

A package of investigations carried out by CJSC ALARM enabled development of basic advanced technologies (combining HSMS method, continuous and semi-continuous casting, and drawing together with fluxing, if required) and equipment for manufacturing of rods, bands, wire semi-finished products of non-round cross-section, round calibrated wire (with and without flux) of wide range. Wire of 0.3–3.0 mm diameter, rods with basic diameter of 1.6–6.0 mm and band of 0.4–1.0 mm thickness and 10–40 mm width are supplied.

Diversity of brands and wide range of braze alloy product typesizes allowed an essential widening of applications of hard-to-form brazes alloys in different branches of industry and for different brazing methods. Possibility of manufacturing extended products, also of small cross-sections, allows manufacturing em-

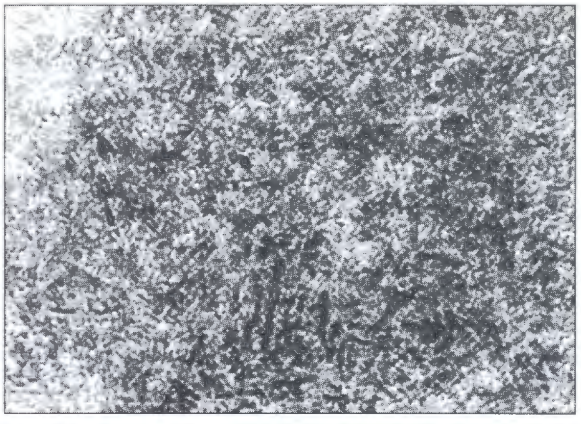

Figure 4. Microstructure of PMFOTsr 6-4-0.03 and P14 braze alloys after HSMS (×500)

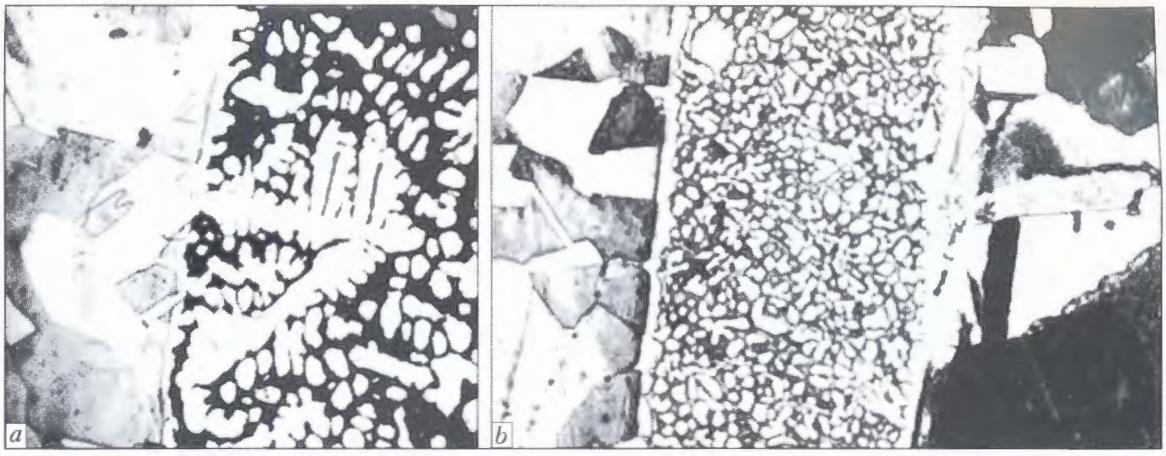

Figure 5. Microstructure of copper to copper brazed joint (×500) made by PMFOTsr 6-4-0.03 pressed rod (copper–seam) (*a*) and rapidly-quenched braze alloy P14 (copper–seam–copper) (*b*)

bedded elements for automatic and mechanized brazing processes that considerably reduces the unjustified application of deficit silver braze alloy.

Unique possibilities of HSMS method allowed correcting the composition of PMFOTsr 6-4-0.03 braze alloy of Cu–P–Sn system, alloyed for accommodating hot pressing and better structure modification by small zirconium additives [6].

As shown by investigations, the microstructure of PMFOTsr 6-4-0.3 and P14 braze alloys produced by HSMS method, does not differ. It is a quasi-eutectic and consists of an oversaturated solid solution of phosphorus in copper with dispersed particles of copper phosphide uniformly distributed in it (Figure 4). Such structure causes higher ductility of the made products and possibility of its further treatment for giving it the required shape, including the embedded elements. Wire and band of P14 and PMFOTsr 6-4-0.03 braze alloys can stand overbending through 180° for a few times and δ values are increased several times at stretching of wires made by HSMS method, in comparison with the values for extruded rods.

Value σ_t for P14 braze alloy (MF06-4) in the rapidly quenched state is equal to 670 MPa, and for PMFOTsr6-4-0.03 extruded braze alloy — 460 MPa; and δ value — to 7.0 and 1.7 % respectively.

High chemical and structural homogeneity, structure dispersity, low content of oxide films on the surface of braze alloys, manufactured by HSMS method, promote producing a homogeneous and fine-grained structure of the brazed joint with a smaller number of pores, cavities and other defects that is favorable for mechanical characteristics of joints.

A lower quality of cast and extruded rods leads to contamination of the brazed metal seam by slags and to porosity formation, and a coarser structure of extruded rods results in a coarser structure of the seam metal (Figure 5, *a*) in comparison with the structure produced using a braze alloy manufactured by HSMS method (Figure 5, *b*).

In such a way, as shown by metallographic analysis, the microstructure of the brazed seam, its dispersity are determined by density, surface cleanliness, dispersity of as-delivered braze alloy structure at equal brazing conditions, and do not depend on zirconium presence in its composition. Data that we received are in good agreement with the known investigations results on positive influence of amorphous and microcrystalline structure of the braze alloys of different systems on the structure and properties of the brazed joints [1, 7].

Rapidly quenched braze alloy are used in manufacturing of household refrigerators (copper and steel piping of cooling units), heat-exchange installations, tools, in instrument engineering (including joints of brass and combination of brass with steel (P81 braze alloy)), power machine-building, electrical engineering and so on, instead of PSr45, PSr40, PSr29.5, PSr15 and PSrF5-5 silver braze alloys.

1. Kalin, B.A., Fedotov, V.T., Sevryukov, O.N. et al. (1996) Amorphous strip braze alloys for brazing. Experience of development of technology for production and applications. *Svarochn. Proizvodstvo*, **1**, 15–19.
2. (1986) *Ultrarapid quenching of molten alloys*: Transact. Ed. by G. German. Moscow: Metallurgiya.
3. Vasiliev, V.A., Lozovan, A.A., Pashkov, I.N. et al. (2002) *Scientific prerequisites and practice of production of metastable materials*. Moscow: RGTU im. K.E. Tsiolkovsky.
4. Vasiliev, V.A., Mitin, B.S., Pashkov, I.N. et al. (1998) *Ultrarapid solidification of melt*. Moscow: Intermet Engineering.
5. Pashkov, I.N., Iliina, I.I., Shokin, S.V. et al. (1996) *Rapidly-quenched wire and strip of silver-free braze alloys: new aspects of production and application. Role of brazing processes in development of new technique*. Part 2. Moscow: TsRDZ.
6. Pashkov, I.N., Iliina, I.I., Shokin, S.V. et al. (2003) Influence of zirconium microalloying of copper–phosphorus–tin system and production technology on structure and properties of PMFOTsr 6-4-0.03 and P14 braze alloys, as well as joints brazed by them. In: *Proc. of Conf. on Brazing, Current Technologies, Materials, Structures, Service Experience of Brazed Structures*. Moscow: TsRDZ, 86–92.
7. Kalin, B.A., Plyushchev, A.N., Fedotov, V.T. et al. (2001) Influence of structural state of the braze alloy on physico-mechanical properties of brazed joints. *Svarochn. Proizvodstvo*, **8**, 38–41.

CHARACTERISTIC DEFECTS IN FSW OF SHEET ALUMINIUM ALLOYS AND MAIN CAUSES FOR THEIR FORMATION

A.G. POKLYATSKY
E.O. Paton Electric Welding Institute, NASU, Kiev, Ukraine

Characteristic defects formed in friction stir welds on aluminium alloy sheets (1.8–2.5 mm) are considered. The effect of the main welding process parameters and different technological factors on formation of these defects was studied. Main causes of lacks-of-fusion, formation of flash and overheating of metal on the weld metal face, as well as lacks-of-fusion in the root part of the welds and formation of defects in the form of discontinuities in their central part were established. Designs of the tools were developed, and ranges of variation of the main process parameters were determined, providing sound friction stir welded joints on aluminium alloy sheets.

Keywords: *friction stir welding, thin aluminium alloys, welded joint, weld defects, lacks-of-fusion, overheating, flash, discontinuities, defect prevention*

Friction stir welding (FSW) is widely applied in many countries of the world for manufacturing various structures from aluminium alloys [1–5]. At FSW permanent joints are produced in the solid phase without base metal melting, this allowing prevention of hot cracking in welds, reducing the degree of welded joint softening and lowering the level of residual stresses and deformations in the weldments, thereby improving their performance and residual life [6–9].

However, the conditions of formation and quality of welds depend essentially on the welding process parameters and various technological factors. The main parameters include (Figure 1): shoulder radius r_{sh} and design features of working surfaces of the shoulder and probe of the tool; angle of inclination Q of the tool to the vertical axis; force of pressing F of the working tool to the surfaces of parts being welded; depth of immersion t of tool shoulder into the metal being welded of thickness δ and of probe penetration l_{pr} into the butt; frequency of rotation ω of the tool about a vertical axis; welding speed v_w.

Stability of the process of weld formation and welded joint quality essentially depend also on the reliable fastening of the edges being welded, accuracy of their fitting and set up, weld length, joint geometry, etc. These technological factors can lead to excessive gaps in the butt, edge deplanation, shifting of butt axis relative to the tool, as well as change of some parameters of the welding process (force of tool pressing, depth of shoulder immersion or probe penetration). Incorrect selection of FSW parameters or their deviation in welding, as well as violation of the conditions of assembly and fastening of edges in welds, as a rule, lead to defects.

The purpose of this work is determination of the main causes for appearance of characteristic defects in welds at FSW of sheet aluminium alloys, as well as establishing effective methods of their prevention, which guarantee making sound welded joints.

Investigations were conducted in an experimental set up for FSW, which allows smooth adjustment of welding speed in the range of 4–40 m/h at the tool rotation frequency of 1420 or 288 rpm. Influence of process parameters and technological factors on defect formation in welds was evaluated in welding butt joints of sheet aluminium alloys AD31, AMtsN, AMg2M, AMg6M, 1420, 1201 and 1460. Weld defectiveness was determined by visual inspection, as well as using metallographic investigations, performed in MIM-8 optical microscope. It is established that at FSW of sheet (1.8–2.5 mm) aluminium alloys, it is possible to single out several types of characteristic defects, developing for different reasons.

Lack-of-fusion on the weld face. The main causes for development of such defects are the small diameter of the tool shoulder; large diameter of the tool probe; considerable depression on the working (end face) surface of the tool shoulder; insufficient immersion of the tool shoulder into the metal being welded; insufficient force of pressing of the tool to the surfaces of parts being welded during welding; low frequency of tool rotation, considerable welding speed; large gap in the butt and shifting of the butt axis relative to the tool; unreliable fixation of the edges being welded.

Weld formation at FSW occurs at excess pressure in a volume limited by working surfaces of the tool

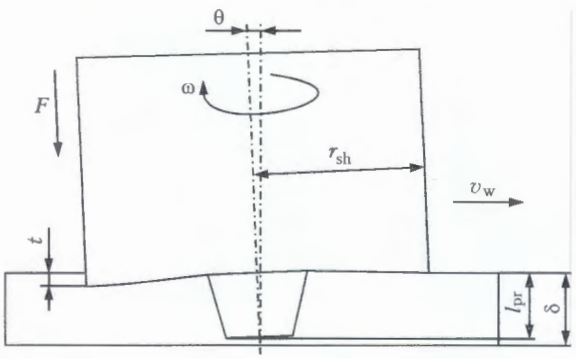

Figure 1. Schematic of FSW process and its main parameters

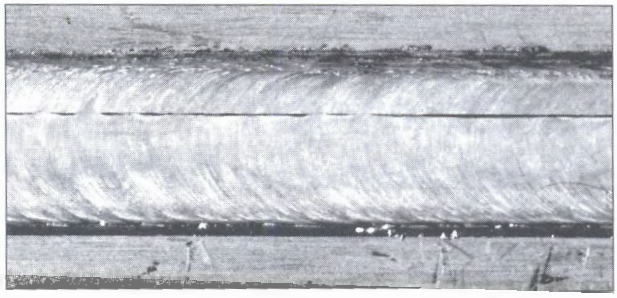

Figure 2. View of the weld face with a defect of lack-of-fusion type made by FSW on aluminium alloy AMg6M 2 mm thick (×2)

and the substrate. The metal is heated by friction forces up to the plastic state and is pressed out by the probe, which is rotating and moving along the tool butt into the freed volume behind it. In this connection, when a tool with a small diameter of the shoulder or a large diameter of the probe is used, the plasticized metal volume can be insufficient for a complete filling of the space freed behind the tool, which may result in a defect in the form of lack-of-fusion developing on the weld face (Figure 2).

To achieve welding process stabilization, a small circular depression is made on the end face of the tool shoulder, providing a smooth and continuous displacement of plasticized metal and formation of a sound weld face. The size of this groove should be such that at a slight immersion of the tool shoulder the moving plasticized metal was continuously at excess pressure. Insufficient immersion of the tool shoulder into the metal being welded or the force of tool pressing to the surface of parts being welded during welding, lead to increase of the volume filled by plasticized metal at weld formation, and, therefore, to lowering of excess pressure and formation of lack-of-fusion on the weld face.

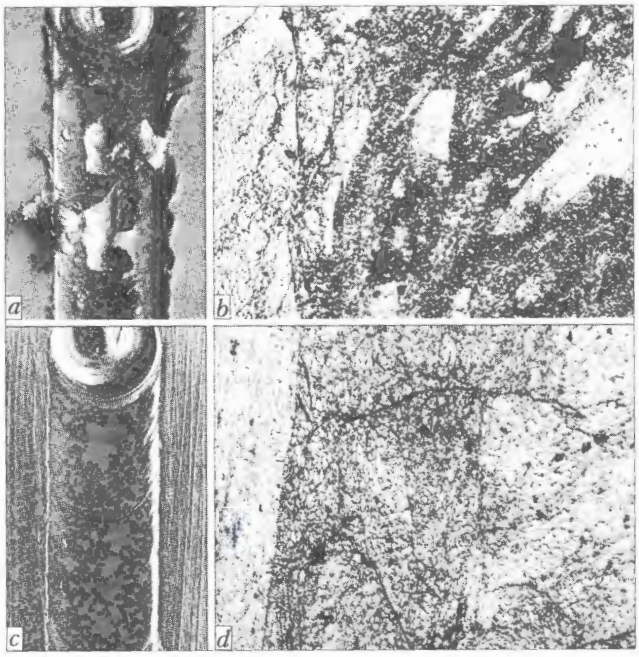

Figure 3. View (*a*, *c* — ×1.25) and microstructure (*b*, *d* — ×125) of the face of the weld made by FSW on 1420 alloy 2 mm thick with overheating (*a*, *b*) and without it (*c*, *d*)

Welding speed and tool rotation frequency essentially influence the heat evolution in the welding zone. At certain ratios of the frequency of tool rotation and speed of its displacement along the butt, the heat released at friction may turn out to be insufficient for plasticizing the volume of metal required for filling the void created by the tool probe. Degree of metal plasticizing can be increased due to lowering the welding speed or increasing the frequency of the tool rotation.

A gap in the butt also leads to lack-of-fusion, as the volume of plasticized metal is insufficient for filling the additional space between the edges being welded.

At shifting of the tool relative to the butt axis, weld formation occurs at the side. Located along the butt axis is a thermodeformational zone, in which the edges fuse to only a small depth or a defect in the form of lack-of-fusion develops.

Insufficient fastening of the edges being welded promotes formation of a gap between them, shifting of the butt axis, edge deplanation and violation of the conditions of immersion and pressing of the tool shoulder, which results in formation of such defects on the weld surface.

Metal overheating on the weld face. Main causes for formation of this defect are as follow: a large radius of the tool shoulder; excess force of tool pressing, great angle of tool inclination relative to the vertical axis; considerable frequency of the tool rotation; low welding speed; insufficient finish of the tool shoulder working surface; contamination of the surface of parts being welded.

The main quantity of heat required for metal plasticizing in the welding zone evolves at friction of the tool shoulder working surface against the surfaces of parts being welded and is found from the following expression [10]:

$$Q = 3/4\pi(r_{sh})^3 F\omega\mu/v_w,$$

where μ is the coefficient of friction.

Experimental studies showed that when a tool with a large shoulder diameter is used, excess of the evolved heat may lead to metal overheating in the welding zone and deterioration of the quality of weld face (Figure 3). Formation of such a defect is also possible in the case of too strong pressing of the tool to the surfaces of parts being welded or its immersion into the metal. Here, in addition to greater evolution of heat leading to metal overheating, tears occur on its surface.

Increase of the angle of tool inclination can be regarded as violation of the stability of the moving flow of plasticized metal. Excess immersion of the tool shoulder in the weld rear part leads to local overheating of the metal, periodically changes the path of its displacement, promoting formation of a non-uniform weld face with protrusions, depressions and tears.

Ratio of welding speed and frequency of tool rotation also essentially influence the degree of heating

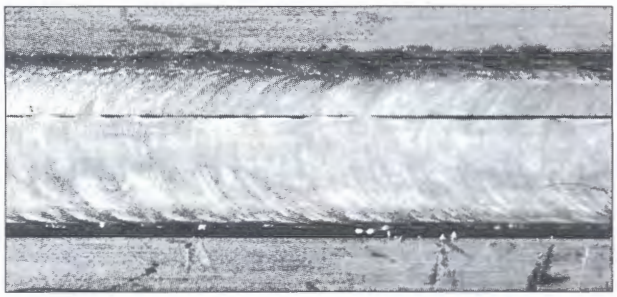

Figure 2. View of the weld face with a defect of lack-of-fusion type made by FSW on aluminium alloy AMg6M 2 mm thick (×2)

and the substrate. The metal is heated by friction forces up to the plastic state and is pressed out by the probe, which is rotating and moving along the tool butt into the freed volume behind it. In this connection, when a tool with a small diameter of the shoulder or a large diameter of the probe is used, the plasticized metal volume can be insufficient for a complete filling of the space freed behind the tool, which may result in a defect in the form of lack-of-fusion developing on the weld face (Figure 2).

To achieve welding process stabilization, a small circular depression is made on the end face of the tool shoulder, providing a smooth and continuous displacement of plasticized metal and formation of a sound weld face. The size of this groove should be such that at a slight immersion of the tool shoulder the moving plasticized metal was continuously at excess pressure. Insufficient immersion of the tool shoulder into the metal being welded or the force of tool pressing to the surface of parts being welded during welding, lead to increase of the volume filled by plasticized metal at weld formation, and, therefore, to lowering of excess pressure and formation of lack-of-fusion on the weld face.

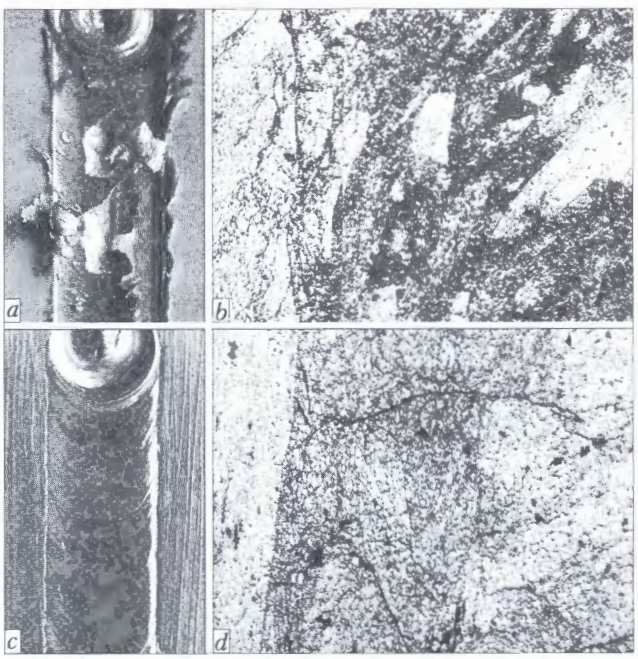

Figure 3. View (*a*, *c* — ×1.25) and microstructure (*b*, *d* — ×125) of the face of the weld made by FSW on 1420 alloy 2 mm thick with overheating (*a*, *b*) and without it (*c*, *d*)

Welding speed and tool rotation frequency essentially influence the heat evolution in the welding zone. At certain ratios of the frequency of tool rotation and speed of its displacement along the butt, the heat released at friction may turn out to be insufficient for plasticizing the volume of metal required for filling the void created by the tool probe. Degree of metal plasticizing can be increased due to lowering the welding speed or increasing the frequency of the tool rotation.

A gap in the butt also leads to lack-of-fusion, as the volume of plasticized metal is insufficient for filling the additional space between the edges being welded.

At shifting of the tool relative to the butt axis, weld formation occurs at the side. Located along the butt axis is a thermodeformational zone, in which the edges fuse to only a small depth or a defect in the form of lack-of-fusion develops.

Insufficient fastening of the edges being welded promotes formation of a gap between them, shifting of the butt axis, edge deplanation and violation of the conditions of immersion and pressing of the tool shoulder, which results in formation of such defects on the weld surface.

Metal overheating on the weld face. Main causes for formation of this defect are as follow: a large radius of the tool shoulder; excess force of tool pressing; great angle of tool inclination relative to the vertical axis; considerable frequency of the tool rotation; low welding speed; insufficient finish of the tool shoulder working surface; contamination of the surface of parts being welded.

The main quantity of heat required for metal plasticizing in the welding zone evolves at friction of the tool shoulder working surface against the surfaces of parts being welded and is found from the following expression [10]:

$$Q = 3/4\pi(r_{sh})^3 F\omega\mu/v_w,$$

where μ is the coefficient of friction.

Experimental studies showed that when a tool with a large shoulder diameter is used, excess of the evolved heat may lead to metal overheating in the welding zone and deterioration of the quality of weld face (Figure 3). Formation of such a defect is also possible in the case of too strong pressing of the tool to the surfaces of parts being welded or its immersion into the metal. Here, in addition to greater evolution of heat leading to metal overheating, tears occur on its surface.

Increase of the angle of tool inclination can be regarded as violation of the stability of the moving flow of plasticized metal. Excess immersion of the tool shoulder in the weld rear part leads to local overheating of the metal, periodically changes the path of its displacement, promoting formation of a non-uniform weld face with protrusions, depressions and tears.

Ratio of welding speed and frequency of tool rotation also essentially influence the degree of heating

and level of metal plasticizing. Therefore, lowering of welding speed or increase of the frequency of tool rotation may lead to metal overheating and impair the quality of weld surface.

To ensure a uniform finely-rippled surface of the weld face the tool shoulder working surface is usually ground or polished. Its high surface finish promotes a smooth and uniform displacement of plasticized metal. Any burrs, protrusions or dents on it will cause periodical changes of the metal displacement path, speed of its motion, as well as volume. In this case, the dynamic thermal equilibrium and continuity of metal flow are disturbed, and the weld face develops defects in the form of local sections of overheated metal and isolated tears. Various contaminations in the form of hard particles on the surface of parts being weld lead to the same consequences. Penetrating under the working surface of the tool shoulder, they move together with plasticized metal and cause local overheating in it without disturbing the continuity of its flow. This results in non-uniform formation of the weld face with local tears, dents and burrs.

Flash on the weld face. Such a defect develops at FSW as a result of the following causes: excess immersion of the tool shoulder into the metal being welded; large angle of inclination of the tool relative to the vertical axis; excess height (deplanation) of the edge from the side of tool retreating; tool deviation from the vertical axis to the left or to the right relative to the butt; unreliable fastening of the edges being welded.

To ensure a sound weld formation at FSW, the shoulder working surface is immersed into the metal being welded to a small depth. Its excess immersion leads to ousting of part of plasticized metal on the weld face from the side of the tool retreating (where the vectors of the direction of tool rotation and welding speed are oriented in opposite directions) in the form of flash (Figure 4). A similar defect can develop in welds at a large angle of the tool inclination relative to the vertical axis, when the metal is pressed out by the tool shoulder in the weld rear part. As a rule, ductile materials are prone to flash formation (AD31, AMtsN, AMg2M), whereas in welding of high-strength aluminium alloys (1420, 1201 and 1460) metal overheating, tear formation and metal ousting on the weld face can proceed simultaneously.

Edge deplanation also promotes flash formation on the weld face. However, in case of excess edge height from the side of tool advance (where the vectors of the direction of the tool rotation and welding speed coincide) the excess metal is cut off by the shoulder, and the flash remains only in the case of excess height of the edge from the tool retreating side.

At FSW the tool should be located so that no deviation of the tool from the vertical axis to the left or right relative to the butt occurred during weld formation, otherwise at its inclination to the edge from the side of the tool advance the plasticized metal will be partially ousted from under the shoulder and form the flash.

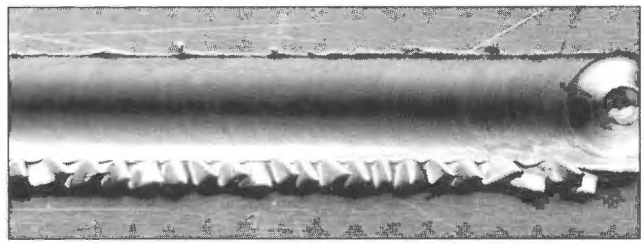

Figure 4. View of weld face with a defect of flash type made by FSW on aluminium alloy AMtsN 2 mm thick (×1.25)

Sheet aluminium alloys are highly prone to warping as a result of heating in welding. Therefore, in the case of unreliable fastening or fixing of the edges far from the welding zone, their shifting may take place in a certain section of the butt in the vertical plane. In such a case the metal ousted by the tool shoulder develops a defect in the form of flash.

Lack-of-fusion in the weld root. The causes for formation of such defects in the welds are insufficient length of the probe for this thickness of metal being welded; tool shoulder immersion into the metal being welded and force of the tool pressing to the surfaces of parts being welded; large shifting of the butt axis relative to the tool; tool probe wear during welding.

To ensure reliable mixing of the metal along the entire thickness of edges being welded and sound weld formation, the tool probe should have a certain length for each thickness of metal being welded. If the tool probe penetrates practically through the entire thickness of the edges, the heat evolved at FSW and applied force impact is sufficient for the interfaces of the parts being welded to become close in size to intergranular boundaries. Otherwise, the weld root part will develop a defect of the type of lack-of-fusion (Figure 5).

However, even at a correct selection of the length of the tool probe at FSW it is necessary to ensure the required immersion of the tool shoulder into the metal being welded and constant force of the tool pressing to the surfaces of parts being welded, as in welding of sheet materials even a slight displacement of the tool in the vertical plane may lead to a lack-of-fusion in the weld root part. Development of such defects is also possible at a great shifting of the butt relative to the tool. This is due to a very small (about 3 mm) diameter of the cone-shaped probes applied in FSW of sheet materials.

During operation the tool probe can become worn (most often as a result of touching the substrate), so that the tools should be made of strong and wear-resistant materials. The fixture should ensure a high accuracy of the butt assembly and movement of the tool along it, as well as reliable fixing of the edges and stable pressing of the tool to the surfaces of parts being welded.

Inner defects in the form of discontinuities. As shown by experimental results, these defects can develop in welds in the case of overheating of the metal

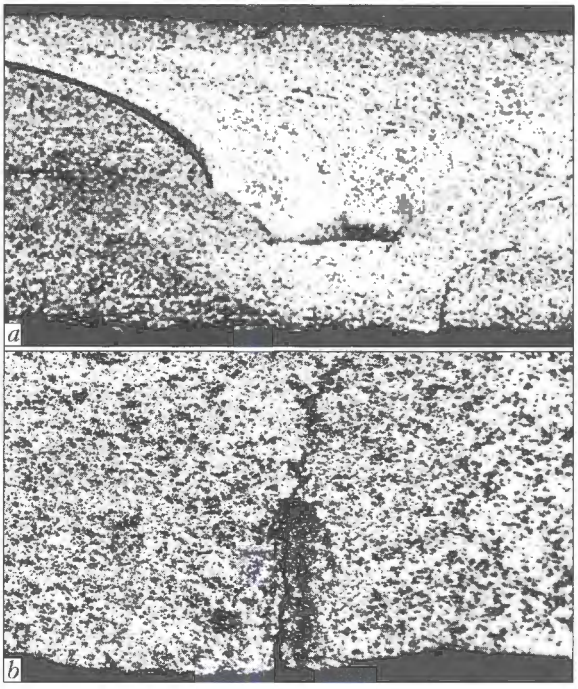

Figure 5. Transverse macrosection of the welded joint with a lack-of-fusion in the weld root part (*a* — ×25) made by FSW on AMg2M alloy 2 mm thick, and microstructure (×300) of weld section (*b*) in the place of defect location

being welded or at insufficient heat evolution for plasticizing in the welding zone of the metal volume required for weld formation (Figure 6).

Excess overheating of metal in the welding zone leading to surface melting of intergranular boundaries with low-melting eutectics accumulating there, occurs, mainly, for the same causes as owing to overheating of the weld face metal and flash formation. Just the degree of metal overheating is higher here.

In case of insufficient heat evolution in the welding zone the required ductility of the metal volume necessary for weld formation, which is continuously moving along a complex path in a limited space, is not ensured. This results in violation of the continuity of the plasticized metal flow, and the weld develops inner cavities unfilled with metal. The causes for their appearance are practically the same. They lead to lack-of-fusion of the metal on the weld face, but since the volume of plasticized metal is somewhat greater, the defect does not come to the surface, but stays inside the weld.

Thus, as a result of performance of a package of scientific-experimental investigations, as well as on the basis of the data of foreign publications, the ranges of variation of the main parameters of the process were established, which allow producing sound joints of sheet aluminium alloys by FSW. A design of the tool with probes in the form of a truncated cone was developed. The diameter of the probe base should be equal to 3.2–3.6 mm, and that of the probe tip — 2.4–2.6 mm. To avoid lacks-of-fusion in the weld root part, the probe length should be equal to (0.90–0.95)δ, optimum diameter of the tool shoulder — to 10–12 mm. To ensure a stable weld formation it is necessary to make a conical or semi-spherical groove on the shoulder working surface. It is recommended to make tools for FSW of sheet aluminium alloys from tool steels of R6M5 type. Welding is performed by backward inclined tool at the angle of tool inclination of 2–3° relative to the vertical axis. The force of tool pressing to the surface of parts being welded is equal to 5–10 kN and depends on the grade of the alloy being welded.

Shifting of the butt axis relative to the tool in welding of sheet aluminium alloys should not be more than 0.5 mm. The admissible gap between the edges is not more than 0.3 mm. Excess height of the edge from the tool advancing side should not me more than 25 %, and from the tool retreating side — 5 % of the thickness of metal being welded. In this connection, during welding it is necessary to ensure a reliable fastening of the parts being welded as close as possible to the butt, and to place in front of the tool the press-down roller, preventing edges warping in welding.

Sound joints, while satisfying all the above conditions, can only be produced in certain ranges of variation of the frequency of rotation and speed of movement of the tool, which may be quite broad for ductile low-alloyed alloys or narrower for high-strength complex alloys. As a rule for the studied material thicknesses the frequency of the tool rotation is equal to 1000–3000 rpm, and the welding speed is 4–40 m/h. Depending on the grade of the alloy being welded and requirements made of the welded joint, it is necessary to experimentally determine the optimum frequency of rotation and speed of displacement of the tool along the butt.

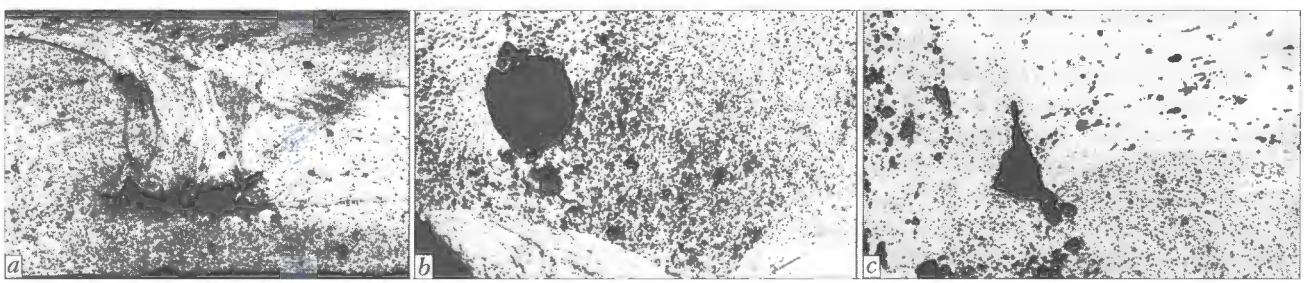

Figure 6. Macrosection of a welded joint with inner defects in the weld (*a* — ×25), and microstructure of weld metal in the zone of the defect caused by metal overheating (*b* — ×500) or insufficient volume of plasticized metal (*c* — ×300) made by FSW on AMg6M alloy 2 mm thick

1. Norlin, A. (2000) A century of aluminium — a product of the future. *Svetsaren*, **2**, 31–33.
2. Weman, K. (2000) Equipment for aluminium welding. *Ibid.*, 11–13.
3. Kallee, S.W., Devenport, J., Nicholas, E.D. (2002) Railway manufacturers implement friction stir welding. *Welding J.*, **10**, 47–50.
4. Arbegast, W. (2002) Friction stir welding after a decade of development. *Ibid.*, 28–35.
5. Ding, J., Carter, R., Lawless, K. et al. (2006) Friction stir welding flies high at NASA. *Ibid.*, **3**, 54–59.
6. Defalco, J. (2006) Friction stir welding vs fusion welding. *Ibid.*, 42–44.
7. Okamura, H., Aota, K., Ezumi, M. (2000) Friction stir welding of aluminum alloy and application to structure. *J. Jap. Institute of Light Metals*, **4**, 166–172.
8. Lanciotti, A., Vitali, F. (2003) Characterisation of friction stir welded joints in aluminium alloy 6082-T6 plates. *Welding Int.*, **8**, 624–630.
9. Ericsson, M., Sandstrom, R. (2003) Influence of welding speed on the fatigue of friction stir welds and comparison with MIG and TIG. *Int. J. Fatigue*, **25**, 1379–1387.
10. Okamura, H. (2003) Point of application for FSW. *Welding Techn.*, **15**, 60–69.

UPGRADED EQUIPMENT FOR AUST OF END SECTIONS OF PIPES

V.L. NAJDA[1], A.A. MOZZHUKHIN[1], O.F. LOBANOV[1], V.A. IGNATENKO[1], Yu.A. OLEJNIK[1], I.V. EFIMOV[1], A.P. KOPYLOV[2] and A.F. ZAKHAROV[2]
[1]SE «E.O. Paton EWI DO», NASU, Kiev Ukraine
[2]Vyksunsky Metallurgical Plant, Russia

Directions of improvement of the ultrasonic testing automation technology of end sections of pipes of big diameter on acting line production are described. Upgrading is fulfilled with application of a new flaw detector of the NK 363 type, developed in the E.O. Paton EWI Design Office on basis of industrial computer of the ASR 4000 series and five UPSC 3108 MBA eight-channel ultrasonic multiplexers («Socomate», France).

Keywords: *ultrasonic testing, pipes, line production, flaw detector, installation*

In 2004 two sets of the NK 362 installations (Figure 1) for automated ultrasonic testing (AUST) of end sections of welded pipes of 508–1420 mm diameter with thickness of walls 7–50 mm were developed and manufactured at the PWI DO and supplied to OJSC «Vyksunsky metallurgical plant». In 2007 to «Vyksunsky metallurgical plant» the upgraded NK 362M version of this installation was supplied.

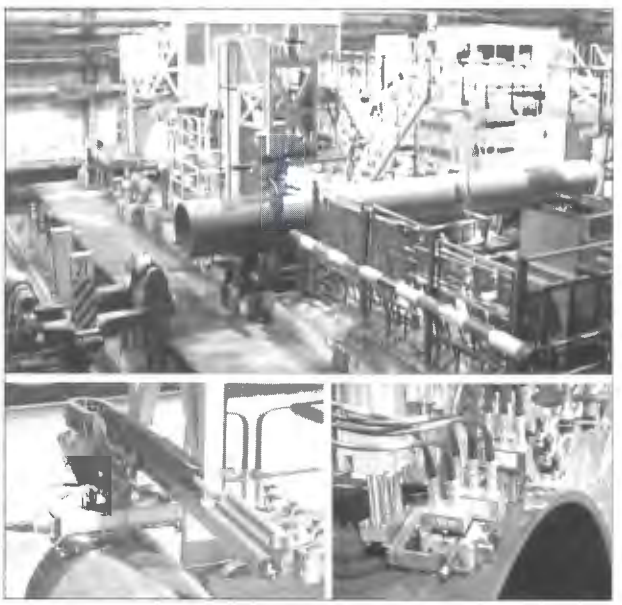

Figure 1. NK 362M installation at «Vyksunsky Metallurgical Plant»

The NK 362M installation has the following differences in comparison with the NK 362 installation:

- mounting rigidity of the acoustic transducer units is increased;
- coustic units *A* and *B* (Figure 2) have independent pneumatic actuators;

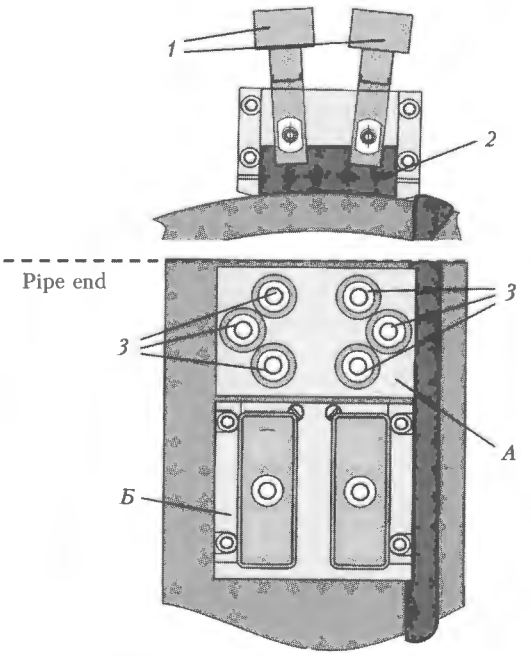

Figure 2. Scheme of check and spatial arrangement of US transduces: *1* — film broad-coverage piezoelectron transduces (PET) of «Krautkramer» company with 60 mm check zone; *2* — immersion bath; *3* — inclined PET with angle of introduction 45° and 30 mm check zone; *A*, *B* — acoustic units for checking presence of respectively longitudinal defects and laminations

Figure 3. Cabin of NK 362M installation operator

• increase of the controlled end section width up to 300 mm is possible;

• acoustic scheme of check and algorithm of its performance, at which acoustic units are always in zenith of the pipe and transducers for checking presence of longitudinal defects and laminations are placed in separate units, are changed; slot method of establishing acoustic contact is replaced for the immersion one;

• multi-channel ultrasonic flaw detector of NIINK production (Kishinev, Moldova) is replaced for the flaw detector of own design with application of multichannel US boards («Socomate» company, France).

Scheme of check and spatial arrangement of US transducers are shown in Figure 2. In US testing for presence of laminations operates only acoustic unit *B*. When performing check for presence of laminations and longitudinal cracks the testing is performed sequentially: check for presence of laminations during first turn of the pipe; movement of the acoustic units along the weld; check for presence of longitudinal defects during second turn of the pipe (acoustic units are always in zenith of the pipe). In case of detection of the defects acoustic units *A* and *B* move to an adjacent ring and the check cycle repeats.

Cabin of the NK 362M installation operator is shown in Figure 3.

Main advantages of the new flaw detector consist in universality of the US boards, which allows easy readjustment for a new scheme of testing; high speed of collection and processing of the check data; increased level of noise protection; high reliability and stability of operation; flexible software that meets state-of-the-art requirements.

Used in the flaw detector universal US boards of the «Socomate» company represent full-size PCI-boards for installation on chassis of an industrial computer and are designed for development of US flaw detectors of different complexity and implementation of different schemes of testing. The board itself carries out amplification, filtration and digitations of a signal, its digital processing and preliminary storage in memory of the board itself for its further transmission by packages into the computer storage device with application of the DMA mode.

There are following types of the UPSC series boards: single-channel ones with a generator aboard and a remote generator; multi-channel ones (8 multiplexed channels) with common and independent parameters. Due to their functional possibilities they allow performing high-speed collection of data in A- and C-scan mode and non-speedy selection in C-scan mode.

NEWS

NEW GENERATION COMPLEX FOR ARC WELDING OF POSITION BUTTS OF PIPES OF THE MAIN PIPELINES

The purpose of «STYK» complex developed at the E.O. Paton Electric Welding Institute of NASU is performance of automatic orbital upward arc welding of position butts of the main pipelines using flux-cored wire with forced weld formation by two welding heads.

The root weld is made on the outside of the pipe joint with application of a self-propelled inner aligning device with special copper backing ring in the automatic mode. Subsequent passes are made to fill the groove and perform weld facing. After each pass the groove is filled for 5–8 mm (depending on pipe wall thickness). Specialized flux-cored wires of 1.6, 2.0 and 2.4 mm diameter were developed to make welded joints of steels of X70 and X80 class.

«STYK» complex equipment is made by OJSC «Kakhovka Plant of Electric Welding Equipment». Special flux-cored wires are made by SE «Pilot Plant of Welding Consumables of the E.O. Paton Electric Welding Institute of the NAS of Ukraine». Scientific-technical support was provided by the E.O. Paton Electric Welding Institute of NASU.

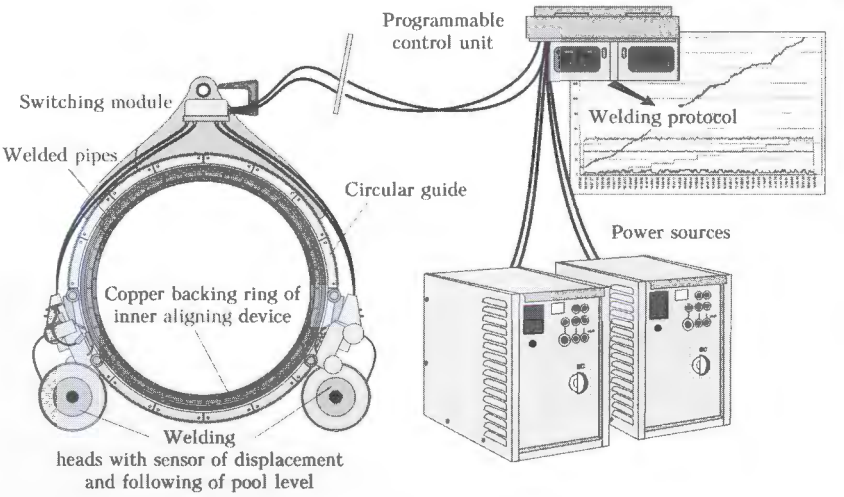

DC ELECTROSLAG CRUBILE FURNACE

The crucible furnace developed by STC «E.O. Paton Electric Welding Institute» is a compact unit supplied as part of the technology complex designed for establishing a metallurgical mini-plant.

The complex is applied for remelting the wastes of ferrous and non-ferrous metal and alloy production, for processing the ferroalloy enterprise piles, in processing of various non-metallic wastes, and in production of calcium carbide and fluxes.

In addition to the furnace the complex includes:

• ingenious modular power source, which consists of several independent rectifiers;

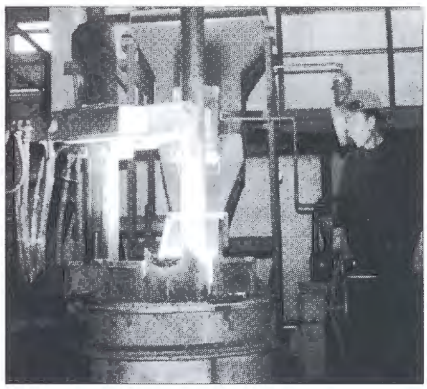

• control module, consisting of the control panel and cabinet;

• gas-cleaning unit (provides a not less than 97.5 % degree of cleaning of the waste gases; content of carbon oxides, nitrogen and sulphur in them after cleaning is below the MAC).

The main technical characteristics of the complex are as follows: mains voltage of 380 V; primary power of 630 kW; working voltage of 0–56 V; working current (max) of 9000 A; furnace crucible volume (working) of 200 dm^3; working mode is continuous.

CONTINUOUS CUTTING DEVICE «DONMET-807»

Kramatorsk Plant of Autogenuous Equipment «Donmet» offers to its users not only its serial products, but also ingenuous devices for flame cutting of the rolled stock.

One of such devices is «Donmet-807». In the summer of 2007 it was introduced into production in the mechanical section of the rolling shop of OJSC «Donetsk Metal-Rolling Plant». This device allowed automation of severing of rolled stock of 125 × 125 mm section, earlier performed by manual cutters.

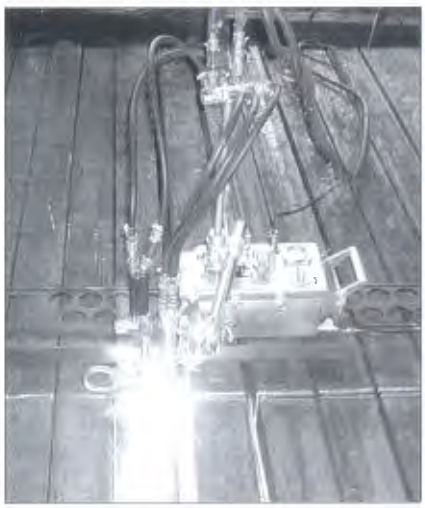

The continuous cutting device is a self-propelled portable machine CG-100 carrying the rod with a carriage, in which a gas cutter and «Donmet-290» torch are fixed.

Energy carriers (combustible gas and oxygen) are fed to the cutter and torch through special hoses from the gas collector mounted on the self-propelled machine.

The self-propelled machine moves along the guide rail. Two furrows are made on the rail surface at 150 mm distance from each other for the wheels. A mechanical friction variator ensures a smooth stepless adjustment of the machine movement speed and, therefore, of gas cutting. Used as the displacement drive is a low-power electric motor (220 V), which is connected to the wheels through a two-stage gear. Idle run coupling allows switching off the drive and freely moving the machine along the guide rail. Cut thickness is adjusted by replacement of the gas cutter nozzle. This determines the set speed of machine displacement. Depending on the rolled stock thickness, the gas cutting speed of the device can be between 80 and 800 m/min.

As shown by practical application of «Donmet-807» device in the mechanical section of the rolling shop of OJSC «Donetsk Metal-Rolling Plant» the time of cutting rolled stock of 125 × 125 mm cross-section was reduced by 40 % compared to manual cutting. In addition, at machining the cut width was reduced more than 1.5 times (from 8 to 5 mm), and, hence, also the metal losses during blank preparation. Combustible gas (methane) and oxygen flow rate was also reduced by 10 %.

EXHIBITION «WELDING. ALLIED TECHNOLOGIES — 2008» IN KIEV

On April 7–9, 2008, PATON EXPO Exhibition was held at «KievExpoPlaza» Exhibition Center, uniting such expositions as «Welding. Allied Technologies», «Pipeline Transportation», «Non-Destructive Testing», «Corrosion Protection», «Industrial Ecology», «Fasteners and Tools», «Measurements. Laboratory Equipment». They were organized by Technology Transfer Center of the E.O. Paton Electric Welding Institute of the NAS of Ukraine with the support of the Society of Welders of Ukraine, NAC «Neftegaz Ukrainy», OKO Association, Association of Industrial Armature Engineering of Ukraine, Association of Manufacturers and Builders of Polymer Pipelines of Ukraine.

Altogether 48 participants, coming from Ukraine, Russia, Lithuania, Italy, Czekia, demonstrated their achievements in the Exhibition. Among them were the E.O. Paton Electric Welding Institute of the NAS of Ukraine, PWI Experimental Design-Technological Bureau, two PWI pilot plants (of Welding Equipment and of Welding Consumables), STC SEPROZ, Interindustry Education-Certification Center, known manufacturers of equipment for welding, cutting and brazing — KZESO (Kakhovka), SELMA Company (Simferopol), «Fronius-Ukraine» (Kiev District), «Kommunar» (Kharkov), SiMZ (Simferopol), DONMET (Novokramatorsk), GRPZ (Ryazan), «Zont» (Odessa), manufacturers of welding consumables: PWI Pilot Plant of Welding Consumables (Kiev), Losinoostrovsky Electrode Manufacturing Plant (Moscow), «Torgovy Dom Mezhgosmetiz» (Mtsensk), «Plazmatek» (Vinnitsa), «Anyksin Varis» (Anikshchyaj).

A significant part of the expositions was taken up by the representative offices of the known world welding manufacturers (ESAB, Lincoln Electric, Kemppi, Boehler, Abicor Binzel, Weldoterm, etc.) — ESAB Ltd. in Ukraine, «Binzel Ukraine», «Weldoterm-Ukraine», «Interkhim-BTV», «Vistek», etc.

An even greater number of booths were taken up by trading organizations such as «Abplanalp Ukraina», «Avdeks», «AVTsentr», «Dary Prirody», «Develd», «Idel», «Industrialy Metizny Soyuz», «Lincoln Electric Europe», «Migatex», «Ruso», «Svarkom», etc.

It is gratifying that for the first time in the specialized exhibitions of Ukraine four companies simultaneously namely «Artyom», «NAVKO-TEKh», «Fronius-Ukraine» and «ABB-Ukraine» (all located in Kiev and Kiev District), demonstrated the robotic welding systems, including robots of such well-known companies as «Fanuk», «Kawasaki», «Panasonic». This is, certainly, due to the growing interest of Ukrainian industry to the issues of production automation.

Achievements of Italian enterprises were presented in «Mipa Italy» booth (manufacturing equipment for arc welding and thermal cutting, stainless and aluminium welding wires and rods, as well as flux-cored wires).

Czekia was presented by MGM Company — a producer of plasma and gas-oxygen machines for ther-

Opening of the Exhibition

Fragments of the Exhibition activities

mal cutting. It is characteristic that all of them are fitted with systems of waste gas removal. The same company demonstrated their new development — an ultrasonic system for solar element welding.

During the Exhibition a Conference of the Society of Welders of Ukraine on the topic of «Paths of development of welding fabrication of Ukraine in connection with joining the World Trade Organization» was held, and meetings of a number of sessions of the Conference on NDT were conducted.

Within the PATON EXPO framework the exposition of firms and companies working in the field of non-destructive testing and technical diagnostics looked impressive. Among them are «Izotop», «Science-Production Diagnostic Center», OKO Association, «Ultrakon», representative office of «National Instruments» US Company (Kiev), «Intron» (Odessa), «Mashinostroenie» (Dnepropetrovsk), «Olympus Moscow» (Moscow), as well as trading organizations, such as «Kievprominvest», «Oniko», «Pergam», «Tvema» (Kiev), «Sperantsa» (Zheltye Vody).

On the whole, the Exhibition demonstrated the state-of-the-art of welding fabrication and the tenden-

Ya.I.Mikitin, Director of KZESO company, familiarizes the Exhibition visitors with the equipment made at the plant

cies in development and production of a broad range of equipment and materials for various purposes. In one of the next issues of «The Paton Welding Journal» it is planned to publish an analytical review of the state of development and manufacturing of arc welding power sources presented in the expositions of this Exhibition.

In conclusion it should be noted that the annual exhibition «Welding. Allied Technologies» already traditionally is the main profile exhibition in Ukraine. During the three days of its functioning, it was actively visited by numerous specialists of the subdivisions, departments, institutes and commercial companies from many regions of Ukraine.

V.N. Lipodaev, Dr. of Sci. (Eng.), PWI
A.T. Zelnichenko, Cand. of PhMat. Sci., PWI

SUBSCRIPTION
FOR «THE PATON WELDING JOURNAL»

If You are interested in making subscription directly via Editorial Board, fill, please, the coupon and send application by fax or e-mail.

The cost of annual subscription via Editorial Board is $324.

Telephones and faxes of Editorial Board of «The Paton Welding Journal»:

Tel.: (38044) 287 6302, 271 2403, 529 2623

Fax: (38044) 528 3484, 528 0486, 529 2623.

«The Paton Welding Journal» can be also subscribed worldwide from catalogues of subscription agency EBSCO.

SUBSCRIPTION COUPON
Address for journal delivery

Term of subscription since _____ **200** **till** _____ **200**
Name, initials _____
Affiliation _____
Position _____
Tel., Fax, E-mail _____

ADVERTISEMENT IN «THE PATON WELDING JOURNAL»
(DISTRIBUTED ALL OVER THE WORLD)

«AVTOMATICHESKAYA SVARKA»
RUSSIAN VERSION OF «THE PATON WELDING JOURNAL»
(DISTRIBUTED IN UKRAINE, RUSSIA AND OTHER CIS COUNTRIES)

External cover, fully-colored:
First page of cover (190×190 mm) – $570
Second page of cover (200×290 mm) – $400
Third page of cover (200×290 mm) – $400
Fourth page of cover (200×290 mm) – $400

Internal cover, fully-colored:
First page of cover (200×290 mm) – $400
Second page of cover (200×290 mm) – $400
Third page of cover (200×290 mm) – $400
Fourth page of cover (200×290 mm) – $400

Internal insert:
Fully-colored (200×290 mm) – $340
Fully-colored (double page A3) (400×290 mm) – $570
Fully-colored (200×145 mm) – $170

- Article in the form of advertising is 50 % of the cost of advertising area
- When the sum of advertising contracts exceeds $1000, a flexible system of discounts is envisaged

Technical requirement for the advertising materials:
- Size of journal after cutting is 200×290 mm
- In advertising layouts, the texts, logotypes and other elements should be located 5 mm from the module edge to prevent the loss of a part of information

All files in format IBM PC:
- Corell Draw, version up to 10.0
- Adobe Photoshop, version up to 7.0
- Quark, version up to 5.0
- Representations in format TIFF, color model CMYK, resolution 300 dpi
- Files should be added with a printed copy (makeups in WORD for are not accepted)